Optimal Low Thrust Transfers Between Planetary Parking Orbits

A Report submitted

in partial fulfilment for the Degree of

Bachelor of Technology

in

Aerospace Engineering

by

Padmanabha Prasanna Simha

(SC14B034)

pursued in

Department of Aerospace Engineering

Indian Institute of Space Science and Technology

to

INDIAN INSTITUTE OF SPACE SCIENCE AND TECHNOLOGY

THIRUVANANTHAPURAM

April 2018

CERTIFICATE

This is to certify that the project report titled, "Optimal Low Thrust Transfers Between Planetary Parking Orbits" submitted by Padmanabha Prasanna Simha, to the Indian Institute of Space Science and Technology, Thiruvananthapuram, in completion of the final year project from January 2018 to April 2018, is a bonafide record of the work carried out by him under our supervision. The contents of this report, in full or part, has not been submitted to any other institute or university for the award fo any degree or diploma.

Dr. Ramanan R. V	**Dr. Manoj T. Nair**
Adjunct Professor	Head of the department
Department of Aerospace Engineering	Department of Aerospace Engineering

Place: IIST, Thiruvanathapuram
April 2018

Declaration

I declare that this report titled, "Optimal Low Thrust Transfers Between Planetary Parking Orbits" submitted in completion of the final year project work from January 2018 to April 2018 is a record of the original project work carried out by me under the supervision of Dr. Ramanan R. V. In keeping with the ethical practice in reporting scientific information, due acknowledgments have been made wherever the findings of others have been cited. I aver that if any part of the report is found to be plagiarized, I shall take full responsibility of it.

Place: IIST, Thiruvanathapuram
April 2018

Padmanabha Prasanna Simha
SC14B034

Acknowledgements

I would like to sincerely express my gratitude to my guide Dr. Ramanan R. V for the support, guidance and discussions during the course of the project. I also wish to thank my parents for their constant encouragement.

I take this opportunity to thank the developers and contributors of the Boost library and the C++ Standards Committee for building the C++ programming language and it's libraries to the extent it is today. I would also like to thank Bill Gray, the developer of the ephemeris code, "Project Pluto" which my current work hugely benefited from. The Jet Propulsion Laboratory of NASA has my appreciation for publishing exhaustive ephemeris data in the public domain.

Abstract

Low thrust transfers require the solution to continuous optimal control problems. Here, the indirect approach to optimal control is applied. The dynamics of the spacecraft under gravity is represented as a set of differential equations in the three dimensional Cartesian frame of reference. Costates are introduced and Pontryagin's minimum principle is used to derive the optimal control law and the costate dynamics. This results in the formulation of a two point boundary value problem where the initial values of the costates are unknown. The final boundary condition is the desired orbit that the spacecraft has to attain. This problem is solved using differential evolution, a search based global optimization method. The cost function is set as the error in attaining the final orbit while the search is performed in a hyper-box of initial costate variables. A parallelized code has been written in standard C++17. The efficiency of the parallelization has been tested. The differential evolution algorithm has been benchmarked against a wide variety of test problems.

Several problems have been solved in the heliocentric and geocentric frames. The problem of transfer between two generic heliocentric orbits has been extensively studied and several parametric studies have been performed. The problem of transferring from the geosynchronous transfer orbit to geostationary orbits with inclination change has also been solved.

Nuclear and solar electric power models and their impact on spacecraft trajectories have been investigated. It has been observed that nuclear electric propulsion offers significant advantages when compared to solar electric propulsion for outward travel in the solar system. This situation reverses during transfers to the inner planets.

The spacecraft state dynamics, costate dynamics and the optimal control law have also been derived under the influence of multiple gravitating bodies. Coordinate frame switching based on the crossing of planetary mean spheres of influence has also been implemented. This is to reduce numerical sensitivity and roundoff errors during the integration of the spacecraft's orbit with double precision floating point arithmetic. Both time and fuel optimal Earth-Mars transfers have been generated and analyzed.

Further possibilities of applying this computational strategy for optimal control including high thrust propulsive lunar landing problems have been explored.

Table of contents

List of figures **xv**

List of tables **xvii**

Nomenclature **xix**

1 Introduction **1**

1.1 Low thrust propulsion systems 1

1.2 Implications of low thrust levels on orbital maneuvers 2

1.3 Problem description 2

2 Literature Survey **5**

2.1 Low thrust spacecraft 5

2.2 Trajectory design and optimization with low thrust spacecraft 6

2.3 Recent developments 8

3 Problem Formulation **11**

3.1 Spacecraft dynamics with a single central body 11

3.2 Spacecraft dynamics with two gravitating bodies 12

3.3 Formulation of the optimal control problem 13

3.3.1 Cost functions 13

3.3.2 Transformation of Cartesian state vector to semi-major axis, angular momentum and eccentricity vectors 14

3.3.3 Transforming Keplerian orbital elements to state vector 14

3.4 Constraints on the controls 15

3.4.1 Constraint on time optimal control 15

3.4.2 Constraint on fuel optimal control 16

3.5 Two point boundary value problem formulation 16

3.5.1 Direct approach to optimal control 16

3.5.2 Indirect approach to optimal control 17

3.6 Application of the indirect optimal control approach to the single gravitating body system 18

3.6.1 Time optimal Hamiltonian 18

3.6.2 Fuel optimal Hamiltonian 18

3.6.3 Costate dynamics 18

3.6.4 Reduction of the system of equations 19

3.7 Application of the indirect optimal control approach to systems with two gravitating bodies 20

3.7.1 Hamiltonian 21

3.7.2 Costate dynamics 21

3.8 Optimal control law 22

3.8.1 Time optimal control law 22

3.8.2 Fuel optimal control law 23

3.9 Choice of numerical integrator 23

3.10 Solution to the two point boundary value problem 23

4 Heliocentric Transfer Results 25

4.1 Electrical power models 25

4.1.1 Nuclear electric propulsion 25

4.1.2 Solar electric propulsion 25

4.2 Two dimensional time optimal results 26

4.2.1 Model validation 26

4.2.2 Parametric studies - Circle to circle transfers 28

4.3 2 dimensional fuel optimal results 29

4.3.1 Sample Earth-Mars fuel optimal trajectory 30

4.3.2 Power model comparison for outward transfer 31

4.3.3 Parametric study results 33

4.4 Two dimensional elliptic to ellipse transfers 34

4.4.1 Parametric studies - Impact of start location 35

4.4.2 Trajectory with multiple intermediate coasts 38

4.5 Three dimensional transfers 40

4.5.1 Sample 3D transfer 40

4.5.2 Parametric studies on 3D transfers 42

5 Geocentric Transfer Results 47
5.1 Introduction to GTO-GSO transfers 47
5.2 Sample GTO-GSO transfer 48
5.3 Parametric studies on GTO-GSO transfers 50
5.4 Fuel optimal GTO-GSO transfers 52
5.4.1 Impact of flight duration on fuel optimal GTO-GSO transfers 53
5.5 Solar gravitational effects on GTO-GSO transfers 54
5.6 Lunar gravitational effects on GTO-GSO transfers 55
5.7 Comparison with literature 56

6 Transfers with multiple gravitating bodies 59
6.1 Introduction 59
6.1.1 Frame switching with optimal control 59
6.1.2 Frame switching in the context of the current problem 60
6.2 Earth-Moon transfers 60
6.2.1 Sample Earth-Moon transfer 61
6.2.2 Parametric studies on Earth-Moon transfers 64
6.3 Earth-Mars transfers 66
6.3.1 Trajectory design splitting strategy 66
6.3.2 Earth-Mars transfer: Case studies 67
6.3.3 Effect of thrust level variation on fuel optimal Earth-Mars trajectories 72

References 75

Appendix A Differential Evolution for Low Thrust Trajectory Optimization 79
A.1 Introduction to Differential Evolution 79
A.2 Basic DE Algorithm 79
A.3 Parallelization of DE algorithm 80
A.3.1 Parallelizing DE in shared memory architecture 81
A.3.2 Parallelizing DE in distributed memory architecture 82
A.3.3 Parallelizing DE in a graphics processing unit 83
A.4 Parameter tuning for low thrust trajectory optimization 83

Appendix B Optimal Lunar Landing 85
B.1 Introduction 85
B.2 Results 85
B.2.1 Sample optimal landing trajectory 85

B.2.2 Parametric studies: Time optimal results 89
B.2.3 Parametric studies: Influence of specific impulse 91
B.2.4 Parametric studies: Fuel optimal results 92
B.3 Conclusions 93

Appendix C Variable Thrust, Variable Specific Impulse Fuel Optimal Formulation 95

List of figures

4.1 Thrust angle profile compared with Kim (2005). 27
4.2 1AU to 1.5AU minimum time transfer. 27
4.3 Transfer time with varying I_{sp}. 28
4.4 Fuel fraction with varying I_{sp}. 29
4.5 Fuel fraction with varying I_{sp}. 30
4.6 Spacecraft mass profile - fuel optimal transfer. 31
4.7 Thrust angle profile - fuel optimal transfer. 32
4.8 Semi-major axis variation - fuel optimal transfer. 33
4.9 Fuel fraction with flight duration. 34
4.10 A sample ellipse to ellipse transfer. 35
4.11 Fuel fraction variation with initial true anomaly in an ellipse to circle transfer. 36
4.12 Transfer geometry variation with initial true anomaly in an ellipse to circle transfer. 36
4.13 Fuel fraction variation with initial true anomaly in an ellipse to circle transfer. 37
4.14 Coast duration variation with initial true anomaly in an ellipse to circle transfer. 38
4.15 Sample trajectory with multiple intermediate coasts. 39
4.16 Control profile for the trajectory with multiple intermediate coasts. 39
4.17 Sample 3D heliocentric trajectory. 40
4.18 Instantaneous eccentricity profile. 41
4.19 Instantaneous inclination profile. 41
4.20 Fuel fraction with varying inclinations and flight durations. 42
4.21 Fuel fraction with varying start locations. 43
4.22 Fuel fraction with varying start locations (tighter costate bounds). 45
4.23 A 250 day trajectory starting at 60° with tighter costate bounds. 45
4.24 Inclination profile with tighter costate bounds. 46

5.1 A sample GTO to GSO transfer with 28.5° inclination change. 48

5.2 Inclination change performed by the spacecraft launched into a GTO from the Kennedy Space Center. 48
5.3 Instantaneous eccentricity profile of the spacecraft's orbit. 49
5.4 Fuel fraction dependency on launch site latitude. 50
5.5 Fuel fraction dependency on GTO argument of perigee. 51
5.6 Thrust vector plot in space. 52
5.7 Thrust vector profile. 53

6.1 Geocentric trajectory for sample transfer. 61
6.2 Selenocentric trajectory for sample transfer. 62
6.3 Radial distance profile for sample transfer. 63
6.4 Velocity magnitude profile for sample transfer. 63
6.5 Fuel fraction with varying lunar parking orbit inclination. 64
6.6 Flight duration variation with varying lunar parking orbit inclination. 65
6.7 Earth escape trajectory. 68
6.8 Mars capture trajectory. 68
6.9 Mars capture trajectory. 69
6.10 Radial distance profiles. 70
6.11 Velocity magnitude profiles. 70
6.12 Semi-major axis profiles. 71

A.1 DE performance and convergence pattern. 83

B.1 Altitude profile for time optimal descent. 86
B.2 Velocity profile for time optimal descent. 87
B.3 Thrust angle profile for time optimal descent. 87
B.4 Final phase of optimal descent trajectory. 88
B.5 Spacecraft mass variation during descent. 89
B.6 Influence of initial acceleration levels on fuel fraction. 90
B.7 Influence of initial acceleration levels on the peak to initial altitude ratios. . 90
B.8 Propellant required vs final velocity of optimal phase. 91
B.9 Influence of the flight duration on the fuel fraction and final delivered mass. 92
B.10 Fraction of time thruster is firing with varying flight duration. 93

List of tables

5.1 GTO-GSO fuel fraction comparison with varying flight duration for 500mN thrust. 53
5.2 GTO-GSO fuel fraction comparison with varying flight duration for 300mN thrust. 54
5.3 Solar gravity influence on GTO-GSO fuel fraction with varying departure epoch for 500mN thrust. 54
5.4 Lunar gravity influence on GTO-GSO fuel fraction with varying departure epoch for 500mN thrust. 55
5.5 Comparison of obtained GTO-GSO results with literature. 56

6.1 GTO-GSO fuel fraction comparison with varying flight duration for 500mN thrust. 65
6.2 Earth-Mars transfers between 500km parking orbits with varying thrust levels. 72

A.1 DE performance in a dual core 2.6GHz machine. 81

Nomenclature

a	semi-major axis with respect to the corresponding central body
$\vec{e}$	eccentricity vector with corresponding central body
g_0	gravitational acceleration of Earth at sea level
H	Hamiltonian
$\vec{h}$	angular momentum vector with corresponding central body
I_{sp}	thruster specific impulse
m	spacecraft instantaneous mass
p	semilatus rectum
r	spacecraft radial distance from origin
T	thrust level
v	spacecraft velocity seen from origin

Greek Symbols

α	spacecraft acceleration as seen by the frame
i	orbital inclination
λ	costate variable
μ	gravitational parameter
ν	true anomaly
Ω	right ascension of ascending node

ω	argument of periapsis
Φ	terminal cost function

Subscripts

c	central body
J_{fuel}	fuel optimal cost function
J_{time}	time optimal cost function
p	planet
s	sun
x	x coordinate direction
y	y coordinate direction
z	z coordinate direction

Acronyms / Abbreviations

AU	Astronomical Unit - $149.6 \times 10^{1}1$m
BR4BP	Bi-circular Restricted Four Body Problem
BVP	Boundary Value Problem
CPU	Central Processing Unit
CR3BP	Circular Restricted Three Body Problem
CR	DE Crossover Probability
DE	Differential Evolution
EPO	Earth Parking Orbit
ESA	European Space Agency
F	DE Mutation Factor
GA	Genetic Algorithm
GSO	Geosynchronous Orbit

GTO	Geosynchronous Transfer Orbit
ISRO	Indian Space Research Organization
JAXA	Japan Aerospace Exploration Agency
JD	Julian Date
LEO	Low Earth Orbit
LMO	Low Mars Orbit
MPO	Mars Parking Orbit
NASA	National Aeronautics and Space Administration
NEP	Nuclear Electric Propulsion
NLP	Nonlinear Programming Problem
NP	Number of Population Members for DE
SEP	Solar Electric Propulsion
SQP	Sequential Quadratic Programming
TPBVP	Two Point Boundary Value Problem

Chapter 1

Introduction

1.1 Low thrust propulsion systems

In order to perform maneuvers, spacecrafts must possess a system that is capable of imparting a velocity change. These are usually reaction based systems like thrusters or sails. Sails make use of the momentum transferred to the spacecraft by means of reflecting solar radiation at an appropriate angle. This enables them to perform both inward and outward transfers in the solar system. Thrusters provide the required velocity change by expelling mass in the opposite direction of the required impulse. They fall into the following broad categories,

- Cold gas thrusters
- Chemical propulsion systems
- Nuclear thermal propulsion systems
- Electric propulsion systems

Cold gas thrusters provide impulse by expelling matter stored under high pressure into the environment through a nozzle. These systems are generally inefficient. Chemical propulsion systems utilize the energy released from combustion to heat the combustion products to a high temperature before passage through the nozzle. These systems utilize the internal energy of the propellants (either mechanical or chemical) to accelerate the exhaust matter. On the other hand, electric propulsion systems energize the exhaust by supplying energy through electrical means. This requires a separate power source and a system to energize the propellant. Typically, such arrangements lead to very high exhaust velocities of the exhaust but the mass flow rate achieved is very low. This leads to a net low thrust level in comparison to the other systems. The advantage lies in the fact that for the same amount of propellant consumed, electric propulsion systems generate much higher velocity impulses. Typical thrust levels range from micro-Newtons to several hundred milli-Newtons with specific impulses ranging from several hundreds to thousands of seconds. Chemical thrusters on the other hand are capable of providing thrust levels from a few Newtons to hundreds of kilo-Newtons. Their specific impulses on the other hand range from $150s$ to $465s$ for cryogenic engines. Nuclear thermal thrusters are similar to electric thrusters in the sense that the energy to the propellant is provided through an external source. A few experimental thrusters have undergone ground testing but safety, cost and weight issues render these systems impractical as of today.

1.2 Implications of low thrust levels on orbital maneuvers

Due to the low thrust levels, it becomes necessary to continue thrusting for several days to months in order to attain appreciable changes in velocity. The immediate outcome of this is that the spacecraft trajectory no longer moves along conic sections. All orbital parameters can continuously change with time. Unlike chemical thrusters, the burn cannot be approximated as instantaneous. This has serious implications on orbital maneuvers that the spacecraft has to perform. It becomes necessary to determine the direction and magnitude of the thrust at every instant of time the thruster is firing.

1.3 Problem description

It is required to determine the thrust vector profile in order to precisely inject the spacecraft into the desired final orbit. Along with this, it is necessary to ensure that the maneuver consumes the least amount of propellant or takes the smallest flight duration based on the external constraints on the mission. This results the following,

- The spacecraft is in an initial specified orbit.
- It is desired to inject the spacecraft into a prescribed final orbit.
- The spacecraft is to perform maneuvers with continuous thrusting.
- The final orbit must be exactly achieved.
- The propellant mass or flight duration have to be minimized based on mission requirements.
- The thrust levels computed have to be within the constraints provided.

- The spacecraft trajectory is to be computed with high precision to ensure realistic mission design.
- The numerical trajectory optimization method should be computationally fast and easily amenable to parallelization.
- The method must not demand an accurate initial guess for the solution. Additionally, no prior information on coasting should be required.

Some of the problems attempted in this project are planar and three dimensional heliocentric transfers, geosynchronous transfer orbit to geosynchronous orbit transfers, transfers between Earth-Mars parking orbits of arbitrary sizes and inclinations. All these problems are posed as optimal control problems which are then solved by using an optimization technique called differential evolution. Various aspects of these transfers have been analyzed and this report serves to document the aforementioned analysis.

Chapter 2

Literature Survey

In this chapter, the work regarding low thrust spacecraft and related trajectory optimization is briefly presented. First, some papers on spacecraft equipped with low thrust systems are reviewed followed by papers on trajectory design and optimization for low thrust spacecraft. Papers on optimal control theory are also reviewed along with new developments in the field of spacecraft trajectory optimization. Survey papers by Nah et al. (2001) and Genta and Maffione (2016) are of special interest for complete transfers between planetary parking orbits. Rather than focus on the solution strategy adopted by the respective authors, these two papers are taken as benchmarks to compare the current results against. Both the papers attempt the solution to the problem of transferring a spacecraft from a low Earth orbit to a low Mars orbit. The implications of their problem formulation and solution strategy will be discussed in detail.

2.1 Low thrust spacecraft

Some of the earliest investigations on electrically propelled spacecraft were conducted by Robert Goddard and Konstantin Tsiolkovsky. Stuhlinger (1964) presented the first systematic analysis of electric propulsion systems. Electric propulsion systems have significantly evolved since the 1950s. Original designs used low boiling metals like Cesium and Mercury. Recent ion and hall effect thrusters utilize Xenon as the propellant due to it's large atomic size and ease of ionization. Since the 1960s, electric propulsion programs were established in NASA Glenn Research Center and the Jet Propulsion Laboratory. There were also several institutes in Russia established to develop electric thrusters. The Russians were the first to utilize electric propulsion for their communication satellites for station keeping. The fall of the Soviet Union prompted the introduction of their stationary plasma thrusters (SPT) series of electric propulsion systems for use on Western spacecrafts. The NTRS-NASA report by Sankovic et al. (1994) presents the results of extensive tests performed on the SPT-100 thruster conducted at NASA's Lewis Research Center. Several derivative versions of this thruster have flown on ESA missions including SMART-1 which performed a complete lunar transfer from Earth orbit (Kugelberg et al., 2004). Commercial communication spacecraft as of today have routinely used electric propulsion for both station keeping as well as for orbit raising to geosynchronous orbit. ESA's GOCE spacecraft was able to remain in a low Earth orbit at $235km$ for over eleven months due to the on board electric thruster continuously combating atmospheric drag.

NASA's Deep Space 1 was a technology demonstration probe that performed flybys past an asteroid and a comet. This was the first probe too utilize solar electric propulsion as the primary source of propulsion. The mission design details have been presented by Rayman et al. (1999). NASA's Dawn spacecraft was the successor to the Deep Space 1 probe and successfully demonstrated a velocity impulse of over $10kms^{-1}$ in flight (Rayman et al., 2006). JAXA spacecraft like the Hayabusa have also demonstrated the use of electric propulsion for deep space missions. Williams and Coverstone-Carroll (1997) and Circi (2004) discuss various solar power models for the purpose of solar electric propulsion along with some mission design details. Hoskins et al. (2013) discuss the development of electric thrusters in Aerojet Rocketdyne as well as from other organizations.

2.2 Trajectory design and optimization with low thrust spacecraft

Edelbaum (1961), in his seminal paper presented closed form analytic solutions for maneuvers including those by low thrust systems to perform large changes in orbital elements. Some of his results included closed form expressions for transfers between inclined circular orbits of different radii. Arthur. E and Ho (1975) describes a heliocentric Earth-Mars transfer using direct optimal control. This is one of the first sources that presents the use of direct optimal control theory for electric propulsion spacecraft. Rauwolf and Coverstone-Carroll (1996) applies the genetic algorithm to obtain a near optimal trajectory for the same problem. Kim (2005), in his PhD dissertation solves this problem by using the indirect approach to optimal control theory by using an adaptive algorithm combining search based and gradient methods along with homotopy and symmetry methods to obtain the solution to the resulting two point boundary value problem. The results compare well with the previously obtained results from literature.

Racca (2001) highlights the advantages of electric propulsion systems over lower specific impulse high thrust chemical thrusters with regard to missions including gravity assists. Narrowing of launch windows due to relative geometry required for planetary positions restricts the usefulness of the high thrust missions. Additionally, long cruise times lead to greatly increased operating costs and put extra loads on the spacecraft systems. Solar electric propulsion is explored as a viable alternative for such type of interplanetary missions. Yam et al. (2004) presents design strategies for low thrust missions with gravity assists using shape based representations for the spacecraft trajectories. This is a low fidelity approach and it has the assumption of the knowledge of the structure of the control. Even with the shortcomings of this technique, it is valuable to obtain an initial guess for the mission profile before a detailed trajectory optimization run. Patel et al. (2006) analyses the impact of taking different cost functionals for the trajectory optimization. External variables from the structural aspects of the spacecraft and the launch vehicle performance parameters are integrated into the formulation. Trade studies have been performed to analyze the effect of variations in the excess velocity provided, propulsion system power availability and specific impulse.

Quarta et al. (2013) utilizes a hybrid scheme involving genetic algorithm and gradient descent methods to obtain time optimal solutions to solar electric propulsion missions in the heliocentric frame of reference. The obtained solutions for solar electric propulsion spacecraft are compared with solar sail missions. It is reported that the optimal time is to be taken as the lower bound for a feasible solution in the fuel optimal framework. Betts (1998) presents a survey of different techniques for the solution to trajectory optimization problems. Issues regarding the difficulty of obtaining a solution to the two point boundary value problem arising from indirect methods to optimal control are highlighted. Chiravalle (2008) compares nuclear thermal and nuclear electric propulsion systems for interplanetary transfers. Direct methods are used where the control is parametrized as a polynomial with direct collocation to obtain the coefficients. Some disadvantages with this approach would lie in the generation of orbits with multiple revolutions with spacecrafts unless suitable coordinate systems are utilized for each individual problem.

Casalino and Simeoni (2012) uses indirect optimal control applied to electric propulsion for asteroid deflection missions. In this paper, the authors specified the thrust and coast arcs a priori with successive additions of coast arcs to move the solution to the optimum. A patched conic model is used with the assumption that the spacecraft leaves the Earth by means of chemical propulsion systems. Kluever and Pierson (1997) applies indirect optimal control for trajectory optimization using a fixed thrust-coast-thrust sequence. Analytic expressions are used to replace the initial and final circular orbits around the moon as they would slow down the numerical solution procedure and also lead to stalling in convergence for most numerical methods. The circular restricted three body formulation is used in this paper.

Nah et al. (2001) solves the problem of Earth-Mars transfer using a variable specific impulse nuclear electric propulsion system. The transfer is performed from a low Earth orbit to a low Mars orbit. Coordinate frame transformations are performed to reduce numerical sensitivity during geocentric and areocentric phases. The problem is solved using indirect optimal control and a gradient descent method. Costate jump conditions have been derived at the frame switching locations. This approach is suitable for realistic mission design and optimization as all the relevant parameters can be included in the mathematical model along with various stages of the trajectory. The authors note that at the middle of the interplanetary phase, the specific impulse rises sharply and as the system is power limited, there is a large drop in the magnitude of the thrust.

Genta and Maffione (2016) solves a similar problem as Nah et al. (2001). The difference is that the initial and final orbits about Earth and Mars are much lower. The trajectory optimization is split into multiple phases which are then patched together. The splitting is accommodated as a parameter and a parameter optimization is performed to get a globally optimal trajectory. This paper also solves the problem using solar electric propulsion. Earth-Saturn and Earth-Mercury transfers are also evaluated. The main drawback of these two papers is that the thruster is assumed to be capable of a huge thrust and specific impulse range. It is speculated that this is done to avoid solving a fuel optimal problem which would lead to a thrust-coast switching control structure. This would lead to huge difficulties in obtaining converged solutions to the boundary value problem. It is mentioned that during the phases of unrealistically high specific impulse at low thrust levels, the thrusters can be switched off leading to a coast that can potentially save fuel. This strategy is certainly viable but the extent to which the obtained solution will have to be modified to meet the final objectives is still an unknown. In the current work, a similar problem is attempted using a full ephemeris model. A single operating point is selected from the thrust and specific impulse range of the thruster used by Genta and Maffione (2016). In the current work, the problem has been solved by a fuel optimal framework with only one split of the trajectory done at the end of Earth escape. It has been consistently observed that the fuel optimal solution with a fixed thruster operating point can yield better solutions than the variable specific impulse problem solved by Genta and Maffione (2016).

2.3 Recent developments

Anderson and Lo (2009) describe trajectories in the three body framework. The impact of the invariant manifolds on the dynamics of the spacecraft is investigated. It is shown that even with no prior information, trajectory optimization algorithms tend to move towards trajectories that utilize the invariant manifolds to traverse resonances. Sánchez-Sánchez and Izzo (2018) trains deep neural networks to perform real time trajectory optimization for landing maneuvers assuming perfect information on the lander's state is known. This has the advantage of not having to solve the trajectory optimization problem by direct or indirect means thus reducing the computational requirements that is needed on board real systems. It is reported that large sets of initial states are possible to be dealt with using this method producing near optimal results. Pérez-Palau and Epenoy (2018) solve the low thrust fuel optimization problem for Earth-Moon transfer using indirect optimal control. The bi-circular restricted four body problem framework is utilized. Homotopy methods like numerical continuation have been demonstrated to be unsuitable for this purpose due to the numerical sensitivity involved. Massive exploration of the initial costate space is performed and the resulting trajectories are classified into different families based on their shape, transfer duration and fuel fraction. This search is done by backward numerical integration in order to exactly satisfy the final orbit conditions. Further analysis with dynamical systems theory is also presented. This work can yield valuable insights on initial guesses and types of trajectories to search for in a real mission design scenario. The authors are yet to transpose these results to a full ephemeris model.

Chapter 3

Problem Formulation

This chapter will include the state dynamics of the spacecraft under various both a single and multiple gravity fields and thrusting. The significance of the equations will be explained along with the relative contributions of each term to the dynamics of the spacecraft.

3.1 Spacecraft dynamics with a single central body

$$\dot{x} = v_x \tag{3.1}$$

$$\dot{y} = v_y \tag{3.2}$$

$$\dot{z} = v_z \tag{3.3}$$

$$\dot{v}_x = -\mu_c \frac{x}{r^3} + \alpha_x \tag{3.4}$$

$$\dot{v}_y = -\mu_c \frac{y}{r^3} + \alpha_y \tag{3.5}$$

$$\dot{v}_z = -\mu_c \frac{z}{r^3} + \alpha_z \tag{3.6}$$

$$\dot{m} = -\frac{m}{g_0 I_{sp}} \sqrt{\alpha_x^2 + \alpha_y^2 + \alpha_z^2} \tag{3.7}$$

The equations in sections 3.1 and 3.2 are the full three dimensional equations of motion. They can be converted to two dimensional equations by dropping the terms and equations corresponding to the out of plane component.

Equations 3.1-3.6 represent the Newton's law of motion for a spacecraft under the influence of a single central body and a thrust force. The three second order equations of motion are represented as six first order coupled differential equations. Equation 3.7 governs the variation of the mass of the spacecraft based on the thrust and specific impulse levels.

This set of equations can be used in heliocentric or planetocentric dynamics for both the fuel and time optimal problems.

3.2 Spacecraft dynamics with two gravitating bodies

This is required in planetocentric phases where the influence of the sun is to be accounted for. The equations of motion also include the non inertial effect due to the acceleration of the planet around the sun. The origin of this coordinate system is at the center of the planet. It is assumed that the sun's position is known as a function of time with respect to this origin. This formulation allows for ephemeris data to be directly used in the solution.

$$\dot{x} = v_x \tag{3.8}$$

$$\dot{y} = v_y \tag{3.9}$$

$$\dot{z} = v_z \tag{3.10}$$

$$\dot{v}_x = -\mu_p \frac{x}{r^3} + \mu_s \left[-\frac{x_s}{r_s^3} - \frac{x - x_s}{(r - r_s)^3} \right] + \alpha_x \tag{3.11}$$

$$\dot{v}_y = -\mu_p \frac{y}{r^3} + \mu_s \left[-\frac{y_s}{r_s^3} - \frac{y - y_s}{(r - r_s)^3} \right] + \alpha_y \tag{3.12}$$

$$\dot{v}_z = -\mu_p \frac{z}{r^3} + \mu_s \left[-\frac{z_s}{r_s^3} - \frac{z - z_s}{(r - r_s)^3} \right] + \alpha_z \tag{3.13}$$

$$\dot{m} = -\frac{m}{g_0 I_{sp}} \sqrt{\alpha_x^2 + \alpha_y^2 + \alpha_z^2} \tag{3.14}$$

The first term in the square brackets is the acceleration of the frame of reference (i.e planet) under two body assumptions. This constitutes a non inertial force. The second term represents the perturbing force due to the Sun's gravity field on the spacecraft. These equations can be derived by formulating the Newton's laws in the heliocentric (inertial) reference frame and then performing a coordinate transformation to the desired planet's frame. This brings in a term in the spacecraft's dynamics which corresponds to the planet's acceleration around the sun. This term is not known a priori. The planet's mass is assumed to be much smaller than that of the sun and two body dynamics is invoked to give the required acceleration. This is an approximation, albeit a good one for Earth-Moon, Earth-Sun and Mars-Sun systems. This constitutes a so called pseudo-force on the spacecraft. This force is typically three orders of magnitude lesser than the primary gravitational force of the planet when the spacecraft is in a planetary parking orbit.

3.3 Formulation of the optimal control problem

Transferring a spacecraft from one orbit to another requires the determination of a_x, a_y and a_z at each instant of time such that the final conditions are satisfied. Besides this, it is required to perform the maneuver such that either the flight duration or the fuel consumption is minimized (the choice of which depends on other mission parameters).

3.3.1 Cost functions

Time optimal cost function

$$J_{time} = \Phi_f + \int_{t_0}^{t_f} (1)dt \tag{3.15}$$

Evaluation of this integral gives the flight duration of the trajectory. This has to be minimized in the time optimal formulation. Here, the upper limit of the integration is an unknown.

Fuel optimal cost function

$$J_{fuel} = \Phi_f + \int_{t_0}^{t_f} \frac{m}{g_0 I_{sp}} \sqrt{\alpha_x^2 + \alpha_y^2 + \alpha_z^2} dt \tag{3.16}$$

In this case, the final time is kept fixed to a value greater than or equal to the time optimal flight duration with initial time set as zero. There are no fuel optimal solutions for flight durations lesser than the time optimal value. For flight durations greater than the optimal time, it is expected that the fuel fraction needed to perform the maneuver is less than the time optimal value. This is achieved through periods of coasts which lead to a net lower fuel consumption.

Terminal cost function

The error in the achievement of the final orbit conditions has to be driven down to zero for the purpose of mission design. This has to be minimized using a suitable optimization routine.

This error is represented by Φ_f and it can be expanded as follows,

$$\Phi_f = |1 - \frac{a_{achieved}}{a_{desired}}|^2 + |\hat{h}_{achieved} - \hat{h}_{desired}|^2 + |\vec{e}_{achieved} - \vec{e}_{desired}|^2 \tag{3.17}$$

This function is handled separately from the functional part of the cost function which is handled through the theory of optimal control. It is possible to develop alternative versions of this cost function depending on the requirements of the mission. If instead of a particular orbit in space, a certain point is desired, it is possible to use the state vector of the desired point directly as the cost function. The cost function presented here is singular at $|\vec{e}| = 1$ (i.e parabolic orbit). This function is well behaved for all other values of orbital elements.

3.3.2 Transformation of Cartesian state vector to semi-major axis, angular momentum and eccentricity vectors

Since the function Φ_f requires the angular momentum and eccentricity vectors while the Cartesian state vector formulation is used, it becomes necessary to perform the following conversions,

$$a = \frac{1}{\frac{2}{r} - \frac{v^2}{\mu_c}} \tag{3.18}$$

$$\vec{h} = \vec{r} \times \dot{\vec{r}} \tag{3.19}$$

$$\vec{e} = \frac{\dot{\vec{r}} \times \vec{h}}{\mu_c} - \frac{\vec{r}}{|\vec{r}|} \tag{3.20}$$

These are derived from the solution of the two body problem. This is valid as the final desired orbit is defined with it's two body orbital elements.

3.3.3 Transforming Keplerian orbital elements to state vector

The initial position of the spacecraft is specified in terms of the two body Keplerian orbital elements about a central body. This makes it essential to convert these into an initial state vector which can then be propagated. The conversion is performed as follows,

$$h = \sqrt{\mu_c a(1-e^2)} \tag{3.21}$$

$$p = a(1-e^2) \tag{3.22}$$

$$x = r(\cos\Omega\,\cos(\omega+\nu)) - \sin\Omega\,\sin(\omega+\nu)\,\cos i \tag{3.23}$$

$$y = r(\sin\Omega\,\cos(\omega+\nu)) + \cos\Omega\,\sin(\omega+\nu)\,\cos i \tag{3.24}$$

$$z = r(\sin i\,\sin(\omega+\nu)) \tag{3.25}$$

$$\dot{x} = \frac{xhe}{rp}\sin\nu - \frac{h}{r}(\cos\Omega\,\sin(\omega+\nu) + \sin\Omega\,\cos(\omega+\nu)\,\cos i) \tag{3.26}$$

$$\dot{y} = \frac{yhe}{rp}\sin\nu - \frac{h}{r}(\sin\Omega\,\sin(\omega+\nu) + \cos\Omega\,\cos(\omega+\nu)\,\cos i) \tag{3.27}$$

$$\dot{z} = \frac{zhe}{rp}\sin\nu + \frac{h}{r}\sin i\,\cos(\omega+\nu) \tag{3.28}$$

These transformations are singular for the case of $e = 1$. This implies that the initial orbit cannot be parabolic if this transformation is to be used. Hyperbolic orbits also lead to issues with this formulation. For all other values of orbital elements with elliptic orbits, there are no singularities encountered.

3.4 Constraints on the controls

The following variables α_x, α_y and α_z do have differential equations of their own. These are termed as control variables which can be independently varied. Different profiles of these controls lead to different trajectories. The control profiles have to be fixed based on the constraints due to the propulsion system and the type of problem being attempted. These constraints are to be enforced at the time of derivation of the optimal control law. They cannot be imposed after the determination of the controls from an unconstrained analysis. Thus it becomes important to know all the constraints beforehand.

3.4.1 Constraint on time optimal control

$$m\sqrt{\alpha_x^2 + \alpha_y^2 + \alpha_z^2} = T_{max} \tag{3.29}$$

This implies that in the case of the time optimal formulation, it is implicitly assumed that the thruster is to operate at full power all the time as the total magnitude of the thrust is fixed at the maximum available thrust. The direction is the only quantity that has to be determined from further analysis. It is possible to replace the strict equality with a lesser than or equal inequality. From time optimal control analysis, it is possible to prove that the optimal trajectory will occur with the thrust set to the maximum level.

3.4.2 Constraint on fuel optimal control

$$0 \leq m\sqrt{\alpha_x^2 + \alpha_y^2 + \alpha_z^2} \leq T_{max} \tag{3.30}$$

In the case of fuel optimal formulation, the thruster is allowed to utilize the full range of throttle available to it. Further optimal control analysis may reveal a bang-bang type of control where only zero and full throttle levels are required. In energy optimal formulations, it is possible that intermediate throttles can arise from the optimal control formulation.

3.5 Two point boundary value problem formulation

Based on the previous discussion, it is now evident that an optimal control problem has to be solved in order to obtain optimal spacecraft trajectories. There are two main methods for dealing with such problems.

3.5.1 Direct approach to optimal control

The optimal control problem is transformed into a nonlinear programming problem. The flight duration which is described by the independent time variable is discretized and the controls are kept as optimization variables at each point. It is the function of the optimization routine to determine the controls at each discretization point (or coefficients of a fitting function assumed) that drives the terminal cost function to zero along with minimizing the flight duration or the fuel expenditure. This method has been successful in optimizing low thrust spacecraft trajectories.

Merits of direct optimal control

- Conceptually straightforward.
- Ease of implementation.
- Physical interpretation of the optimization variables is apparent.

- Does not need smooth functions for externally available system data (i.e tabulated results can be made use of directly).

Demerits of direct optimal control

- Limited accuracy based on the fineness of the discretization.
- Long flight durations increases the problem size.
- Trajectories with multiple revolutions can be difficult to handle in the Cartesian coordinate system.
- Accurate initial guesses are needed as such problems are typically handled by gradient optimization methods due to the large size of the NLP.

3.5.2 Indirect approach to optimal control

By means of calculus of variations or by the application of Pontryagin's minimum principle (Lev Semenovich, 1987), the optimal control problem is transformed into a TPBVP. This TPBVP has to be solved in order to obtain the optimal trajectory. The optimal control law is determined as a function of the new costate variables that are introduced (Kirk, 2012). These TPBVPs can be solved by a variety of methods including shooting methods, gradient descent algorithms and evolutionary algorithms. The terminal cost function is typically set as the objective function for the optimizers with search bounds on the initial costate values that are to be determined.

Merits of indirect optimal control

- High accuracy
- Small size of the optimization problem (does not increase with flight duration).
- Guesses are needed only for the few initial costate variables.
- Powerful mathematical tools available for the optimal control analysis.

Demerits of indirect optimal control

- TPBVP solution may be very difficult due to numerical sensitivity.
- Accurate adaptive numerical integration schemes are required.

- Tabular data of system parameters cannot be used. Piecewise smooth curve fits are required a priori.
- Highly nonlinear systems may complicate the derivation of the optimal control law.

Weighing the merits and demerits, the indirect approach to optimal control has been selected as the method of choice for all the problems in this study.

3.6 Application of the indirect optimal control approach to the single gravitating body system

This requires the introduction of the costate variables $[\lambda_x\ \lambda_y\ \lambda_z\ \lambda_{v_x}\ \lambda_{v_y}\ \lambda_{v_z}\ \lambda_m]$ corresponding to the state variables $[x\ y\ z\ v_x\ v_y\ v_z\ m]$. The Hamiltonians are formed as follows,

3.6.1 Time optimal Hamiltonian

$$\begin{aligned} H_{time} = 1 - \lambda_m \left(\frac{m\sqrt{\alpha_x^2 + \alpha_y^2 + \alpha_z^2}}{g_0 I_{sp}} \right) + \lambda_x v_x + \lambda_y v_y + \lambda_z v_z + \lambda_{v_x} \left(-\frac{\mu_c x}{r^3} + \alpha_x \right) \\ + \lambda_{v_y} \left(-\frac{\mu_c y}{r^3} + \alpha_y \right) + \lambda_{v_z} \left(-\frac{\mu_c z}{r^3} + \alpha_z \right) \end{aligned} \tag{3.31}$$

3.6.2 Fuel optimal Hamiltonian

$$\begin{aligned} H_{fuel} = (1 - \lambda_m) \left(\frac{m\sqrt{\alpha_x^2 + \alpha_y^2 + \alpha_z^2}}{g_0 I_{sp}} \right) + \lambda_x v_x + \lambda_y v_y + \lambda_z v_z + \lambda_{v_x} \left(-\frac{\mu_c x}{r^3} + \alpha_x \right) \\ + \lambda_{v_y} \left(-\frac{\mu_c y}{r^3} + \alpha_y \right) + \lambda_{v_z} \left(-\frac{\mu_c z}{r^3} + \alpha_z \right) \end{aligned} \tag{3.32}$$

3.6.3 Costate dynamics

The costate dynamics provides us with an additional set of ordinary differential equations that have to be solved. This system is required to complete the TPBVP as the optimal control law is a function of the costates at every time instant.

Time optimal costate dynamics

$$\dot{\lambda}_x = -\frac{\partial H_{time}}{\partial x} = -\lambda_{v_x}\left[-\frac{mu_c}{r^3}+\frac{3\mu_c x}{r^4}\frac{\partial r}{\partial x}\right] - \lambda_{v_y}\left[\frac{3\mu_c y}{r^4}\frac{\partial r}{\partial x}\right] - \lambda_{v_z}\left[\frac{3\mu_c z}{r^4}\frac{\partial r}{\partial x}\right] \tag{3.33}$$

$$\dot{\lambda}_y = -\frac{\partial H_{time}}{\partial y} = -\lambda_{v_x}\left[\frac{3\mu_c x}{r^4}\frac{\partial r}{\partial y}\right] - \lambda_{v_y}\left[-\frac{mu_c}{r^3}+\frac{3\mu_c y}{r^4}\frac{\partial r}{\partial y}\right] - \lambda_{v_z}\left[\frac{3\mu_c z}{r^4}\frac{\partial r}{\partial y}\right] \tag{3.34}$$

$$\dot{\lambda}_z = -\frac{\partial H_{time}}{\partial z} = -\lambda_{v_x}\left[\frac{3\mu_c x}{r^4}\frac{\partial r}{\partial z}\right] - \lambda_{v_y}\left[\frac{3\mu_c y}{r^4}\frac{\partial r}{\partial z}\right] - \lambda_{v_z}\left[-\frac{mu_c}{r^3}+\frac{3\mu_c z}{r^4}\frac{\partial r}{\partial z}\right] \tag{3.35}$$

$$\dot{\lambda}_{v_x} = -\frac{\partial H_{time}}{\partial v_x} = -\lambda_x \tag{3.36}$$

$$\dot{\lambda}_{v_y} = -\frac{\partial H_{time}}{\partial v_y} = -\lambda_y \tag{3.37}$$

$$\dot{\lambda}_{v_z} = -\frac{\partial H_{time}}{\partial v_z} = -\lambda_z \tag{3.38}$$

$$\dot{\lambda}_m = -\frac{\partial H_{time}}{\partial m} = -\frac{\lambda_m\sqrt{\alpha_x^2+\alpha_y^2+\alpha_z^2}}{g_0 I_{sp}} \tag{3.39}$$

$$\frac{\partial r}{\partial x} = \frac{x}{r} \qquad \frac{\partial r}{\partial y} = \frac{y}{r} \qquad \frac{\partial r}{\partial z} = \frac{z}{r} \tag{3.40}$$

Fuel optimal costate dynamics

The costate dynamics for the fuel optimal problem is the same as the time optimal formulation except for the following modification to the costate equation corresponding to the spacecraft mass,

$$\dot{\lambda}_m = -\frac{\partial H_{fuel}}{\partial m} = -(1-\lambda_m)\frac{\sqrt{\alpha_x^2+\alpha_y^2+\alpha_z^2}}{g_0 I_{sp}} \tag{3.41}$$

When the state and costate equations are grouped together for the three dimensional problem, a set of 14 ordinary differential equations are obtained and these have to be simultaneously propagated in time.

3.6.4 Reduction of the system of equations

From a careful analysis of the above systems of equations, it is possible to verify the following results,

Time optimal formulation

$$\dot{m}\lambda_m = \dot{\lambda}_m m \tag{3.42}$$

This identity can be used to eliminate the differential equation for λ_m and replace it by,

$$\lambda_m(t_2) = K\lambda_m(t_1)\frac{m(t_2)}{m(t_1)} \tag{3.43}$$

Here K is an arbitrary constant that can be set to any desired value. The other costates will scale accordingly.

Fuel optimal formulation

$$m(1-\lambda_m) = Q \tag{3.44}$$

Here Q is a conserved quantity, the value of which can be set to any value with the other costates scaling accordingly.

The validity of the above equations can be checked by substitution and differentiation. It is possible to utilize these relations to reduce the system of equations by 1. This corresponds to roughly a 7% decrease in computational time. In the current project, the full set of equations is integrated to check whether the solution procedure utilized is capable of satisfying these identities without any extra information. It may be possible to derive other such conserved quantities if differentiable symmetries in the system can be identified. This is in accordance to Noether's theorems of classical mechanics as the state and costate dynamics can be represented as the result of a Hamiltonian formulation. This has not yet been attempted and can be the subject of future investigation.

3.7 Application of the indirect optimal control approach to systems with two gravitating bodies

This formulation can provide the optimal control law in the case of motion in the planetary sphere of influence along with solar perturbations to the motion. It is also possible to apply the same to the Earth-Moon and other similar systems. This formulation is more general than the restricted three body dynamics as direct ephemeris data on the relative positions of the gravitating bodies can be used for highly accurate realistic trajectory design and optimization.

In case only the primary secondary body is required, the other terms can be shut off and the formulation collapses to that of a single body. Here, only the fuel optimal formulation will be presented.

3.7.1 Hamiltonian

The fuel optimal Hamiltonian in the two gravitating body, planetocentric framework is as follows,

$$\begin{aligned} H_{fuel} &= (1-\lambda_m)\left(\frac{m\sqrt{\alpha_x^2+\alpha_y^2+\alpha_z^2}}{g_0 I_{sp}}\right) + \lambda_x v_x + \lambda_y v_y + \lambda_z v_z \\ &+ \lambda_{v_x}\left[-\frac{\mu_p x}{r^3} - \mu_s\left(\frac{x_s}{r_s^3} + \frac{x-x_s}{(r-r_s)^3}\right) + \alpha_x\right] + \lambda_{v_y}\left[-\frac{\mu_p y}{r^3} - \mu_s\left(\frac{y_s}{r_s^3} + \frac{y-y_s}{(r-r_s)^3}\right) + \alpha_y\right] \\ &+ \lambda_{v_z}\left[-\frac{\mu_p z}{r^3} - \mu_s\left(\frac{z_s}{r_s^3} + \frac{z-z_s}{(r-r_s)^3}\right) + \alpha_z\right] \end{aligned} \tag{3.45}$$

3.7.2 Costate dynamics

From the appropriate partial derivatives of the Hamiltonian, the costate dynamics can be derived as follows,

$$\psi = -\frac{\mu_p}{r^3} - \frac{\mu_s}{(r-r_s)^3} \tag{3.46}$$

$$\varepsilon_x = \frac{\mu_p x}{r^4} + \frac{\mu_s(x-x_s)}{(r-r_s)^4} \tag{3.47}$$

$$\varepsilon_y = \frac{\mu_p y}{r^4} + \frac{\mu_s(y-y_s)}{(r-r_s)^4} \tag{3.48}$$

$$\varepsilon_z = \frac{\mu_p z}{r^4} + \frac{\mu_s(z-z_s)}{(r-r_s)^4} \tag{3.49}$$

$$\dot{\lambda}_x = -\lambda_{v_x}\left[\psi + 3\frac{x}{r}\varepsilon_x\right] - \lambda_{v_y}\left[3\frac{x}{r}\varepsilon_y\right] - \lambda_{v_z}\left[3\frac{x}{r}\varepsilon_z\right] \tag{3.50}$$

$$\dot{\lambda}_y = -\lambda_{v_x}\left[3\frac{y}{r}\varepsilon_x\right] - \lambda_{v_y}\left[\psi + 3\frac{y}{r}\varepsilon_y\right] - \lambda_{v_z}\left[3\frac{y}{r}\varepsilon_z\right] \tag{3.51}$$

$$\dot{\lambda}_z = -\lambda_{v_x}\left[3\frac{z}{r}\varepsilon_x\right] - \lambda_{v_y}\left[3\frac{z}{r}\varepsilon_y\right] - \lambda_{v_z}\left[\psi + 3\frac{z}{r}\varepsilon_z\right] \tag{3.52}$$

$$\dot{\lambda}_{v_x} = -\lambda_x \tag{3.53}$$

$$\dot{\lambda}_{v_y} = -\lambda_y \tag{3.54}$$

$$\dot{\lambda}_{v_z} = -\lambda_z \tag{3.55}$$

$$\dot{\lambda}_m = -\frac{(1-\lambda_m)\sqrt{\alpha_x^2+\alpha_y^2+\alpha_z^2}}{g_0 I_{sp}} \tag{3.56}$$

The above system of differential equations require x_s, y_s, z_s and r_s to be known as an explicit function of time. This can be obtained either through looking up an ephemeris or by analytic series expansion. For the purposes of this project, the JPL ephemeris DE430 has been exclusively utilized wherever necessary.

3.8 Optimal control law

The optimal control law is derived using the Pontryagin's minimum principle. It states that the control which minimizes the cost functional also minimizes the Hamiltonian when evaluated along the optimal trajectory. It can be mathematically written as follows,

$$\vec{\alpha}^* = argmin\{H(\vec{x}^*, \vec{\lambda}^*, \vec{\alpha}))\} \tag{3.57}$$

The starred quantities represent the respective state and costate vectors as evaluated on the optimal trajectories. $\vec{\alpha}^*$ is the vector of optimal controls and $\vec{\alpha}$ is a vector of only the admissible controls. This is where the control constraints come into play, the minimization of the Hamiltonian must be performed only in the set of feasible controls. This is a constrained minimization problem. For both the single gravitating body and two gravitating body models, the same control law is obtained.

3.8.1 Time optimal control law

In this case, the minimization is performed with an equality constraint. The method of Lagrange multipliers will suffice. The control law is obtained as follows,

$$\alpha_x = -\frac{T_{max}\lambda_{v_x}}{m\sqrt{\lambda_{v_x}^2+\lambda_{v_y}^2+\lambda_{v_z}^2}} \tag{3.58}$$

$$\alpha_y = -\frac{T_{max}\lambda_{v_y}}{m\sqrt{\lambda_{v_x}^2+\lambda_{v_y}^2+\lambda_{v_z}^2}} \tag{3.59}$$

$$\alpha_z = -\frac{T_{max}\lambda_{v_z}}{m\sqrt{\lambda_{v_x}^2+\lambda_{v_y}^2+\lambda_{v_z}^2}} \tag{3.60}$$

3.8.2 Fuel optimal control law

In this case, the minimization is performed with an inequality constraint. The Karush-Kuhn-Tucker conditions need to be applied to perform this minimization. The control law along with a switching condition is obtained as follows,

$$l = \frac{\sqrt{\lambda_{v_x}^2 + \lambda_{v_y}^2 + \lambda_{v_z}^2}}{m} - \frac{1 - \lambda_m}{g_0 I_{sp}} \tag{3.61}$$

$$k = -\frac{T_{max}/m}{\sqrt{\lambda_{v_x}^2 + \lambda_{v_y}^2 + \lambda_{v_z}^2}} \tag{3.62}$$

$$\begin{cases} \text{If } l \geq 0, & \alpha_x = k\lambda_{v_x} \quad \alpha_y = k\lambda_{v_y} \quad \alpha_z = k\lambda_{v_z} \\ \text{If } l < 0, & \alpha_x = 0 \quad \alpha_y = 0 \quad \alpha_z = 0 \end{cases} \tag{3.63}$$

3.9 Choice of numerical integrator

The above sets of equations have to be numerically propagated with the given initial conditions. High order, adaptive step size integrators namely the Runge-Kutta-Fehlberg 7(8) scheme or higher are desirable to maintain accuracy while taking large step sizes. Adaptive step size is mandatory as the physics allows for large durations of gradual motion with small rapid movement phases. This can lead to unacceptably large errors if fixed time steps are used. Also, due to the aperiodicity of the solutions in case of non zero thrusting, it is impossible to obtain accurate information on the minimum required step size. Operating at too low step sizes with lower order integrators can lead to huge roundoff errors. Extremely high order schemes like the Runge-Kutta-Feagin schemes (Feagin, 2007) require large computational effort per time step with diminishing returns on accuracy. This is the reason why the adaptive Runge-Kutta-Fehlberg 7(8) scheme has been the primary choice for all the problems investigated in this project.

3.10 Solution to the two point boundary value problem

Differential evolution, a search based global optimization method developed by Storn and Price (1997) is used to solve the TPBVP. The initial costates are set as the optimization variables and the terminal cost function is to be minimized. Every objective function evaluation involves the numerical integration of the trajectory. Differential evolution controls the search based on the operations of crossover, mutation and selection. The algorithm is also elitist leading to rapid convergence. The following steps are to be followed while solving the optimal control trajectory problem.

- Specify initial conditions.
- Transform all given initial conditions to state vector form.
- Form the specified number of random population members based on the NP value.
- The initial costates have to be chosen between the specified bounds.
- Perform the DE algorithm. (Details in Appendix A).
- The DE algorithm in this work is implemented in parallel. Each computer core concurrently propagates and evaluates a trajectory.
- The cost function to be minimized is the terminal cost function. It represents the error in the achievement of the final desired orbit.
- Once the cost function goes below a desired tolerance level, the DE iterations can be terminated.
- The result of this procedure is a set of initial costates.
- These initial costates when used to propagate the state and costate dynamics, lead to an optimal trajectory that delivers the spacecraft from the initial orbit to the desired final orbit.

Chapter 4

Heliocentric Transfer Results

In this chapter the two dimensional time and fuel optimal problems are solved in the heliocentric coordinate system. Both nuclear and solar electric propulsion system models have been considered. The results are presented and analyzed.

4.1 Electrical power models

4.1.1 Nuclear electric propulsion

This type of propulsion system is powered by a nuclear reactor. The power output is roughly constant. For a conventional electric thruster, the thrust produced and specific impulse can be assumed to be constant.

4.1.2 Solar electric propulsion

This form of power system is typically powered by solar arrays that generate electric power. It is assumed that the panels are controlled to face the sun at all times except during eclipses when zero power is available.

Inverse square model

This is the simplest model and is usually taken as the first approximation for the thrust produced. The generated power produced varies as the inverse square of the distance from the sun. It is assumed that the thrust varies linearly with the power supply and that the specific impulse is constant.

Coverstone-Carroll model

This is a significantly more complex model and accounts for the saturation of power generation as the solar distance decreases. This is obtained from a fit based on experimental data. More details on the model are available in the paper by Williams and Coverstone-Carroll (1997). The model is as follows,

$$a_1 = 0.7119713 \tag{4.1}$$

$$a_2 = 0.4089753 \tag{4.2}$$

$$a_3 = -0.0783905 \tag{4.3}$$

$$a_4 = -0.0201896 \tag{4.4}$$

$$a_5 = 0.0623406 \tag{4.5}$$

$$P = \frac{P_0}{r^2}\left[\frac{a_1 + \frac{a_2}{r} + \frac{a_3}{r^2}}{1 + a_4 r + a_5 r^2}\right] \tag{4.6}$$

Alternative models

From the mathematical formulation provided in the previous chapter, since the maximum allowable thrust and specific impulse are external parameters to the system of equations, it is possible to define any custom piecewise smooth variation for the aforementioned quantities. These can be integrated into the dynamics of the problem and the corresponding optimal trajectories can be obtained.

4.2 Two dimensional time optimal results

This section presents the results of time optimal transfers between two heliocentric orbit.

4.2.1 Model validation

The code and mathematical formulation are validated by solving a well documented problem of a 1AU to 1.5AU transfer for a 1000kg NEP spacecraft with 1N thrust and I_{sp} of 6000s.

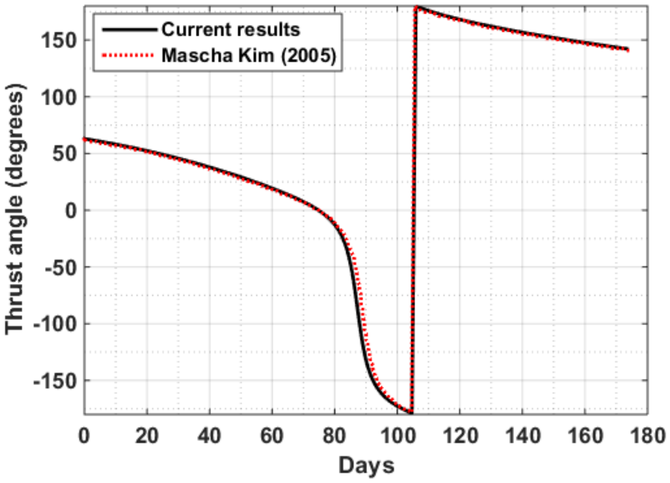

Fig. 4.1 Thrust angle profile compared with Kim (2005).

This is a classic problem that has been solved by both direct (Arthur. E and Ho, 1975) and indirect (Kim, 2005) methods. As seen from figure 4.1, it is seen that the current solution strategy and mathematical formulation closely match the values from literature. This provides confidence for the proposed strategy which makes use of differential evolution. The corresponding time optimal trajectory looks as follows,

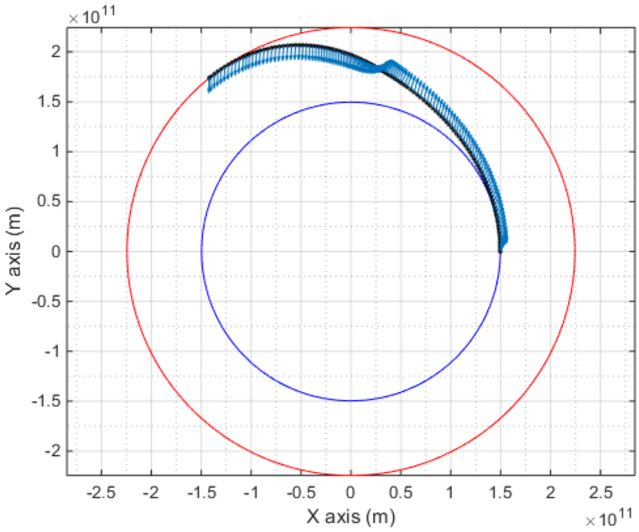

Fig. 4.2 1AU to 1.5AU minimum time transfer.

The blue arrows depict the instantaneous thrust vector. This plot reveals that there is a large rotation of the thrust vector required during the mid portion of the trajectory. Due to the requirement of time optimality, there is a substantial thrust component off the tangent with the thruster operating for a longer duration. This leads to higher fuel consumption but the flight duration is minimized. These trajectories may be suitable for human missions in outer space.

4.2.2 Parametric studies - Circle to circle transfers

The following is the result of a circle to circle transfers from 1AU to 1.5AU with varying thrust levels and specific impulse values. The following results are obtained.

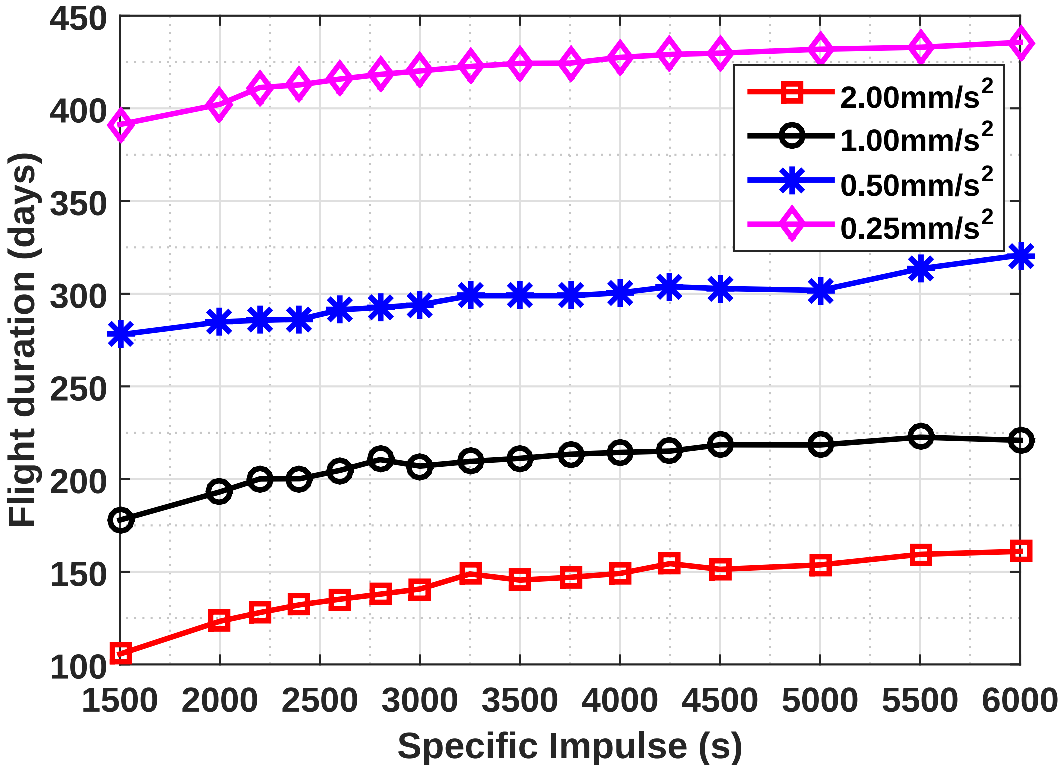

Fig. 4.3 Transfer time with varying I_{sp}.

From figure 4.3, it is visible that the transfer time varies by about 50 days when the specific impulse is varied from 1500 to 6000. This indicates that the flight duration for higher specific impulse is relatively insensitive. For varying acceleration levels, it is clear that the transfer time is highly sensitive. A factor of 8 reduction in acceleration led to an increase in flight duration by a factor of 4.

For very low thrust levels, the transfer takes the form of multiple revolutions around the sun. These types of orbits are challenging to solve using the direct approach in the Cartesian coordinate system. The approach followed in this investigation faces no such issues to the solution.

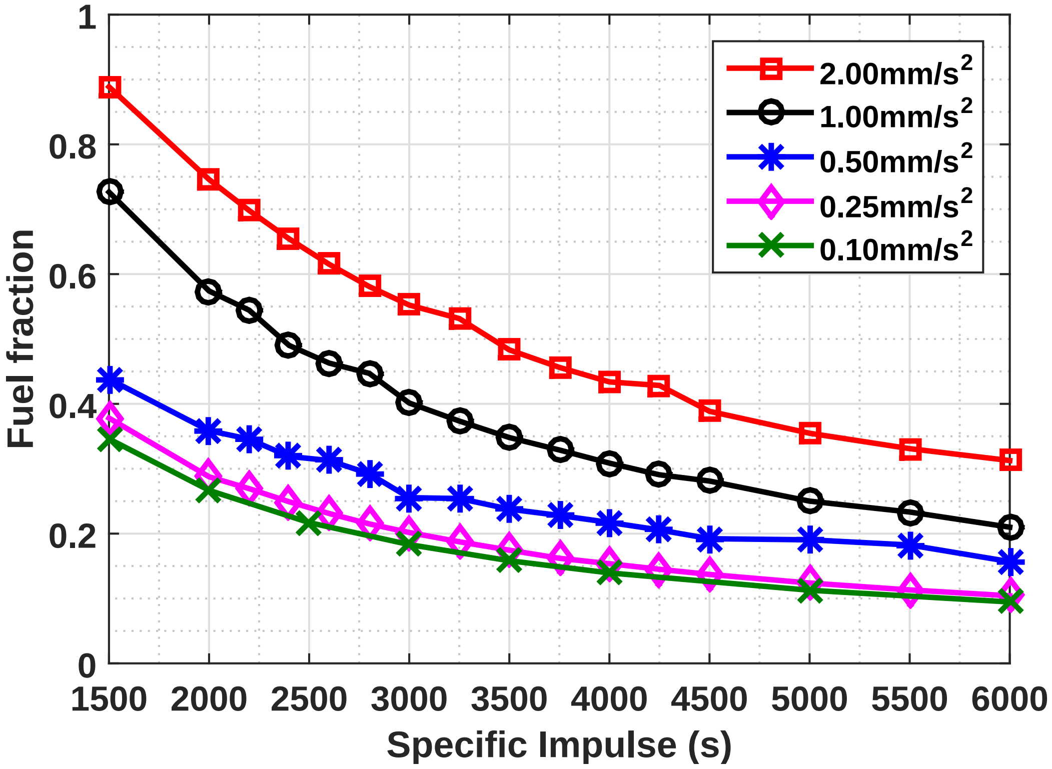

Fig. 4.4 Fuel fraction with varying I_{sp}.

Figure 4.4 shows the dependence of the propellant fraction on the specific impulse in the minimum time formulation. As expected, lower specific impulse leads to a high propellant consumption. The most important observation to make here is that the propellant consumption stagnates and reaches a minimum limiting value for very low acceleration levels. This suggests that lowering the thrust hoping to achieve lower fuel fractions at the cost of flight duration is a strategy that provides diminishing returns beyond a certain extent.

4.3 2 dimensional fuel optimal results

These type of transfers allow for the spacecraft to coast with the thrusters switched off. At the expense of a higher flight duration, significant savings in terms of propellant can be achieved. The flight duration of the corresponding minimum time problem is the lower limit of the flight duration for this case. If the two flight durations are equal, then the fuel optimal and time optimal solutions coincide. If the flight duration for the fuel optimal case is set to a value lower than the minimum time, no solution can be found. Setting a flight duration greater than the minimum time value leads to solutions with coasting. The objective of this work is to ensure that the coast arises naturally from the solution procedure with no information supplied by the user. This is to avoid the requirement of the knowledge of the structure of the control as there can be trajectories with multiple coast phases.

4.3.1 Sample Earth-Mars fuel optimal trajectory

The trajectory for a 400 day fuel optimal Earth-Mars orbit transfer with a 2000s I_{sp} and a thrust level of 236mN.

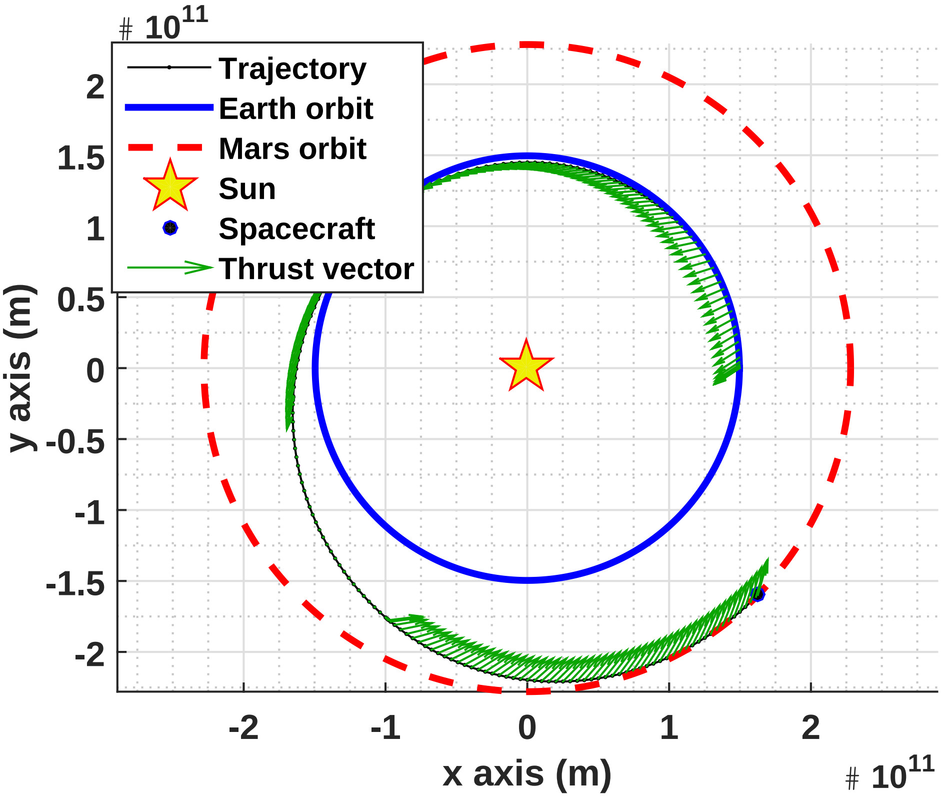

Fig. 4.5 Fuel fraction with varying I_{sp}.

Several important features can be observed in figure 4.5. During the start of the orbit, the thrust is radially inward and has a small retrograde component which gradually rotates to a tangential value. It is speculated that this maneuver occurs to enable longer thrusting in a higher velocity region closer to the sun. If the flight duration is increased, this tendency disappears. The initial thrust phase is followed by a coast duration. Here, the spacecraft flies in a Keplerian orbit. No information is provided to the numerical method a-priori about the location and duration of the coast. It is automatically determined. The final leg of the trajectory is a thrusting phase with a radially inward thrust. This is to perform the circularize the final orbit around the sun at 1.524AU. The rotation of the thrust vector is seen to be very gradual. This implies that very low thrust, precision attitude control thrusters can be made use of. The attitude control requirement is estimated to be in the range of micro-Newtons to a few milli-Newtons depending on the size and shape of the spacecraft. This can be performed by smaller auxiliary electric thrusters.

4.3.2 Power model comparison for outward transfer

Here, a 200 day fuel optimal transfer from 1AU to 1.524AU for a 1000kg spacecraft with a 1N, 2000s I_{sp} thruster.

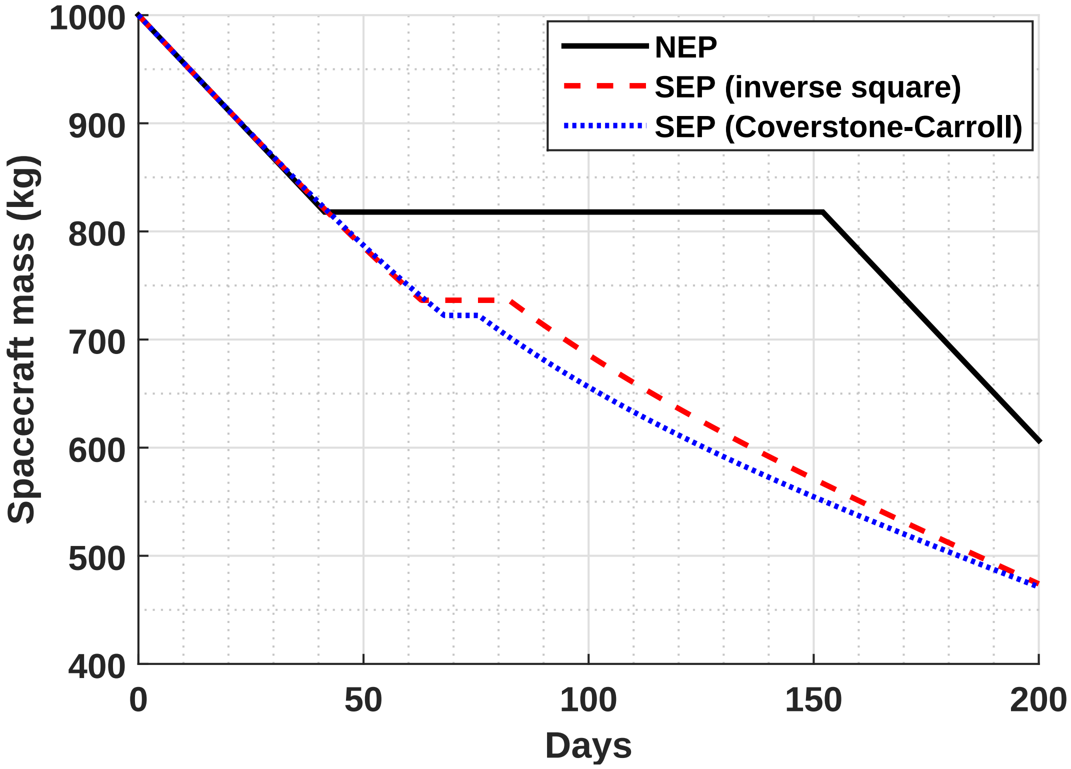

Fig. 4.6 Spacecraft mass profile - fuel optimal transfer.

Figure 4.6 shows the spacecraft instantaneous mass profile under different power models. It is seen that NEP has an advantage of over 10% in comparison to both SEP models used. The coast duration is also seen to be much larger. The inverse square dependency on thrust is visible for the SEP models as the slope of the mass profile in the final thrust phase is seen to vary in a decreasing fashion as the spacecraft moves away from the sun.

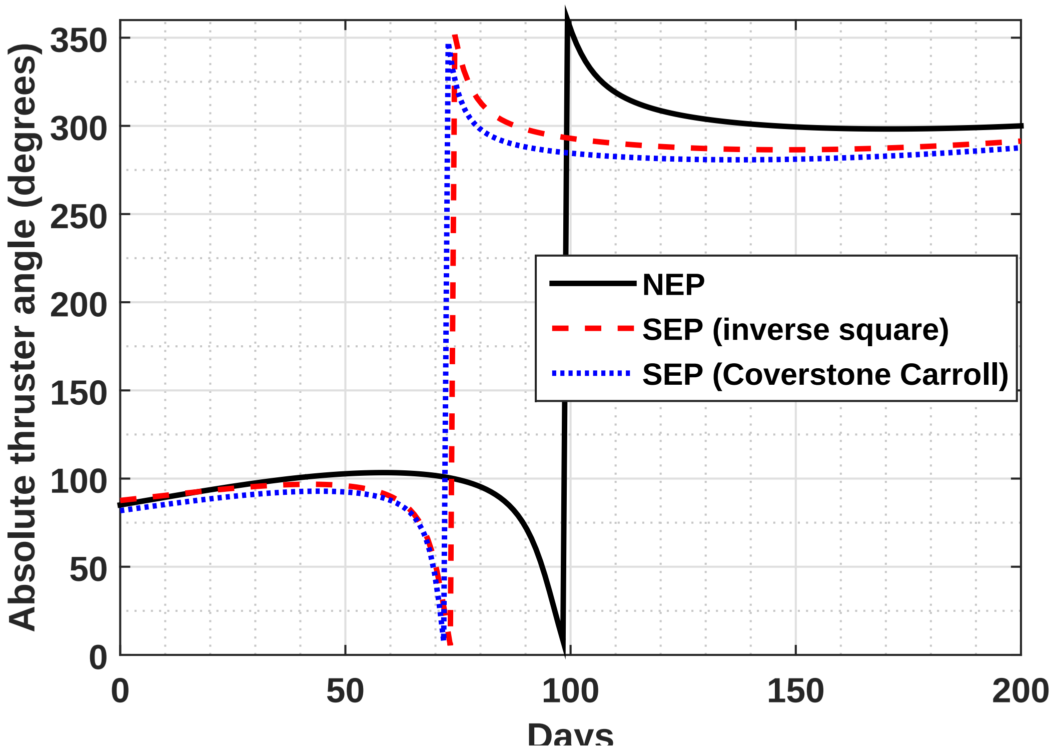

Fig. 4.7 Thrust angle profile - fuel optimal transfer.

Figure 4.7 shows the variation of the absolute thrust angle. It is clearly visible that the rapid change in thrust direction occurs in the middle of the coast duration. Since the thruster is inactive in this phase, there are no attitude control requirements and only the initial and final phases of the trajectory count for attitude control requirement determination. This implies that the fuel optimal trajectory is much more benign than the time optimal trajectory in terms of maximum attitude control requirements. micro-Newton thrust levels are sufficient to achieve this profile depending on the spacecraft mass and moment of inertia. Accurate determination of the attitude control requirements and dynamics will require a detailed 6DOF simulation.

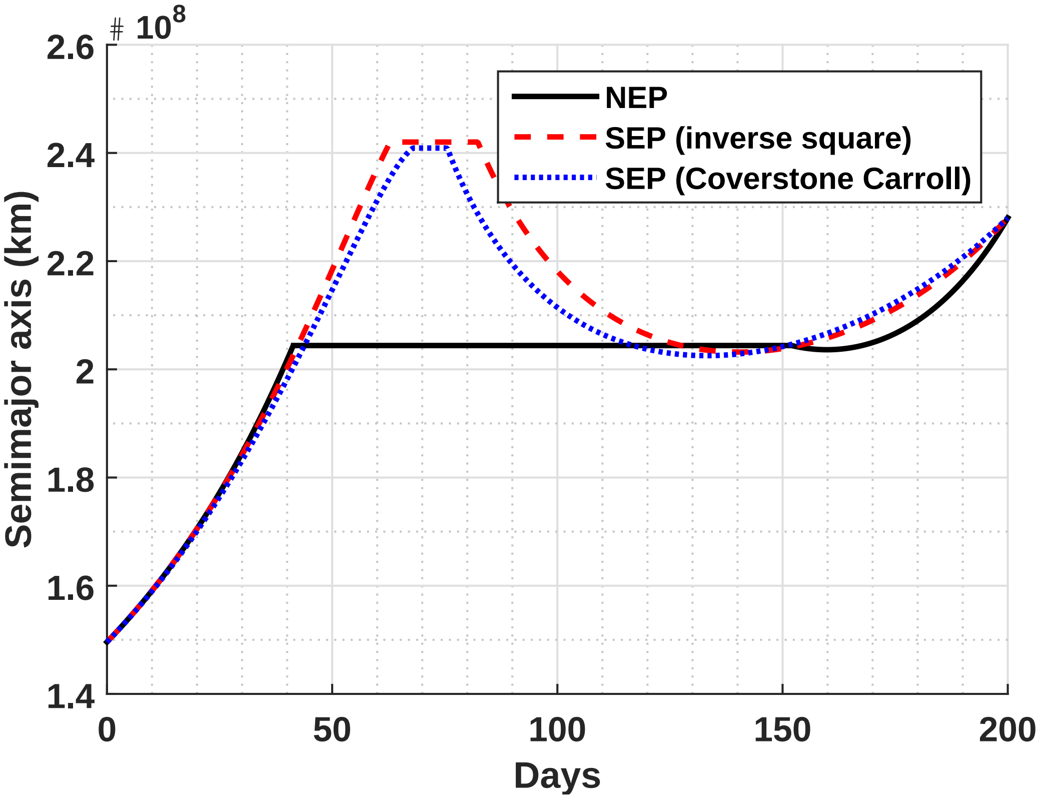

Fig. 4.8 Semi-major axis variation - fuel optimal transfer.

Figure 4.8 shows the semi-major axis variation with time for the same transfer with different power models. It is seen that both the solar electric models drive the semi-major axis to a high level and then thrust to reduce it to the required level. This is due to the 200 day flight duration that has been specified. NEP on the other hand has a much longer coast and the increase in semi-major axis is much lesser. Semi-major axis is representative of the energy state of the spacecraft. It is evident that for this outward transfer, NEP does not waste much energy in comparison to SEP models. From the figure, even the NEP model shows a slight dip in semi-major axis after the end of the coast. This suggests that a modest increase in flight time will eliminate this loss. For the case of SEP, much longer flight durations are needed for the propellant consumption to approach NEP levels.

4.3.3 Parametric study results

For the same problem as before, the flight duration is varied from 200 days to 300 days and the corresponding fuel optimal results are presented as a parametric study.

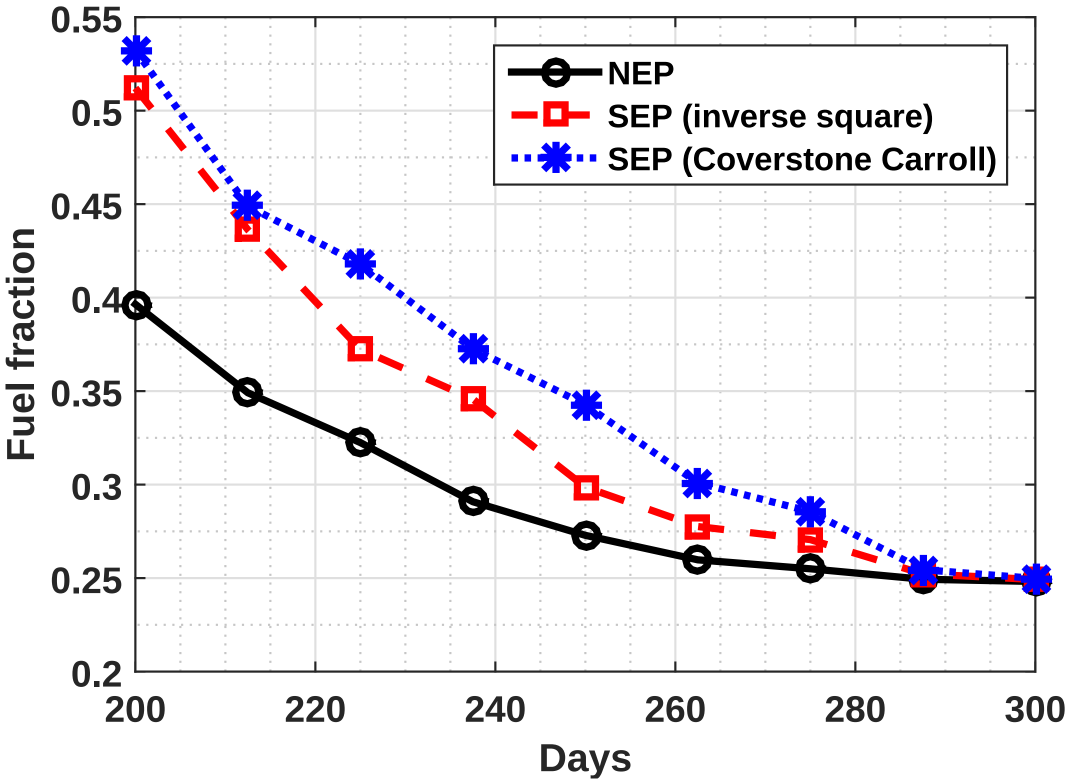

Fig. 4.9 Fuel fraction with flight duration.

Figure 4.9 shows the trend in propellant required with increasing flight duration. It is seen that with increase in flight duration, all power models require lower propellant mass. It is also visible that this trend stagnates at higher flight durations and all the three power models tend to converge to the same fuel fraction value. The primary advantage of NEP is in outward transfers with low flight durations. This is due to the rapid loss of the maximum available thrust that SEP models face at higher distances from the sun. This situation reverses during inward travel where equal performing SEP and NEP thrusters at the starting point will ensure that the SEP thruster outperforms NEP once the trajectory moves closer to the sun.

4.4 Two dimensional elliptic to ellipse transfers

For demonstration, a transfer from a fictitious 0.4AU perihelion orbit with eccentricity 0.5 to a 1.524AU perihelion orbit with eccentricity 0.1 is performed with NEP. The initial acceleration level is $1mm/s^2$ with 2000s I_{sp}. The angle between the line of apsides is 225 degrees. Figure 4.10 shows this transfer. The spacecraft starts at the aphelion.

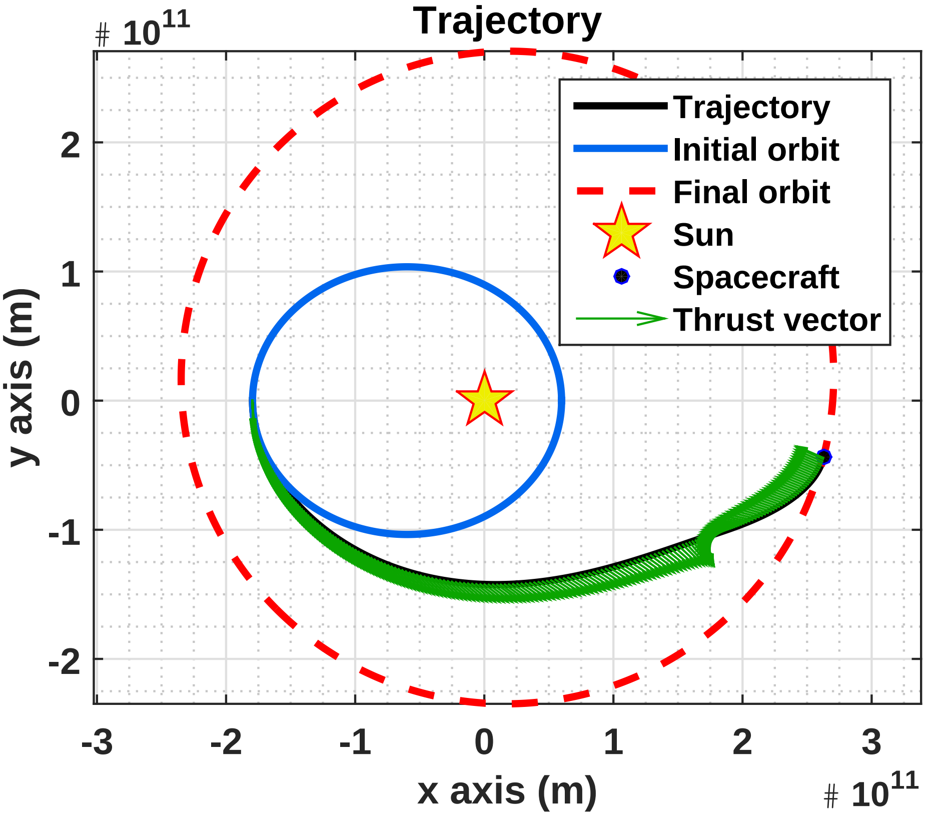

Fig. 4.10 A sample ellipse to ellipse transfer.

4.4.1 Parametric studies - Impact of start location

Time optimal ellipse-circle transfer

Here, a transfer is considered from the 0.4AU perihelion, 0.5 eccentricity orbit to a 1.524AU circular orbit around the sun with NEP. The initial acceleration is $1mm/s^2$ with 2000s I_{sp}. the starting location is varied on the initial elliptic orbit. The fuel fraction and transfer angle geometry is seen to be a strong function of this starting true anomaly on the initial orbit. A swing of about 25% is seen in the required fuel fraction in these transfers.

Figure 4.11 shows the fuel fraction needed with varying initial true anomalies in the time optimal framework. It is seen that the maximum propellant consumption occurs when the spacecraft starts in the vicinity of the perihelion. The minimum occurs at a true anomaly of approximately 120°. This plot reveals that from such an orbit, it may be preferable to coast initially until the optimum true anomaly is attained. This information is obtained without having to solve the numerically difficult fuel optimal problem.

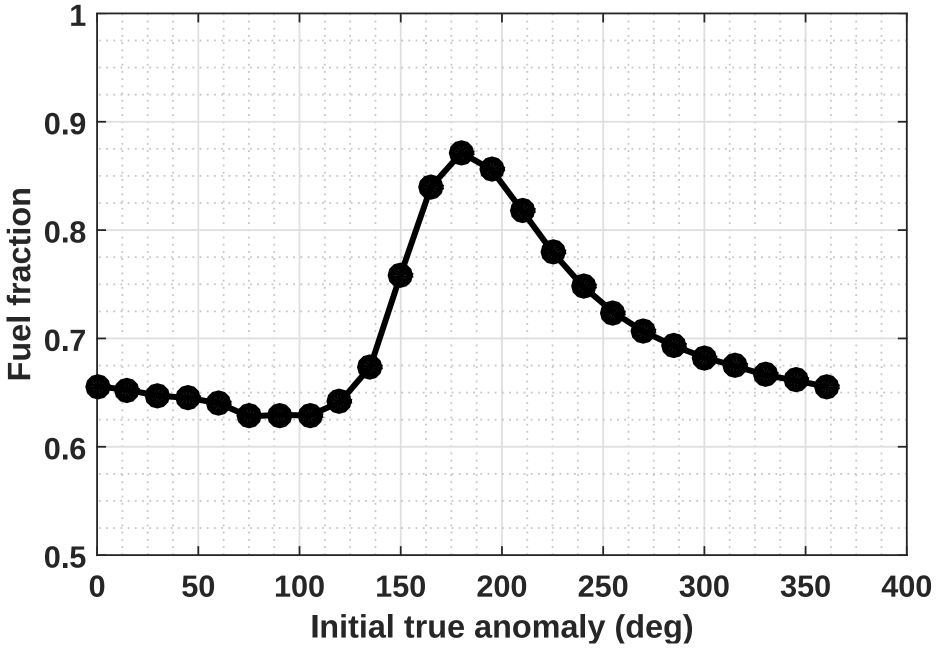

Fig. 4.11 Fuel fraction variation with initial true anomaly in an ellipse to circle transfer.

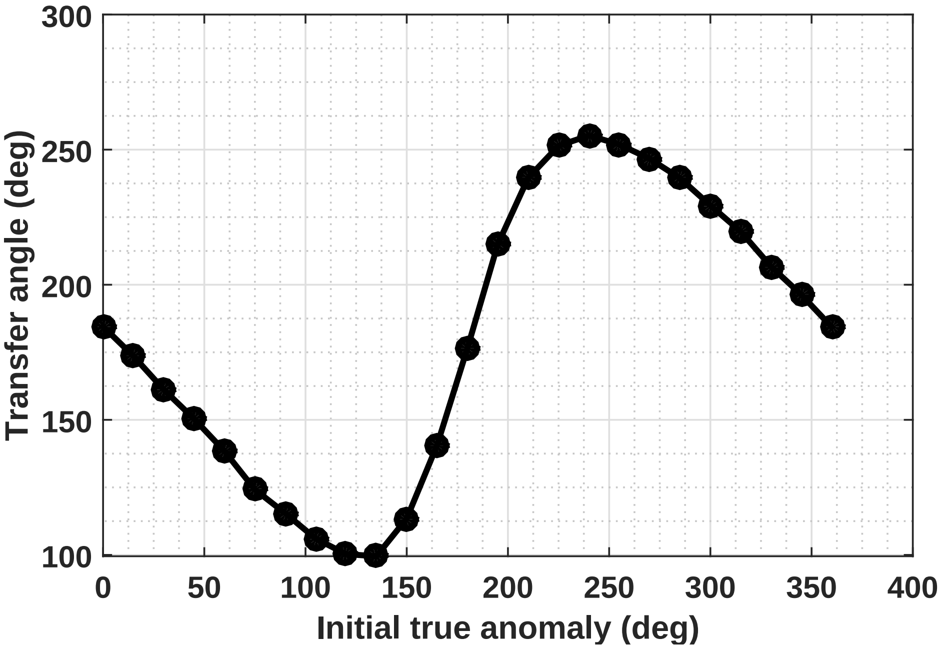

Fig. 4.12 Transfer geometry variation with initial true anomaly in an ellipse to circle transfer.

Figure 4.12 reveals a tentative reason for the minimum fuel consumption at 120° initial true anomaly. It is seen that the transfer angle needed for this case is a minimum. This observation must be made with caution as a similar result is not seen at transfers from the aphelion. Even though at 250° true anomaly, the transfer angle reaches a maximum, the fuel consumption for transfers from this location is not high as the spacecraft is now in the vicinity of the perihelion where it moves rapidly and the transfer is completed faster than those from the aphelion. The peak fuel consumption depending on when the combination of initial radial distance from the sun and transfer geometry take on the most unfavorable values rather than the value of any individual parameter.

Fuel optimal ellipse-circle transfer

Here, 225 day transfers from between the same orbit as in the previous case are considered.

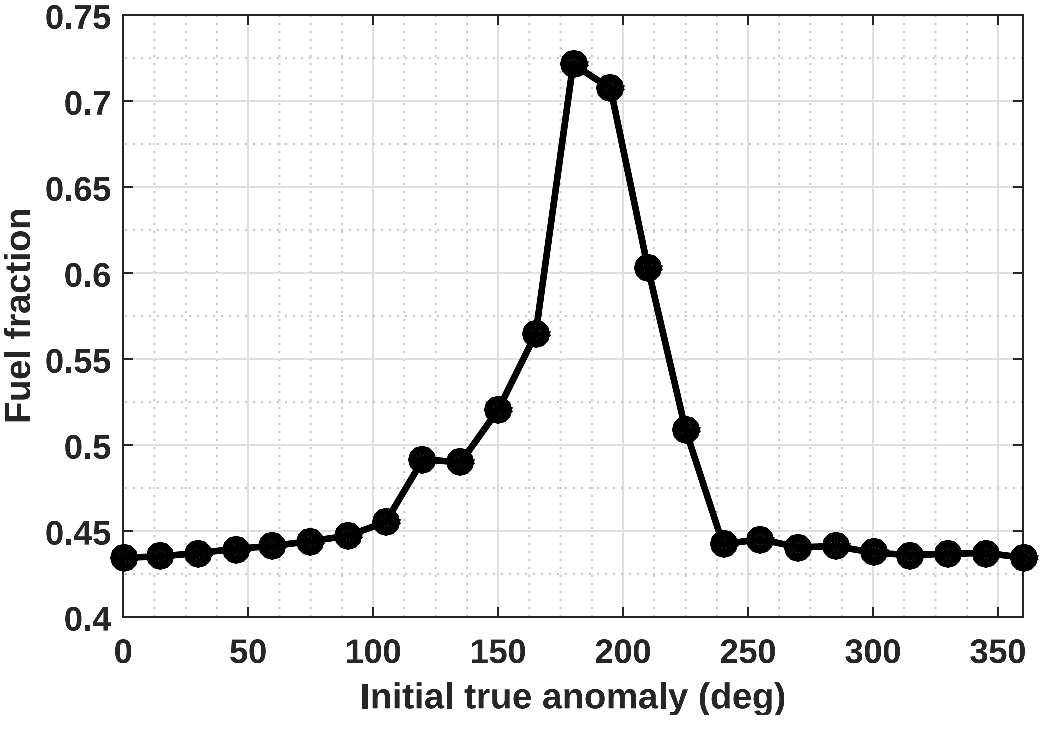

Fig. 4.13 Fuel fraction variation with initial true anomaly in an ellipse to circle transfer.

In figure 4.13, it is visible that the maximum fuel expenditure occurs when the start location is the aphelion. Nonetheless, it is seen that in comparison to the time optimal case, as the transfer time is larger, the peak is of a lower magnitude than in figure 4.11. Unlike the time optimal case, for a wide range of starting true anomalies (±100° from the perihelion), it is seen that the fuel fraction remains relatively insensitive to the starting location. This is because the coast is able to adjust for the disadvantageous starting location.

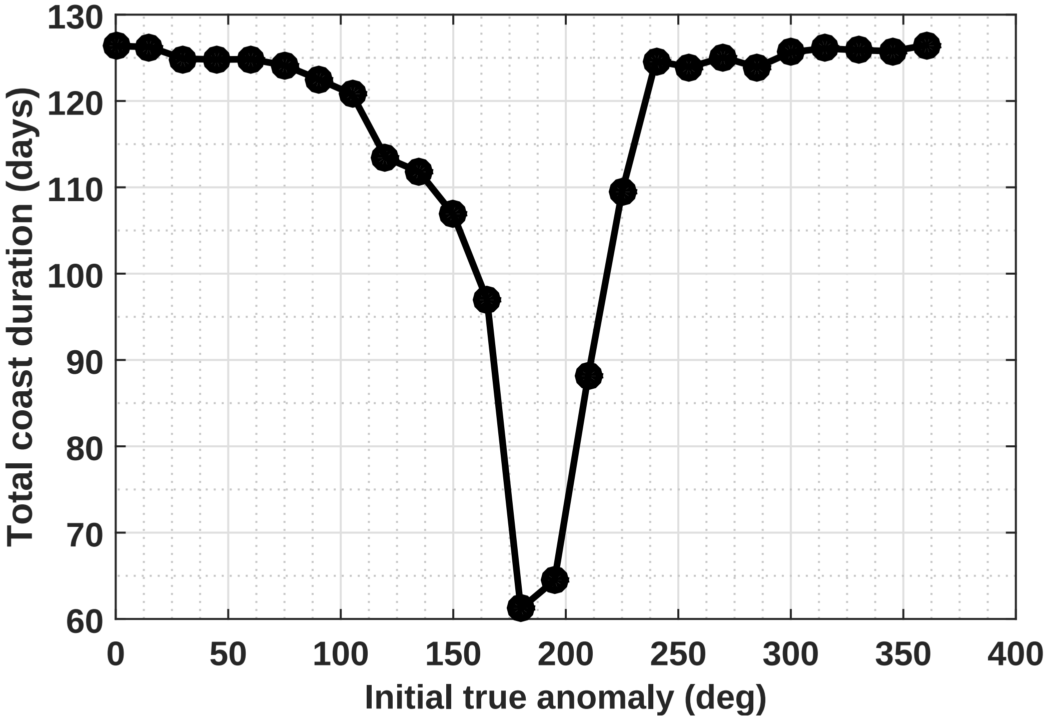

Fig. 4.14 Coast duration variation with initial true anomaly in an ellipse to circle transfer.

Figure 4.14 shows the variation of the coast duration. For the $\pm 100^\circ$ range about the perihelion, the coast is greater than or equal to 120 days. When the starting true anomaly is in the vicinity of the aphelion, the total coast duration sharply drops to less than half the maximum value attained. This is the reason for the increase of over 25% in propellant consumption compared to the minimum value.

4.4.2 Trajectory with multiple intermediate coasts

The following trajectory is the reason for the specification that the numerical method should be able to perform the trajectory optimization without any information a priori about the control structure. Depending on the flight duration, there may be multiple thrust-coast-thrust switchings that cannot be determined beforehand. Figure 4.15 shows the same for an ellipse-ellipse transfer from a 0.4AU perihelion orbit with eccentricity of 0.5 to a 1.524AU orbit with eccentricity of 0.1. The angle between the line of apsides is 225°.

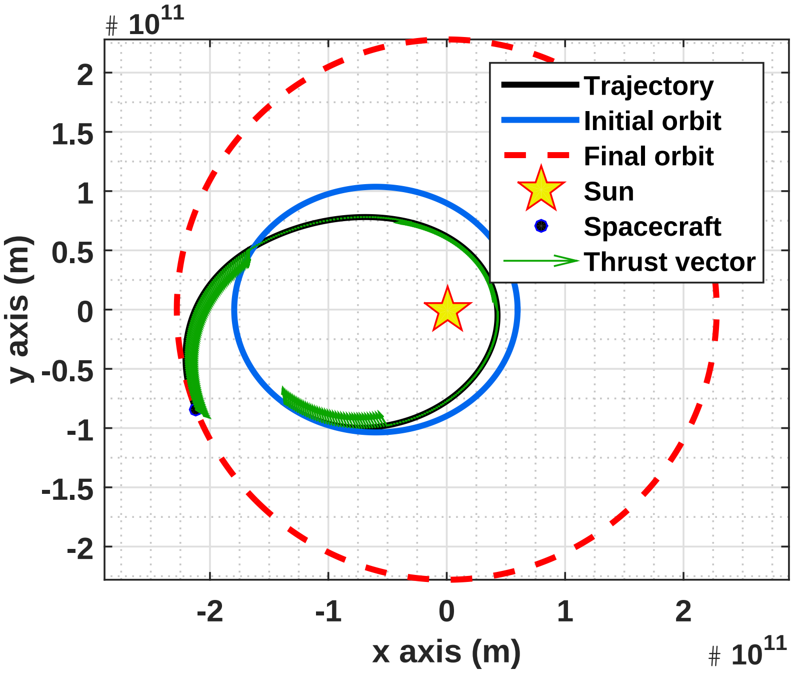

Fig. 4.15 Sample trajectory with multiple intermediate coasts.

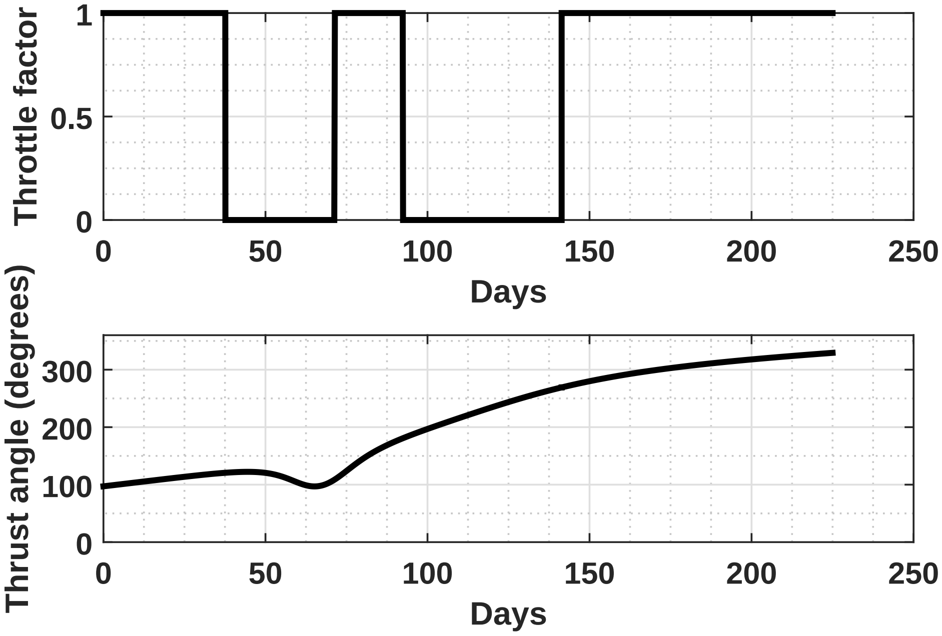

Fig. 4.16 Control profile for the trajectory with multiple intermediate coasts.

Figure 4.16 shows the control profile. Two coast phases are clearly visible. The first and last thrust phases have inward radial components. The second thrust phase is mostly tangential. The first thrust phase also has a small retrograde component that leads to the lowering of the perihelion. This is an artifact of fixing the transfer duration to 225 days. Increasing the flight duration will alleviate this perihelion lowering which is a symptom of energy wastage.

4.5 Three dimensional transfers

4.5.1 Sample 3D transfer

To demonstrate the ability of the code, a 350 day fuel optimal NEP transfer is considered from a 1AU circular orbit with 0° inclination to a 0.5AU circular orbit inclined at 90° to the initial orbit. This type of trajectories could be useful for closely observing the solar poles without having to resort to inclination change techniques that rely on gravity assists from Jupiter.

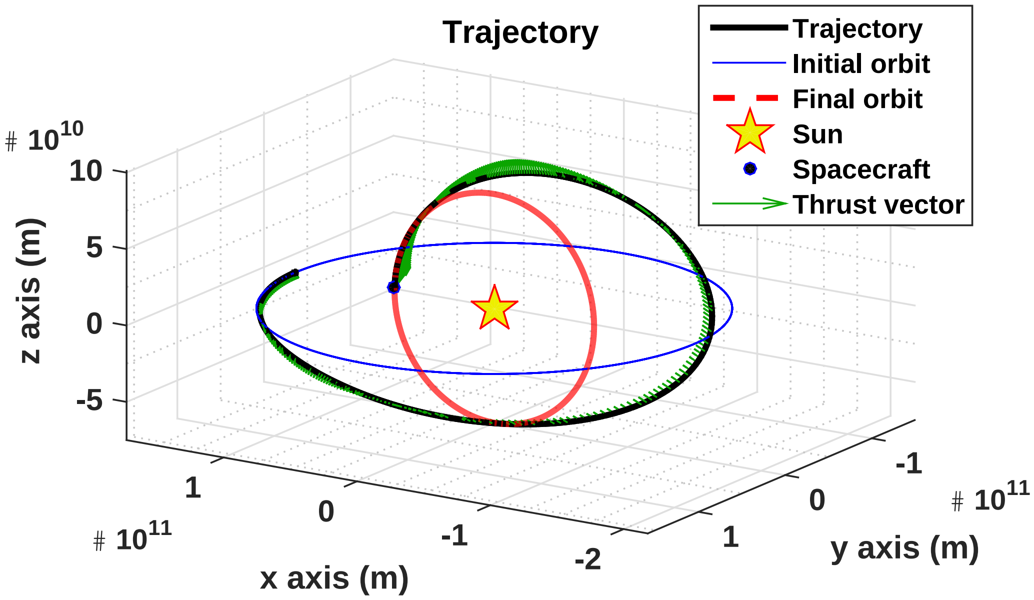

Fig. 4.17 Sample 3D heliocentric trajectory.

As seen in figure 4.17, the distance from the sun first increases and then it gets lowered to the final value.

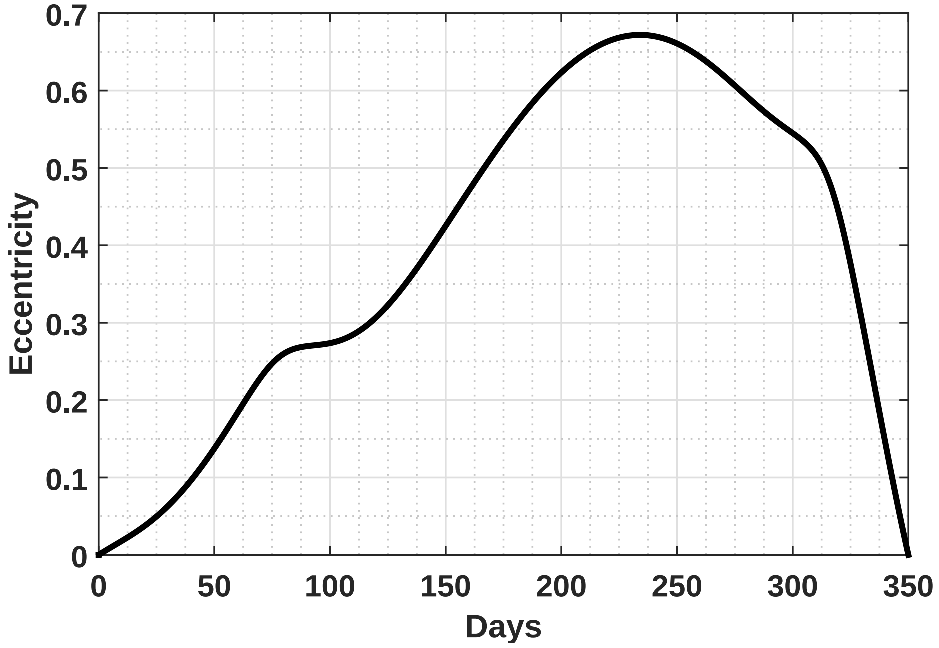

Fig. 4.18 Instantaneous eccentricity profile.

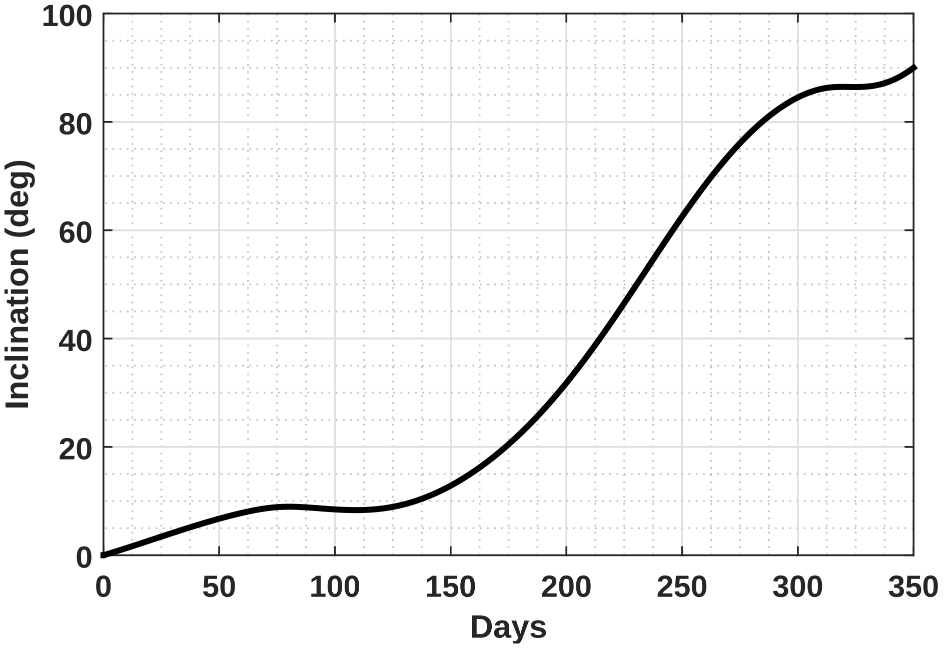

Fig. 4.19 Instantaneous inclination profile.

Figures 4.18 and 4.19 show the instantaneous eccentricity and inclination profiles for the sample transfer. When comparing with the trajectory plot, it is seen that the bulk of the inclination change occurs when the spacecraft is farthest from the sun. This is in accordance to conventional understanding as the ΔV requirements for inclination change is lowest when the spacecraft's velocity is a minimum. The final circularizing of the orbit occurs in the last phase of the trajectory when the spacecraft is very close to the final orbit. This is evident from the sharp drop in the eccentricity of the trajectory. The inclination only shows a minor change towards the target value in this time period.

4.5.2 Parametric studies on 3D transfers

Three dimensional transfers include many variables, whose influence is difficult to qualitatively understand. For this purpose, the effect of inclination change on transfers between a 1AU to a 1.5AU circular orbit is studied in depth in order to obtain some understanding on the nature of such low thrust transfers. (Initial acceleration is taken to be $1mm/s^2$ with 2000s I_{sp})

With varying inclination, starting from nodal line

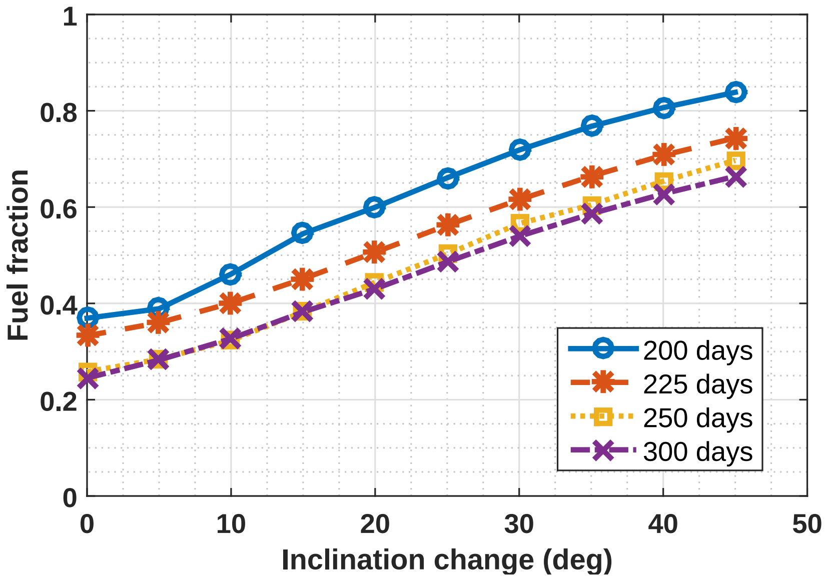

Fig. 4.20 Fuel fraction with varying inclinations and flight durations.

Here a spacecraft transfers between the aforementioned orbits with varying inclinations and flight durations in the fuel optimal framework. The starting point is fixed on the line of intersection of the two orbital planes in the ascending side. Figure 4.20 shows the effect of both varying inclination change and the flight duration. It is clearly visible that higher inclinations lead to much greater propellant consumption. Increasing flight duration tends to reduce the propellant consumption but there is a lower bound as is evident from the figure. This means that increasing the flight duration will offer diminishing returns in terms of propellant requirements. These type of plots will enable designers to perform trade studies to analyze the best combination of propellant requirement and flight duration.

Transfer between fixed orbits starting from different true anomalies

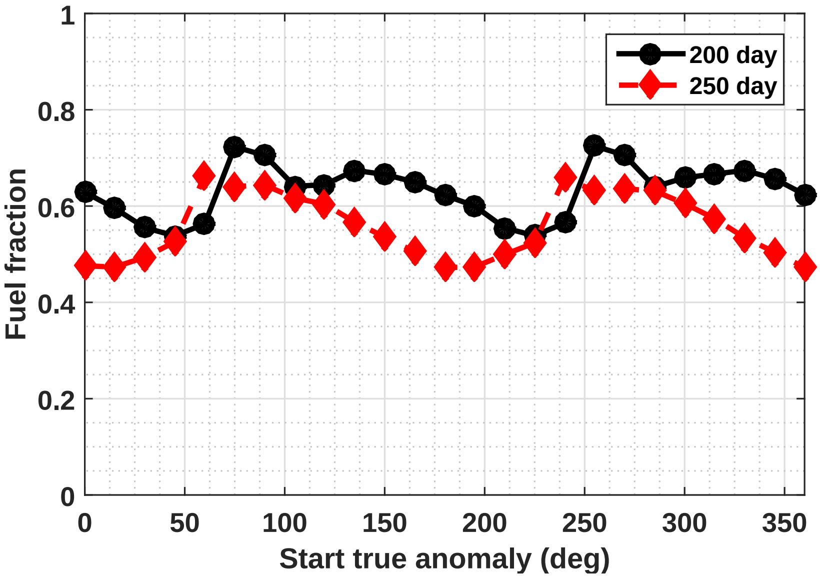

Fig. 4.21 Fuel fraction with varying start locations.

Figure 4.21 presents results for the same spacecraft transferring from 1AU to 1.5AU with 22.5° inclination change for a 200 day transfer. 0° corresponds to a point on the line of intersection of the two circular orbital planes. There is roughly, a 20% swing in fuel fraction needed depending on the starting location. In the minimum case, the majority of the inclination change is performed towards the final phase of the trajectory. This corresponds to an inclination change being performed in the vicinity of the line of intersection of the orbital planes. The maximum case corresponds to the inclination change being performed early. This corresponds to the conventional knowledge from impulsive transfers that a combined maneuver at the line of intersections of orbital planes farthest from the gravitating body leads to minimum ΔV requirements. The same seems to hold true in the case of low thrust maneuvers although it is impossible to comment about the exact nature of the maneuver and quantify it a priori to the trajectory optimization run. Due to the circular nature of the initial and final orbits, the trends in figure 4.21 show a 180° periodicity. The trajectories in the ascending and descending sides are identical all aspects except for the out of plane motion component which is inverted in sign. This type of periodicity is lost when the transfers happen between elliptic orbits or even if one of the orbits is elliptic. Even though there may be symmetry in the geometrical orientation, the kinetic energy of the spacecraft is vastly different between the periapsis and apoapsis sides of the elliptic orbit. This leads to only a 360° periodicity in the more general case.

Issue with the solution

It is also visible that for some starting true anomalies, the (example - at 60° and at 240°) the 250 day transfer requires more propellant than the 200 day transfer. This is due to the non uniqueness of the solution. In the worst case, the solution that should have been found for the 250 day transfer at these points is actually a 200 day transfer followed by a coast once the final orbit is attained. In reality, these types of transfers are extremely difficult to obtain numerically. Thus for some cases, it is necessary to conduct extensive numerical experiments to determine the true nature of the solution. This occurs because the Pontryagin's minimum principle is only a necessary condition for optimality and does not guarantee uniqueness of the obtained optimal trajectories. This example serves to highlight the drawbacks of the solution procedure. Namely, fuel optimality is not always guaranteed and the user must perform exhaustive analysis in case mission constraints are being violated.
The other alternative is to perform a wide range of numerical experiments and take the lower envelop of the resulting fuel fraction curves with their matching flight durations.

Method to resolve the issue in the current framework

In figure 4.21, all the trajectories obtained have a thrust-coast-thrust control structure. There is only one coast duration in the middle phase of the trajectory. This is the result of rather wide boundss on the costate variables corresponding to the position. By tightening the bounds, a significantly better solution can be obtained.
Figure 4.22 presents the results of the repeated analysis with tighter bounds on the costates. The starting locations which previously led to higher propellant consumption for the 250 day case now lead to a net lower propellant consumption. The control structure for these trajectories is radically different different with a thrust-coast-thrust-coast-thrust structure. There are two intermediate coasts with one intermediate thrust phase. The inclination change is now performed at a location with better efficiency (i.e at the line of intersection of the orbital planes).

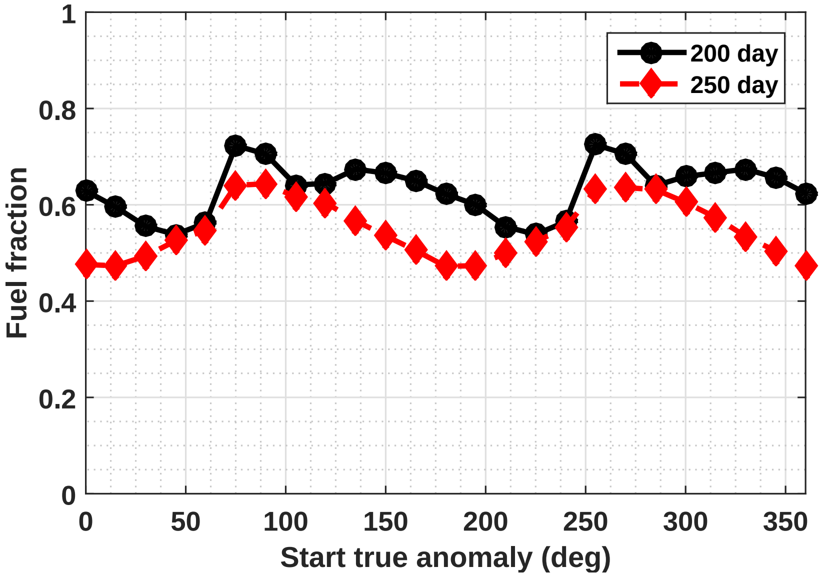

Fig. 4.22 Fuel fraction with varying start locations (tighter costate bounds).

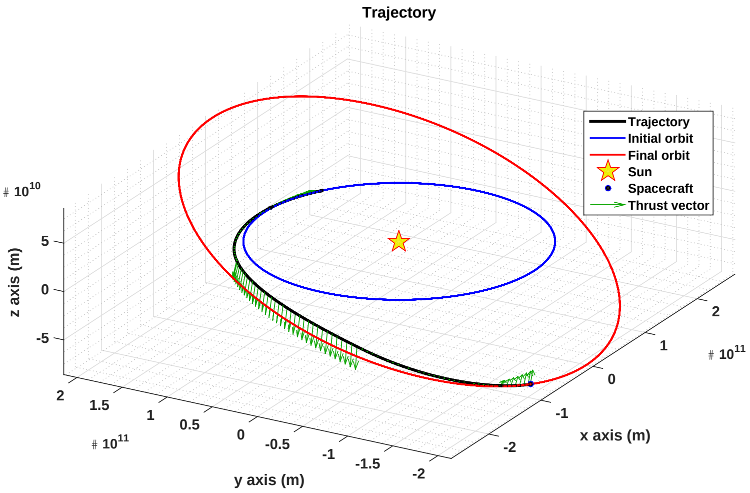

Fig. 4.23 A 250 day trajectory starting at 60° with tighter costate bounds.

The other starting true anomaly locations lead to the same trajectory with identical control structures and fuel consumption. This leads to the following strategy for the application of differential evolution to fuel optimal transfers. If in the case of a larger flight duration, worse performing solutions are found, the bounds on the costate variables are to be progressively tightened until a better performing solution is found. In case no better solutions are found, it can be concluded (but not proven) that the best solution is the one with the lower flight duration followed by a terminal coast. It is seen from figure 4.23 that the initial and final thrust phases operate mostly in plane maneuvers to change the semi-major axis. The intermediate thrust phase in the vicinity of the line of intersection of the orbital planes is seen to cause most of the inclination change. This observation is supported by figure 4.24.

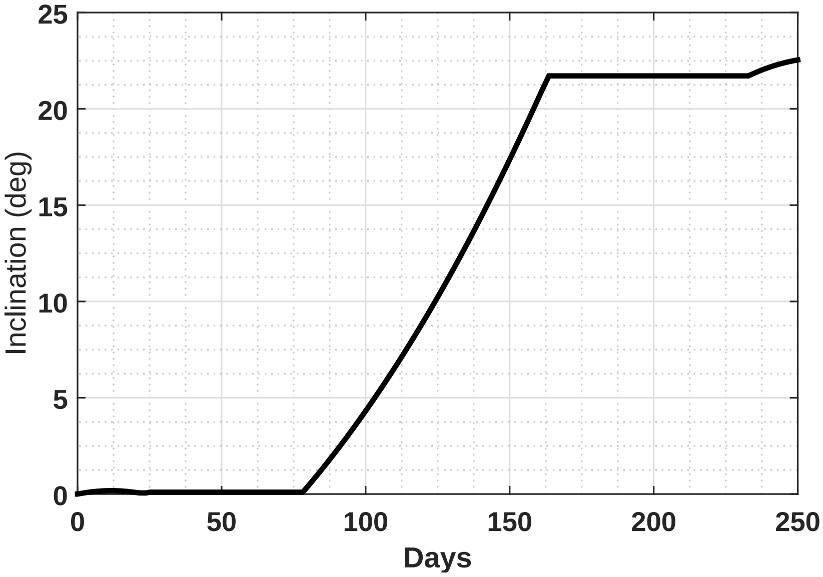

Fig. 4.24 Inclination profile with tighter costate bounds.

Here it is seen that about 21.6° of inclination change is performed by the intermediate burn. The initial and final burns lead to very small inclination changes. The coasts are visible as the two flat portions of the graph where the inclination stays constant. This is due to Keplerian dynamics which causes the angular momentum vector to be conserved under the absence of thrust forces.

Chapter 5

Geocentric Transfer Results

5.1 Introduction to GTO-GSO transfers

Geosynchronous transfer orbits are highly elliptical orbits that spacecrafts are placed into by launch vehicle upper stages. Geosynchronous orbits are a class of high altitude circular orbits whose orbital time period is equal to the rotational period of the Earth. These are important for communication satellites which are to appear in fixed locations over the ground when in operation. Launch vehicle upper stages usually deploy the satellite into a GTO from which the final GSO is achieved by means of the spacecraft's propulsion system. These transfers are important for the deployment of communication satellites. Conventional high thrust satellites perform a series of orbit raising maneuvers combined with plane change maneuvers to enter into a 24 hour equatorial orbit. Low thrust satellites on the other hand, need to thrust for several months to be able to raise themselves to their required location. Optimizing these transfers can help in saving propellant mass and thus increasing the operational life of the satellites. Low thrust spacecraft propulsion systems on account of their higher specific impulse can perform this GTO-GSO transfer with much lower fuel fractions than conventional chemically propelled satellites. The added advantage of these low thrust, high specific impulse satellites is that transfers with large inclination changes can be performed with much lesser propellant than chemically propelled spacecrafts. This implies that launches from higher latitudes which were once deemed impossible due to orbit inclination requirements can now be made feasible. Overall system plus launch costs may decrease due to the lower propellant mass and the availability of a greater number of launch sites to conduct the mission.

5.2 Sample GTO-GSO transfer

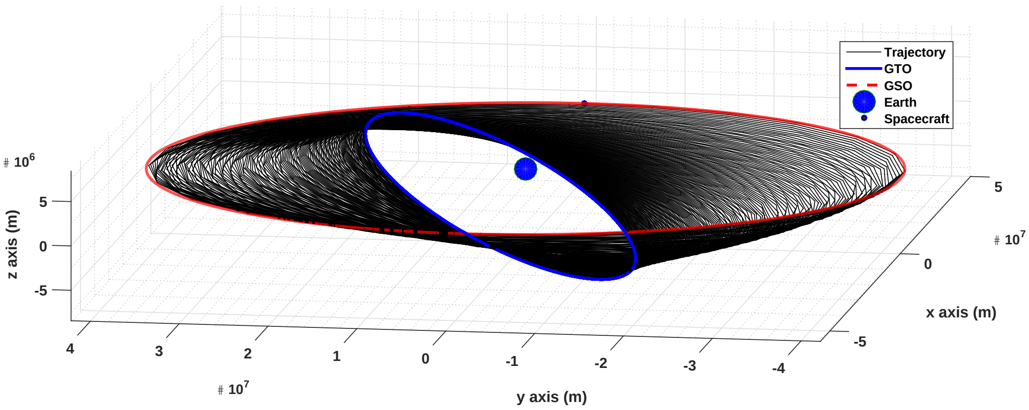

Fig. 5.1 A sample GTO to GSO transfer with 28.5° inclination change.

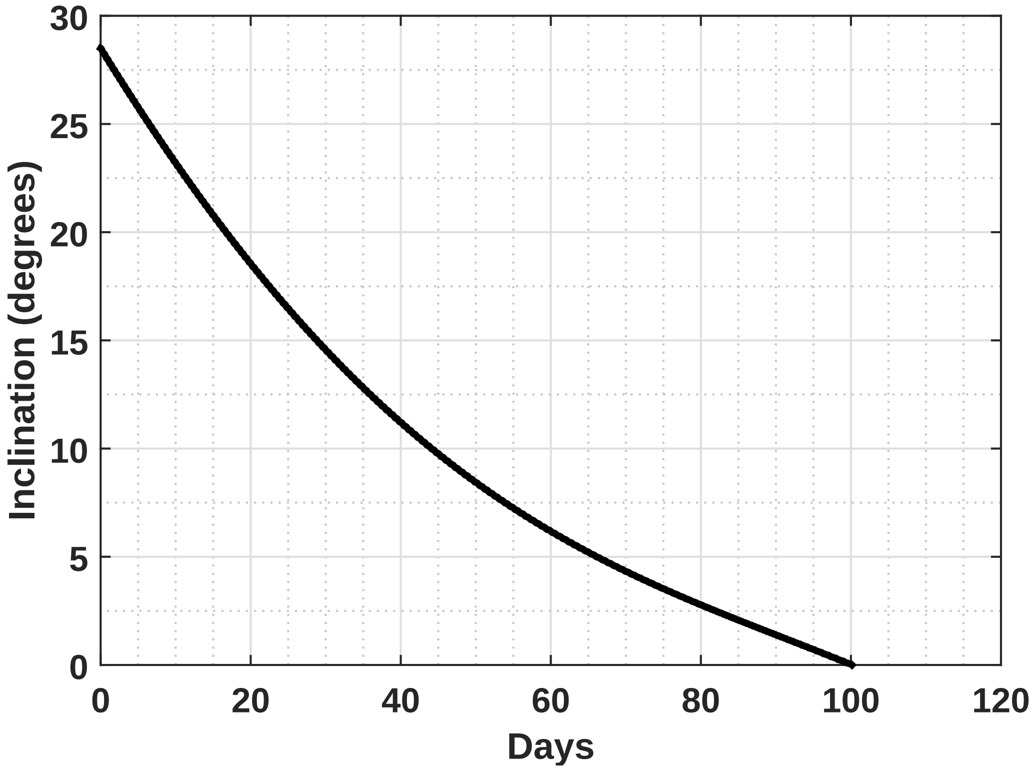

Fig. 5.2 Inclination change performed by the spacecraft launched into a GTO from the Kennedy Space Center.

Here, a spacecraft of 1000kg initial mass is transferred from a 250km×35768km orbit with an inclination of 28.5 degrees to an equatorial geosynchronous orbit. The thrust level is 300mN and has an I_{sp} of 2000s. This thrust level is realizable with technology as of today.

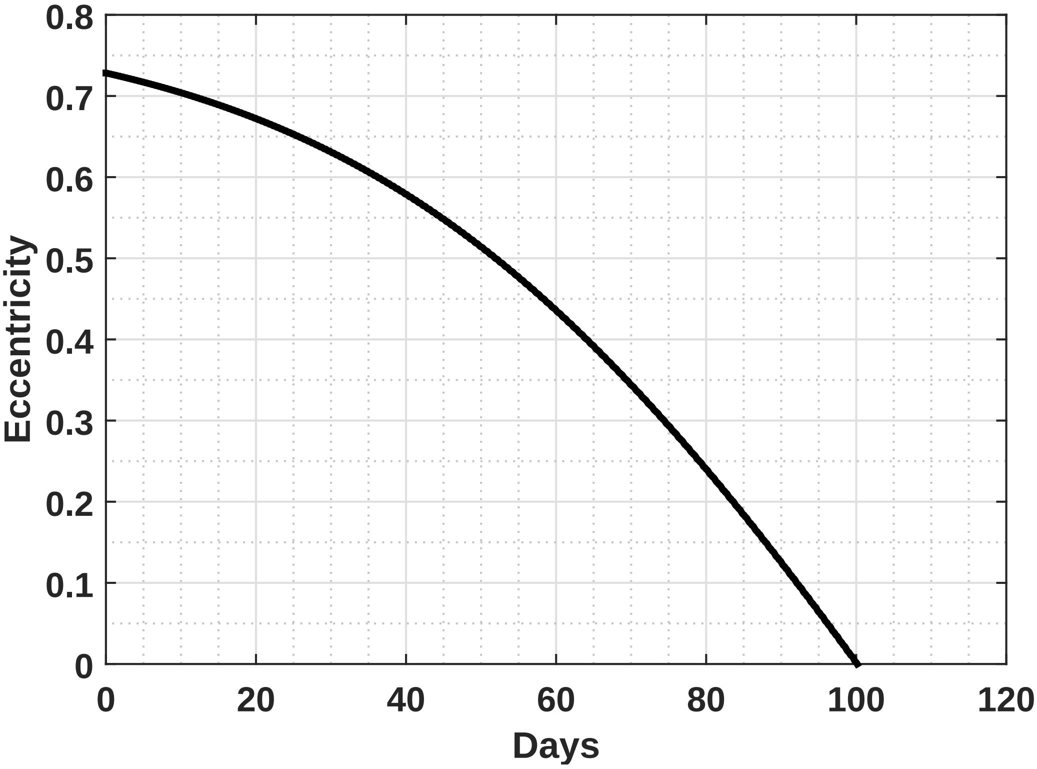

Fig. 5.3 Instantaneous eccentricity profile of the spacecraft's orbit.

From figure 5.1, it is evident that the spacecraft performs multiple spirals around the Earth. The inclination change is also gradually performed. The propellant mass needed for this transfer is only 132.342kg. A single impulse combined maneuver at the apogee with the state of the art hypergolic bipropellant chemical propulsion systems would require approximately 480kg of chemical propellants. This clearly highlights the effectiveness in terms of mass fraction that electric propulsion systems can achieve. The disadvantage is that the transfer takes approximately 99.7 days to complete. This can imply that the spacecraft would have to pass through the van Allen radiation belt several times and that would necessitate appropriate radiation hardening of electronic components. There is also the problem of eclipses where solar power would not be available. It is possible with current battery technology to provide power during the eclipses but it may be preferable to stop thrusting during eclipses. The current mathematical model for optimal control is easily capable of handling such discontinuities by just setting the maximum available thrust level to zero.

Figure 5.2 depicts the inclination profile of the spacecraft. Due to the constant low thrust, the inclination does not change abruptly but is smoothly driven down to zero. Similar trends are seen with the eccentricity profile in figure 5.3. The final GSO is assumed to be circular and equatorial. It is also possible that instead of a conventional launch, a supersynchronous orbit can be made use of. This is due to the fact that the spacecraft initially raises the apogee by a small fraction before lowering it to GSO levels. This is indicative of wasted energy and instead of using higher amounts of electric propellant, it may be possible to reduce the launch mass of the spacecraft and instead enable the launch vehicle to lob the spacecraft into a higher orbit than the GTO.

5.3 Parametric studies on GTO-GSO transfers

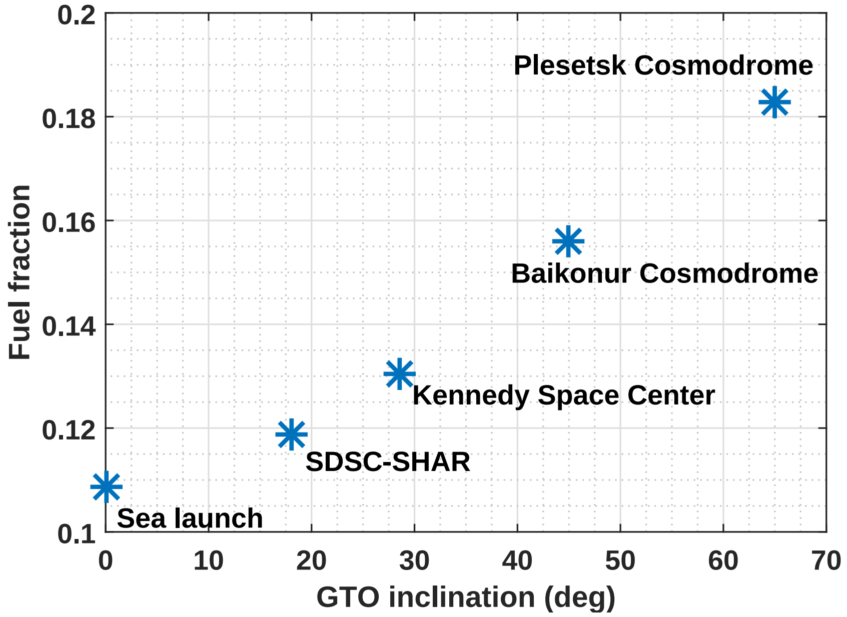

Fig. 5.4 Fuel fraction dependency on launch site latitude.

From figure 5.4, it can be seen that the launch site latitude has a clear implication on the propellant fraction needed to perform the GTO to GSO transfer. Higher latitudes require much larger fuel fuel fraction but even for the Plesetsk Cosmodrome, the fuel fraction needed with continuous thrusting is less than 20%. This means that launchers from the Russian mainland may be used to economically launch commercial satellites equipped with electric thrusters into equatorial GSO orbits. This decision may be more economical depending on the total cost of the launch vehicle and the spacecraft.

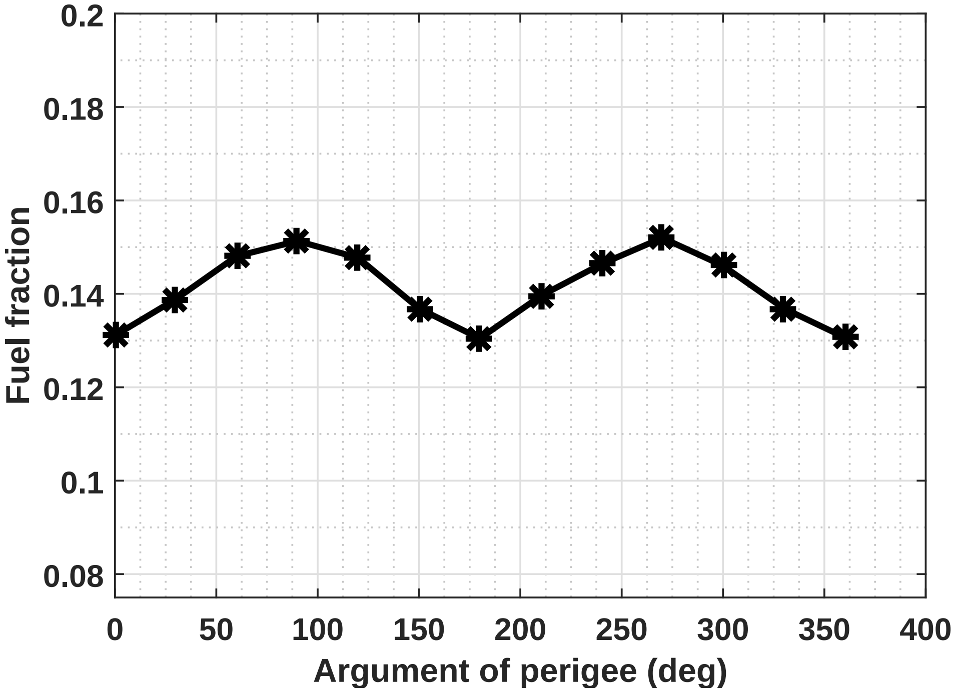

Fig. 5.5 Fuel fraction dependency on GTO argument of perigee.

In figure 5.5, it is visible that the argument of perigee (ω) influences the propellant amount required by a small degree. The GTO corresponds to a launch from the Kennedy Space Center. The minimum is seen to occur when the apogee of the GTO is tangent to the final GSO. This is the case when ω is 0°, 180° or 360°. The maximum fuel requirement occurs when ω is 90°. The difference in propellant fraction needed is in the order of 2%. This is a very minor change considering the large change in orbital orientation. In the case of high thrust chemical propulsion systems, such large changes in orbital orientation are not tolerable as the ΔV requirement rapidly shoots up when the apogee of the GTO does not lie on the final GSO. This insensitivity to large changes in the initial orbital plane orientation suggest that in case of launch vehicle issues, the success of the mission as a whole will not be jeopardized. Large inclination changes also do not present a major hurdle as the higher I_{sp} tends to reduce the propellant requirement to levels far below what would be required by chemical propulsion systems. As an additional example, a GTO-GSO transfer by a 1000kg spacecraft launched from the Plesetsk Cosmodrome would require about 617kg of propellant if a combined maneuver is performed at the apogee. This is in stark contrast to the 183kg required from the same orbit with electric propulsion systems. In this case, the transfer time is approximately 138.4 days.

5.4 Fuel optimal GTO-GSO transfers

These transfers are achieved by fixing a flight duration above the time optimal value. These can lead to several thrust coast phases which ultimately lead to an improvement in the fuel fraction needed for the maneuver. These transfers are also extremely numerically challenging due to the large number of switchings in the control structure. The current code on an 8 core machine takes tens of minutes to perform an optimization run for a 75 day GTO-GSO transfer for a 1000kg spacecraft with 500mN of thrust at 2000s I_{sp} with the GTO delivered by a launch from the Kennedy Space Center.

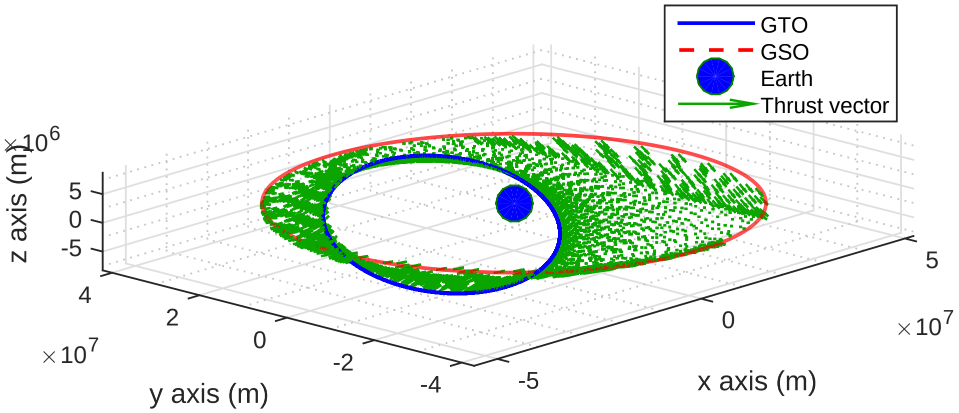

Fig. 5.6 Thrust vector plot in space.

Figure 5.6 shows a plot of the thrust vectors at locations where the thruster is firing. It is seen that a significant portion of the orbit does not have any thrusting. Thrusting is seen mainly in the vicinity of the apogee while for a large duration of time, the perigee remains in the coast period. Towards the final phase of the orbit, the perigee side sees retrograde thrusting. This is performed to ensure complete circularizing of the final GSO orbit as the apogee gets boosted to a higher level due to the thrust arcs.

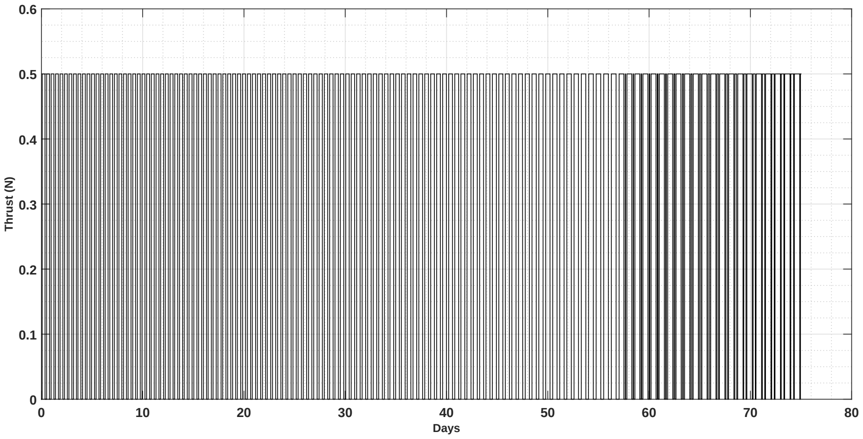

Fig. 5.7 Thrust vector profile.

Figure 5.7 is a plot of the thrust magnitude as a function of time. The density of lines in the figure depicts the frequency of control switching.

5.4.1 Impact of flight duration on fuel optimal GTO-GSO transfers

In fuel optimal transfers, the flight duration is fixed to a value greater than or equal to the time optimal value. When equal, the fuel and time optimal solutions coincide. When the flight duration is set to a higher value, the transfer consumes lesser propellant due to periods of coasting that get introduced automatically by the indirect optimal control formulation.

Table 5.1 GTO-GSO fuel fraction comparison with varying flight duration for 500mN thrust.

Formulation	Flight duration (days)	Fuel fraction
Time optimal	59.987	0.13214
Fuel optimal	67.500	0.11600
Fuel optimal	70.000	0.11355
Fuel optimal	75.000	0.10832
Fuel optimal	80.000	0.10716
Fuel optimal	85.000	0.10371
Fuel optimal	90.000	0.10264

Table 5.2 GTO-GSO fuel fraction comparison with varying flight duration for 300mN thrust.

Formulation	Flight duration (days)	Fuel fraction
Time optimal	099.178	0.13108
Fuel optimal	112.500	0.11862
Fuel optimal	125.000	0.10971
Fuel optimal	137.500	0.10500

Tables 5.1 and 5.2 list data for varying flight duration on the fuel fraction needed for the transfer. It is seen that even a modest increase in flight duration can lead to savings in propellant. This is due to the increased orbital maneuver efficiency of thrusting in the vicinity of the perigee. The initial GTO is assumed to be delivered by a launch from the Kennedy Space Center. The argument of perigee of the GTO is taken to be 0°. The initial spacecraft mass is 1000kg and the thruster I_{sp} is 2000s. Table 5.2 represents values achievable by current technology using Hall effect thrusters and large solar panels.

Gopinath (2003) utilizes a strategy to minimize fuel consumption by introducing arcs of thrusting and coasting by defining a thrust arc length from the center of the Earth on the side of the apogee of the GTO. This approach ideally should give the time optimal result when the thrust arc length is a full 360°. However, upon applying the current optimal control methodology, it is found that significantly better solutions can be obtained in comparison to the strategy outlined in the paper. Fuel optimal transfers having higher flight durations than the time optimal result lead to better performing transfers than the ones in the aforementioned paper.

5.5 Solar gravitational effects on GTO-GSO transfers

Table 5.3 Solar gravity influence on GTO-GSO fuel fraction with varying departure epoch for 500mN thrust.

Start epoch (JD)	Earth alone	Sun in state dynamics alone	Sun in state and costate dynamics
2458287.000	0.13214	0.13711	0.13197
2458378.313	0.13214	0.13455	0.13186
2458469.625	0.13214	0.13749	0.13312
2458560.938	0.13214	0.13457	0.13220
2458652.250	0.13214	0.13708	0.13129

Table 5.3 presents results for the influence of solar perturbations on the spacecraft transferring from a GTO launched from Kennedy Space Center. The results are tabulated for every 3 months over the course of one year. It is seen that the effect of the Sun is significant and in some cases leads to extra propellant consumption while in some cases lead to a slight benefit. All these are dependent on the relative orbital plane orientations, argument of perigee at launch and the start epoch. This introduces difficulties in qualitatively describing the effects of the sun. The quantitative variations are less than 0.5% for all departure epochs when the Sun's effect is considered in both the state and costate dynamics. Adding the Sun's gravitational perturbation to the state dynamics while keeping the costate dynamics unchanged leads to significantly worse solutions. In all cases, this formulation gives worse results than the complete optimal control formulation. This suggests that solar perturbations if considered, have to be included in both the state and costate dynamics to obtain reliable solutions.

5.6 Lunar gravitational effects on GTO-GSO transfers

Table 5.4 Lunar gravity influence on GTO-GSO fuel fraction with varying departure epoch for 500mN thrust.

Start epoch (JD)	Earth alone	Earth+Moon
2458287.000	0.13214	0.13182
2458378.313	0.13214	0.13174
2458469.625	0.13214	0.13081
2458560.938	0.13214	0.13200
2458652.250	0.13214	0.13158

In table 5.4, it is seen that for the minimum time formulation for the same orbit transfer as in the previous section, it is visible that the inclusion of Moon's gravity has provided a slight assistance to the transfer. This depends on a variety of other factors including the initial orbit Ω and ω and flight duration. Due to the large number of influencing parameters, only the start epoch has been varied for the demonstration problem as in the previous sections. It is possible that for an certain orbital and transfer parameters, lunar gravity could be of a slight detriment for GTO-GSO transfers.

5.7 Comparison with literature

The current DE based indirect optimal control technique has been applied to a GTO-GSO transfer and obtained results have been compared with values from literature. It has been found that in comparison to collocation methods as used by Falck and Dankanich (2012). Falck et al. (2014) compare different guidance laws for the same problem. Betts (2000) has applied the direct collocation method to solve the same problem using sequential quadratic programming. Due to the large number of revolutions, direct solutions by direct methods are not feasible. This prompted Falck and Dankanich (2012) to make use of orbital averaging techniques over the state and costates to reduce the computational time. It has been found that the current method is capable outperforming the ones quoted by the above references. The problem considered is the transfer of a 1200kg spacecraft from GTO of $185.6616km \times 35786.3384km$ altitude. The power available is 5kW with I_{sp} of 1800s. The GTO argument of perigee is 0.1° and the right ascension of the ascending node is 179.6°. The GTO is assumed to be the result of a launch from the Kennedy Space Center with an inclination of 28.5 degrees.

Table 5.5 Comparison of obtained GTO-GSO results with literature.

Solution technique	Flight duration (days)	Fuel fraction
Current method	114.88	0.14601
Collocation	118.29	0.15035
Kluever control parametrization	118.36	0.15044
SEPSPOT	118.29	0.15035
DAG	125.60	0.15636
Q-Law	120.02	0.14966

Table 5.5 presents the comparison of results for a GTO-GSO transfer using the various methods for the given spacecraft parameters. The control parametrization method by Kluever can be found in the book on spacecraft trajectory optimization by Conway (2014). It is seen to give comparable results with SEPSPOT (solar electric propulsion code for low thrust missions) and the collocation method by Falck and Dankanich (2012). The Q-Law guidance strategy presented by Falck et al. (2014) has provided better results than the direct optimal control methods in the table. The current method is seen to give a substantially better performance with a 3.41 day improvement in the flight duration compared to the collocation method. The corresponding propellant savings is 5.208 kilograms. Direct methods have the added disadvantage of being very cumbersome to use in a fuel optimal framework for a

GTO-GSO transfer as seen in a previous section of this chapter due to the extremely large number of jumps in the control structure. These jumps are not known a priori. It is also seen that there are thrusting regions in the apogee of the orbit in the fuel optimal formulation. This is unexpected and can result in poor initial guesses for the control structure. The use of orbital averaging also reduces the accuracy of the direct approach. Betts (2000) reported computational time of several hours for a 16000 point discretized GTO-GSO transfer. This is due to the huge size of the NLP problem that results from the direct approach to optimal control. Using the current methodology, accurate fuel optimal solutions are obtained in a matter of minutes for the current problem under consideration for flight durations that are fixed to values greater than the time optimal solution. Significant improvements in fuel fraction can be obtained by increasing the flight duration.

Chapter 6

Transfers with multiple gravitating bodies

6.1 Introduction

This chapter addresses the main problem of this study. A spacecraft in a parking orbit around one planet is transferred to a parking orbit around another planet. This transfer must be performed in an optimal fashion in order to minimize propellant expenditure of the flight duration. This problem poses various challenges including that of numerical sensitivity in the planetocentric phases. If only the heliocentric dynamics is used, the resulting numerical errors will be excessive as the planetocentric orbit phase involves small deviations from the planet's distance from the Sun. This brings about the need to switch between frames of reference from heliocentric to planetocentric and vice versa. It is essential that there is continuity in all the state vector components at all frame switching points else impulsive maneuvers will be necessary. To eliminate this, the following theoretical results are applied.

6.1.1 Frame switching with optimal control

Performing a frame switch amounts to changing the system dynamics and state vector at a particular instant of time. This makes it essential to determine how the costates transform when the state vector undergoes a coordinate transformation. The equation for transformation of the costate vector can be found in the book by Arthur. E and Ho (1975).

$$\vec{\lambda}(t^+) = -[\Psi_{x_t^+}]^T [\Psi_{x_t^-}]^{-T} \vec{\lambda}(t^-) \tag{6.1}$$

Here $[\Psi_x]$ represents the Jacobian of the set of transformation laws for the state vector. t^+ represents the time instant just after the transformation and t^- represents the time instant just after. In the Cartesian coordinate system, the transformation between heliocentric and planetocentric dynamics is given by equations 6.2 to 6.8.

6.1.2 Frame switching in the context of the current problem

$$x_p = x_s - X_p \tag{6.2}$$

$$y_p = y_s - Y_p \tag{6.3}$$

$$y_p = y_s - Y_p \tag{6.4}$$

$$\dot{x}_p = \dot{x}_s - \dot{X}_p \tag{6.5}$$

$$\dot{y}_p = \dot{y}_s - \dot{Y}_p \tag{6.6}$$

$$\dot{z}_p = \dot{z}_s - \dot{Z}_p \tag{6.7}$$

$$m_p = m_s \tag{6.8}$$

Here X_p, Y_p, Z_p, $\dot{X}_p$, $\dot{Y}_p$ and $\dot{Z}_p$ are the heliocentric positions and velocities of the planet as functions of time alone. In this project, ephemer Corresponding to these, the Jacobian matrices are $\mathcal{I}_7$ and $-\mathcal{I}_7$ where $\mathcal{I}_7$ is the 7×7 identity matrix. Thus using equation 6.1, it is possible to derive that the costate variable are continuous and suffer no jumps under this coordinate transformation in the Cartesian coordinate system.

$$\vec{\lambda}(t^+) = \vec{\lambda}(t^-) \tag{6.9}$$

6.2 Earth-Moon transfers

The problem of transferring a spacecraft from an EPO to a low lunar orbit using electric propulsion systems is investigated here. Kluever and Pierson (1997) uses the indirect approach to optimal control coupled with SQP in a three stage optimization process to determine optimal Earth-Moon trajectories using electric propulsion. This approach splits the trajectory optimization into multiple phases which can lead to sub-optimality. Betts and Erb (2003) presents results using the direct transcription or the collocation method for solving the same problem in light of the ESA SMART-1 mission. The control structure is assumed to be a thrust-coast-thrust profile. Instead of multiple short burns at the perigee as done by SMART-1, it has been shown that a continuous long duration burn can lead to significantly improved flight durations for a small penalty in the fuel fraction. Mingotti et al. (2009) solves

the problem of a low thrust, low energy lunar transfer. The coupled restricted three body problem is used to provide an initial guess for the trajectory design. This is followed by direct transcription and multiple shooting to solve the low thrust, low energy transfer problem. This strategy has been shown to outperform several other impulsive transfers including that of the weak stability boundary approach.
Here, the same approach using differential evolution applied to indirect optimal control is used to solve the problem of transferring a spacecraft from an Earth parking orbit to a lunar orbit is solved. It is not necessary to make any assumptions about the control structure. The DE430 JPL ephemeris is used to obtain the lunar position and velocity with high accuracy. The formulation used can account for perturbing forces as well as eclipsing of the Sun with no changes in the optimal control law. For demonstration, an optimal transfer from an equatorial GSO to a 250km lunar orbit is performed.

6.2.1 Sample Earth-Moon transfer

Single step optimal Earth-Moon transfer results are presented below.

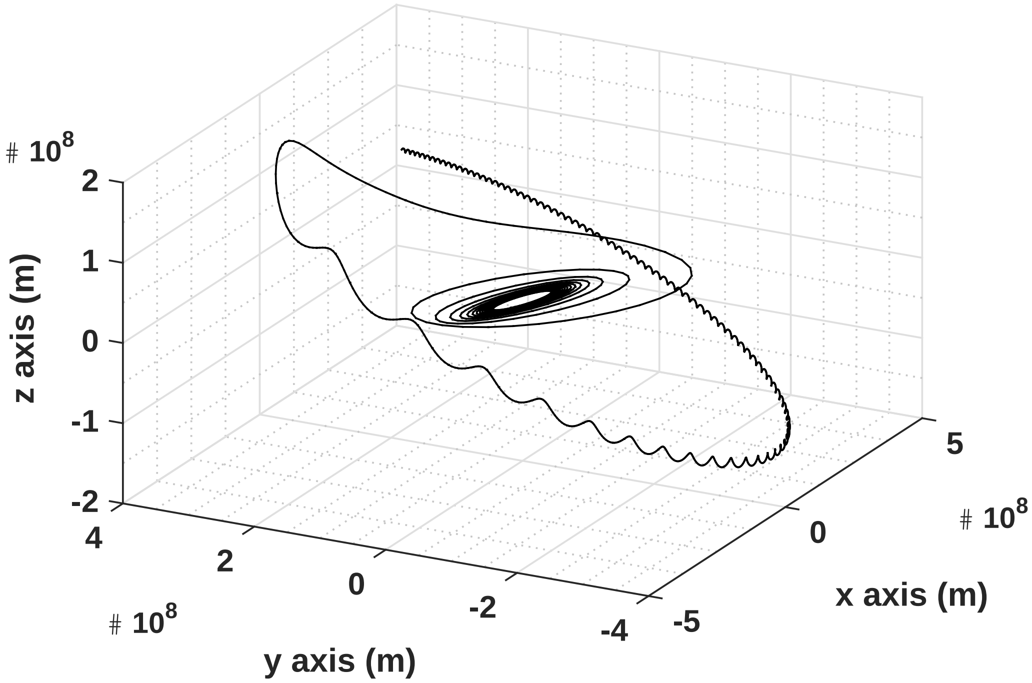

Fig. 6.1 Geocentric trajectory for sample transfer.

A transfer from a 42164km radius GSO inclined at 18° to the Earth's equator to a 250km circular orbit around the Moon inclined at 90° to the Earth's equator is considered. The thrust level is 500mN and the I_{sp} is 2000s. The initial mass of the spacecraft is 1000kg. Figure 6.1 shows the geocentric trajectory. Since the Earth equatorial frame is used, the z axis variation in the lunar trajectory is significant. This makes the problem inherently three dimensional. The trajectory is seen to spiral away from the GSO. The bulk of the inclination change is performed towards the final revolution around the Earth. When joining the Moon, the trajectory appears to be corkscrewing around the Moon with the altitude gradually lowered by the low thrust propulsion system. The total transfer time here is 75.80 days and the fuel fraction is 0.167. The departure epoch and the flight duration are set as optimization parameters and they are determined by the differential evolution algorithm. This causes the solution to converge to a time optimal value as the flight duration is left free with the thruster kept on all the time. It is also seen that the final revolution around the Earth is nearly equatorial. This transfer was specifically chosen to demonstrate the possibility of performing the transfer without having to choose a specific EPO.

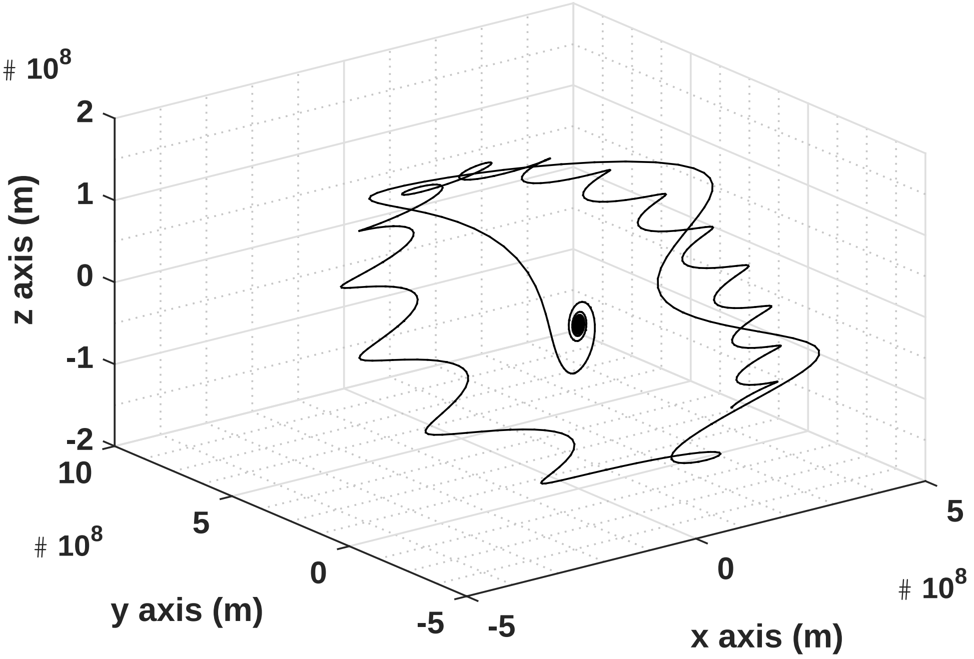

Fig. 6.2 Selenocentric trajectory for sample transfer.

From figure 6.2, it is seen that in the approach phase for the final selenocentric capture orbit, the bulk of the inclination change happens far away from the Moon. This is in accordance to conventional qualitative results for high thrust maneuvers. The circularization and altitude lowering phase is nearly planar.

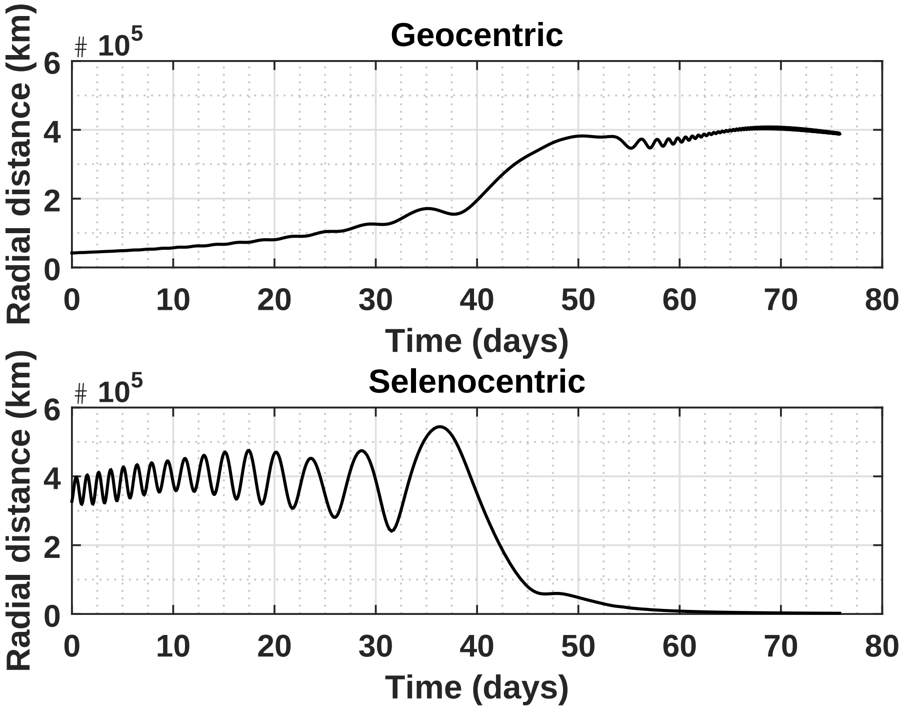

Fig. 6.3 Radial distance profile for sample transfer.

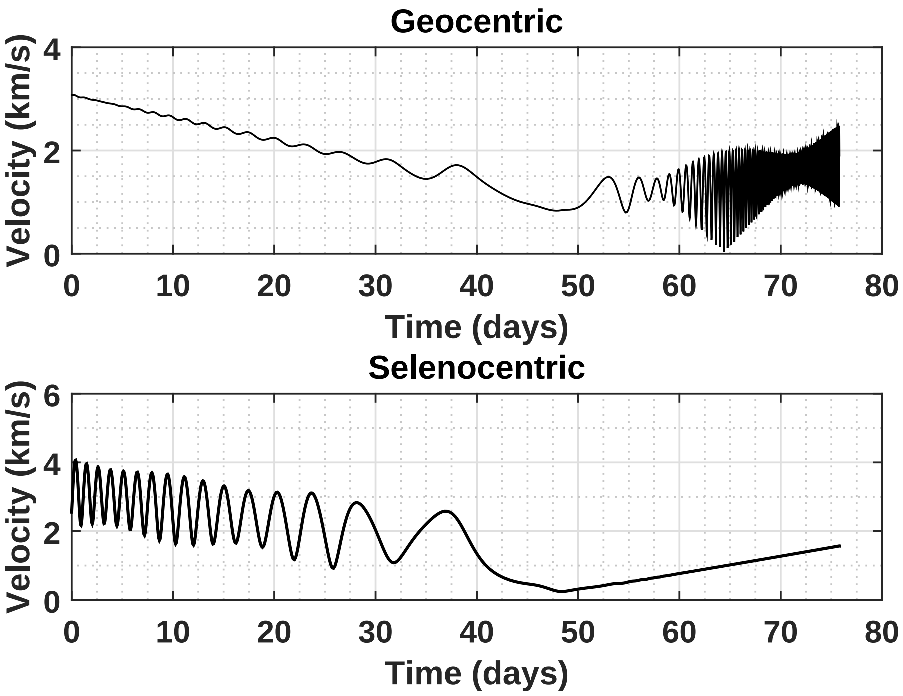

Fig. 6.4 Velocity magnitude profile for sample transfer.

Figure 6.3 plots the geocentric and selenocentric radial distance profiles. The bulk of the increment in radial distance from the Earth happens when the spiral phase is completed. During the circularization, the low frequency oscillation in the plot is due to the Moon's orbit around the Earth being slightly eccentric. From figure 6.4, in the altitude lowering hase of the selenocentric trajectory, the velocity smoothly rises as the altitude lowers without visible oscillations. This implies that in this phase the trajectory is nearly circular all the time and the osculating orbit eccentricity is close to zero at all times.
The significance of this in comparison to results from literature is that it has been obtained in a single optimizer run without splitting the trajectory into distinct phases. The optimal control formulation guarantees the optimality as there are no split trajectory phases that need to be inputs to a higher level parameter optimization routine.

6.2.2 Parametric studies on Earth-Moon transfers

Here a lunar transfer from an 18° inclined GSO to the Earth's equator to 250km lunar parking orbits of varying inclinations to the Earth's equatorial plane are performed. The variation in flight duration and fuel fraction are plotted.

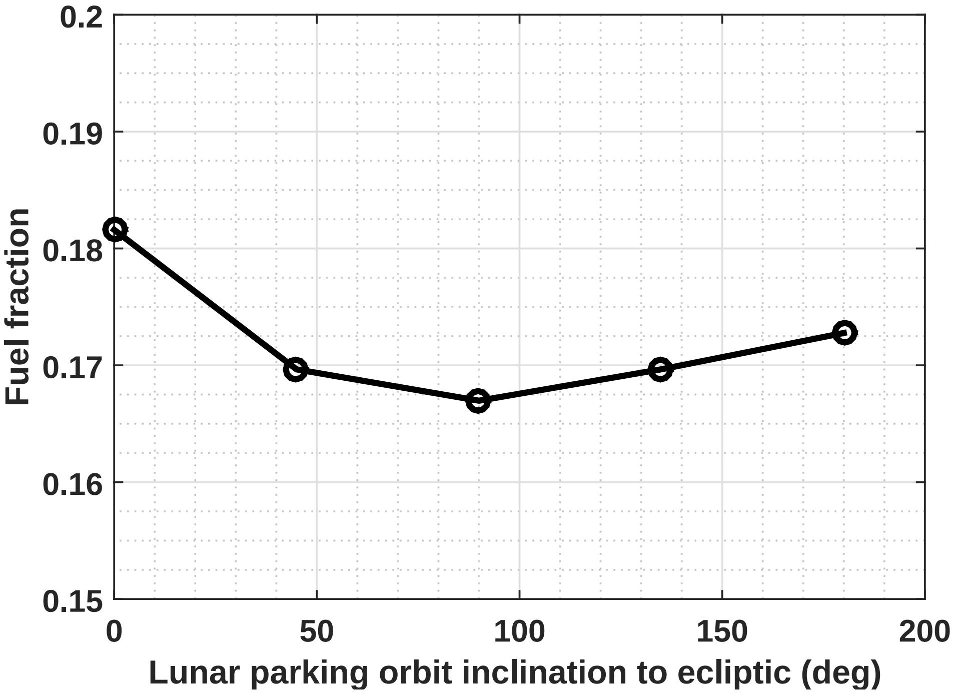

Fig. 6.5 Fuel fraction with varying lunar parking orbit inclination.

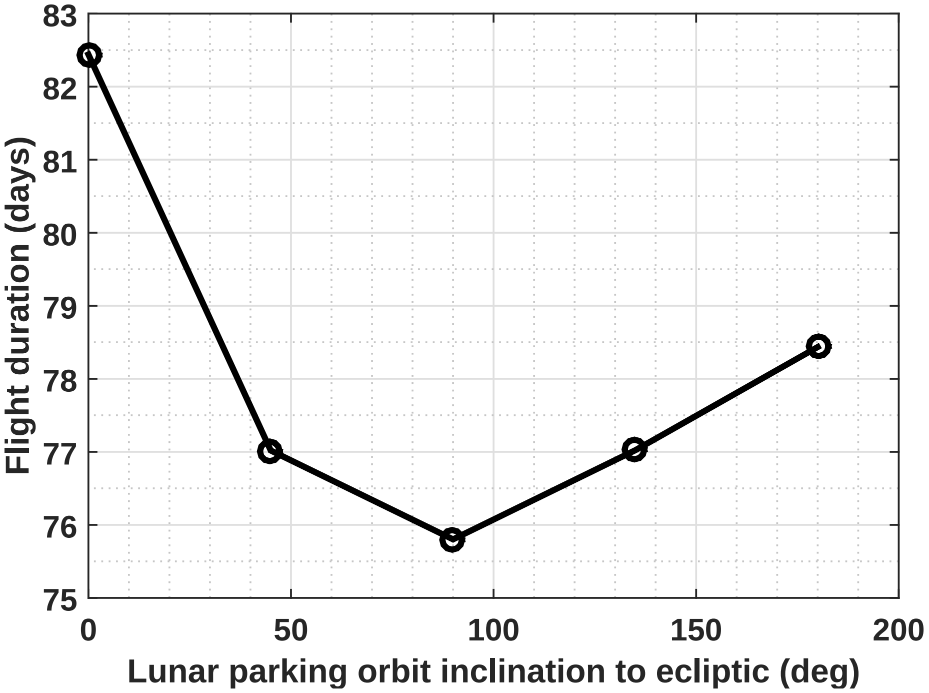

Fig. 6.6 Flight duration variation with varying lunar parking orbit inclination.

Figure 6.5 and 6.6 shows the variation in fuel fraction for the aforementioned transfer. It is seen that orbits perpendicular to the Earth's equatorial plane are seen to require the least amount of propellant for the given initial GSO inclination. Another observation is that the impact of the arrival lunar parking orbit inclination is minimal in terms of fuel fraction. The change in flight duration is in the order of one week over the 180° range of inclinations.

Table 6.1 GTO-GSO fuel fraction comparison with varying flight duration for 500mN thrust.

GSO inclination	Fuel fraction	Flight duration (days)
0° - Sea Launch	0.15166	68.852
18° - SDSC-SHAR	0.16697	75.802

Table 6.1 tabulates results for transfers to a 250km lunar parking orbit inclined at 90° to the Earth's equatorial plane starting from GSOs with different inclinations. The same spacecraft as in the previous figures is considered. It is seen that the initial orbit inclination has a significant impact on the flight duration with the transfer from a GSO inclined at 18° taking one week more. The fuel fraction penalty is in the order of 1.5%. This effect of the initial orbit inclination is pronounced as the Moon is in the gravity well of the Earth. This

causes large plane change maneuvers to be quite expensive. The cheapest transfer would be to have the initial Earth parking orbit in the plane of the Moon's orbit around the earth. Nonetheless, it is seen that even a 18° change in inclination of the EPO has minimal effect on the overall propellant requirement. This is due to the high specific impulse of the electric propulsion system which tends to reduce the sensitivity of the propellant fraction to the maneuver's total ΔV. The figures 6.1 and 6.2 depict the case for a launch from SDSC-SHAR to the aforementioned 90° orbit.

6.3 Earth-Mars transfers

The results of this problem are presented as a case study. This problem involves three major gravitating bodies along with the spacecraft. The transfer is performed between the respective planetary parking orbits. Both fuel and time optimal transfers are considered. Appropriate frame switchings are done when the spacecraft is in a planet's mean sphere of influence in order to reduce numerical sensitivity in accordance to the theoretical results outlined above. Nah et al. (2001) and Genta and Maffione (2016) have solved the problem of transferring a spacecraft from LEO to LMO. They have opted for a three stage approach with the trajectory split into maximum energy Earth escape, interplanetary phase and a Mars capture phase. In the current work, for the minimum time formulation where the parking orbits are sufficiently high. It is found that splitting the trajectory into multiple phases is unnecessary and the TPBVP is solved by DE. For problems where the parking orbit altitudes are very low, it becomes necessary to perform a split trajectory design else the computational time spikes up rapidly.

6.3.1 Trajectory design splitting strategy

Since it becomes necessary to split the trajectory into at least two phases, it is chosen to perform this after escape from the Earth. It is seen that even low thrust propulsion systems are capable of delivering a positive hyperbolic excess velocities when the spacecraft reaches the boundary of the Earth's sphere of influence. This makes it critical to orient this excess velocity vector in the optimal direction. This could be put into the problem formulation as a parameter optimization problem where the magnitude and direction of the excess velocity vector is to be optimized over several trajectory optimization runs. This is a computationally cumbersome exercise and the following strategy is chosen.

- If performing an outward transfer from a planet, target a heliocentric orbit with a semimajor axis about 2.5% to 5% greater than the departure planet (other orbital parameters same as the departure planet).

- If performing an inward transfer from a planet, target a heliocentric orbit with a semimajor axis about 2.5% to 5% lesser than the departure planet (other orbital parameters same as the departure planet).

Although this strategy cannot guarantee optimality of the transfer, it assures that the excess velocity vector is oriented in a near optimal direction. The final conditions in this phase need not be exactly achieved. It has been observed that the degree of achievement of the final orbit conditions in the first leg of the transfer has a negligible impact on the final transfer. This strategy allows for near optimal excess velocity vector determination without having to resort to parameter optimization techniques. The savings in computational time are significant.

6.3.2 Earth-Mars transfer: Case studies

Here a 1000kg NEP spacecraft with 2.0N of thrust with an I_{sp} of 4000s is transferred from a 500km circular EPO at -23.5° degree inclination to the Earth's equator to a 500km circular MPO at 90° to Mars equator. The fuel optimal formulation is used with the proposed splitting strategy. The departure epoch is set at JD 2459000.0 which corresponds to 30^{th} May 2020, 12:00 hours. Figure 6.7 shows the Earth escape phase. The projection of the orbit onto the ecliptic plane is shown here. It is visible that the escape occurs through means of a large number of spirals initially. The final phase of the escape is hyperbolic with respect to the Earth and is no longer represented by spiral dynamics. This leads to approaches that approximate the Earth escape by spiral dynamics to be inaccurate. Figure 6.8 shows the capture spiral at Mars projected onto the ecliptic plane (Thus the circular orbits appear as ellipse with the center as the origin). The final orbit is a circular polar Martian orbit with the right ascension of the ascending node of 0°. From the figure, it is visible that initially the orbital plane of the Mars capture orbit is slightly different from the desired value. This osculating plane slowly rotates to it's final position over the course of the spirals. The thrust vectors are not plotted in these two figures due to the density of the spirals. However, the thrust vector is almost always tangential and prograde during the Earth escape phase and in the Mars capture phase, the thrust vector is almost always tangential and retrograde. In case the final MPO is not circular, it is possible that the thrust vector can have significant deviations from the tangential retrograde direction.

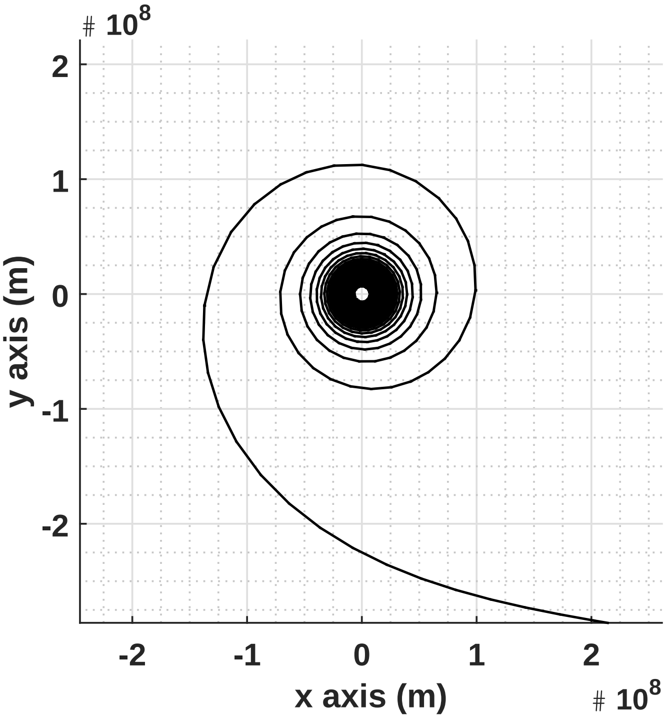

Fig. 6.7 Earth escape trajectory.

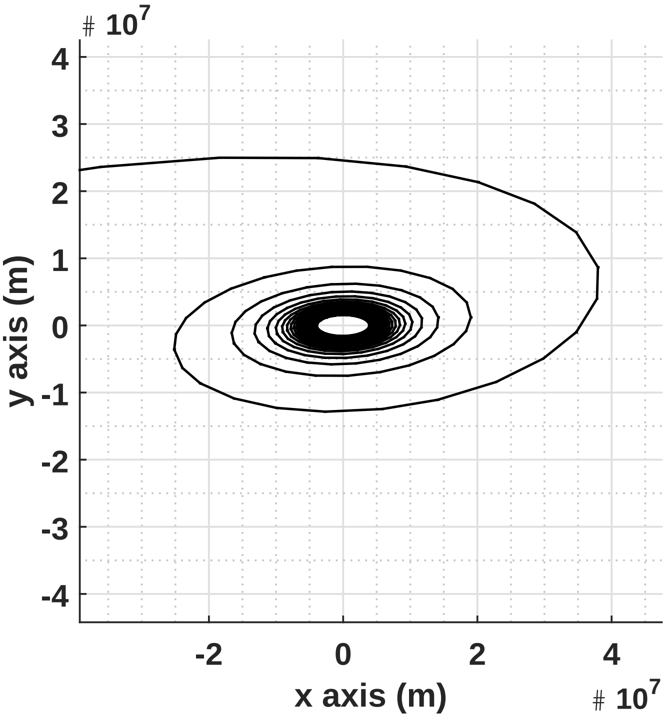

Fig. 6.8 Mars capture trajectory.

Figure 6.9 is the plot of the trajectory as seen from the heliocentric frame. The Earth escape and Mars capture phases are visible as the portions of the optimal trajectory which follow the paths of the respective planets. The Earth escape and Mars capture portions of the trajectory in the heliocentric frame appear to be corkscrewing around the planets. This is not visible in this frame due to the relative magnitudes of the distances. The interplanetary phase is a fuel optimal trajectory with the thruster being inactive in the middle of the interplanetary phase.

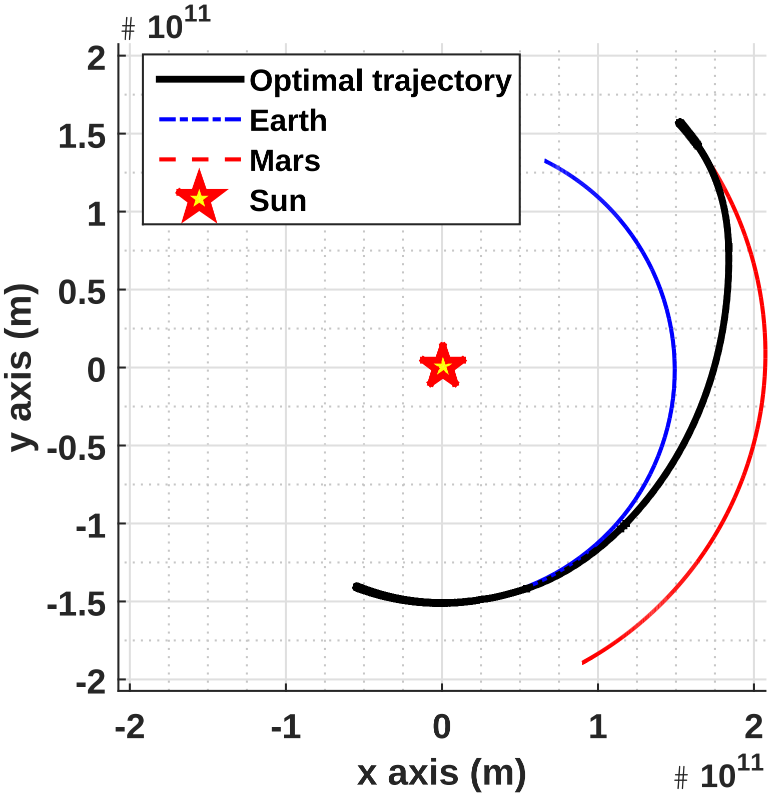

Fig. 6.9 Mars capture trajectory.

Figure 6.10 shows the plots of radial distance profiles as seen from various frames. Unlike in simple orbit to orbit transfers, it is seen that a significant portion of the transfer is spent in the escape and capture phases. This is made evident by the portions of the geocentric and Mars-centric plots that lie very close to their respective x axes.

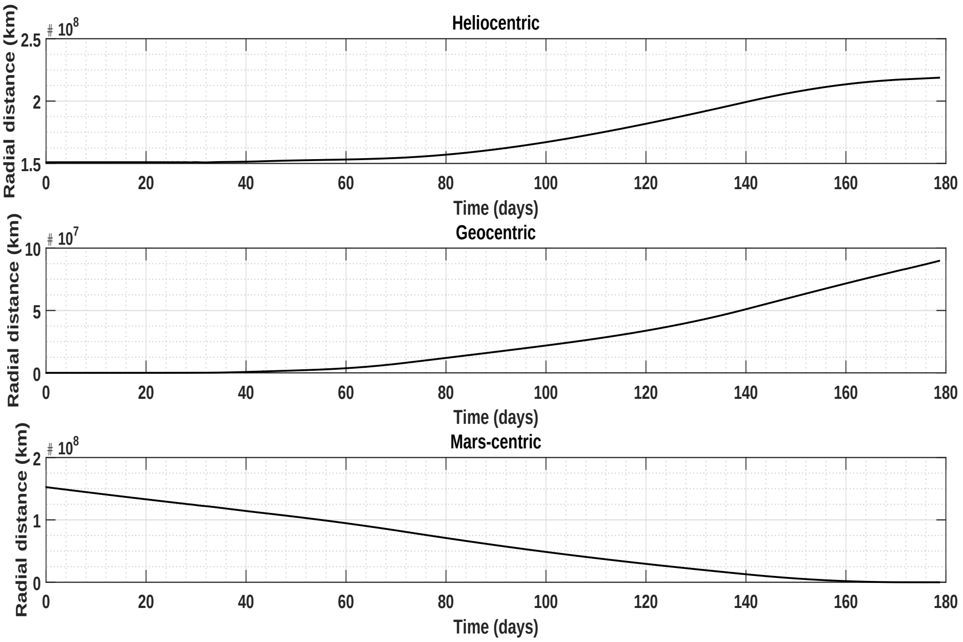

Fig. 6.10 Radial distance profiles.

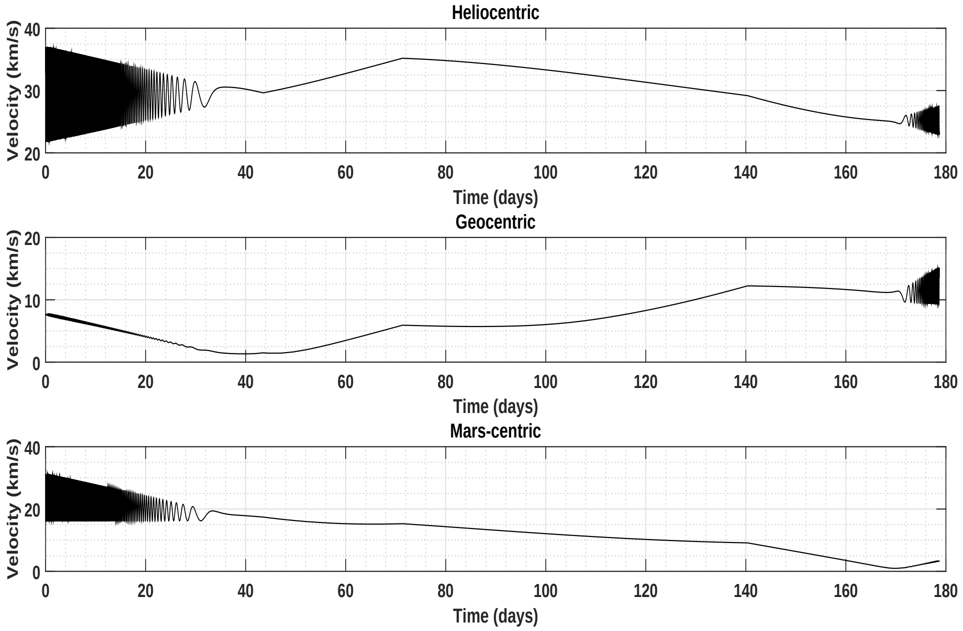

Fig. 6.11 Velocity magnitude profiles.

Figure 6.11 shows the plots of the velocity magnitude profiles as seen from various frames. The initial phase in the geocentric plot shows slight oscillations. This is indicative of the escape spiral trajectory no longer being exactly circular at every instant. The final phase of the Mars-centric trajectory is a smooth line with no visible oscillations. This implies that the final capture trajectory is a very close approximation to a circular trajectory. It can be concluded that the final altitude lowering is very well represented by spiral dynamics for this spacecraft's acceleration levels. The density of the oscillations in the heliocentric phase during the Earth escape and Mars capture phases is representative of the huge number of revolutions that the spacecraft executes around the planets. The total transfer time is 178.7 days with a fuel fraction of approximately 0.482.

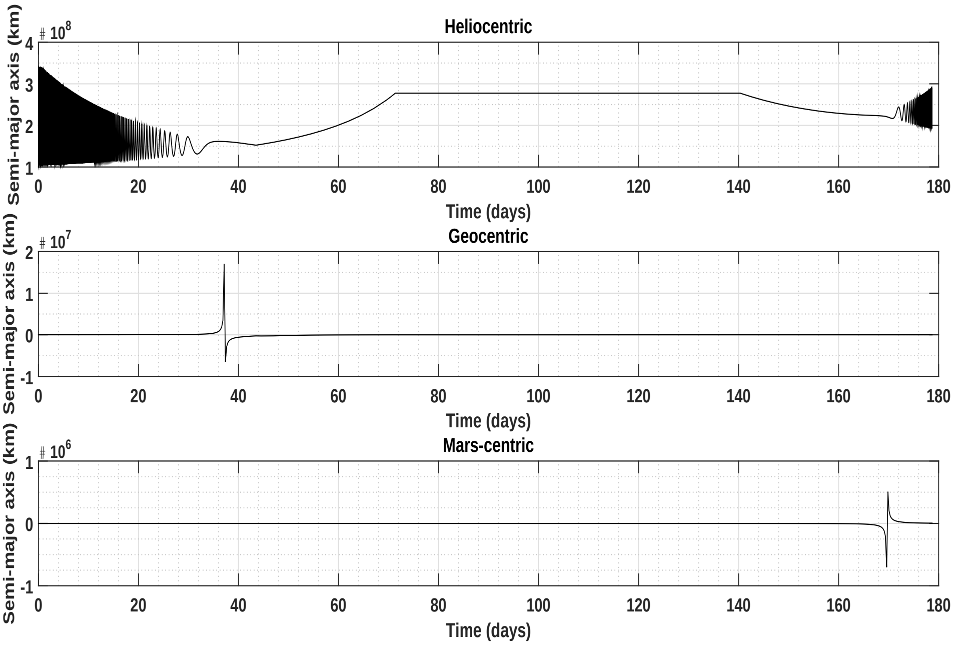

Fig. 6.12 Semi-major axis profiles.

Figure 6.12 shows the semi-major axis profiles. These profiles help in determining the exact times when Earth escape and Mars capture occur. They are visible as kinks in the profile as planetary escape or capture involve the transition of the orbit from a hyperbola to an ellipse or vice versa in the planetocentric frame of reference. The Earth escape is seen to occur on the 37.14^{th} day and the Mars capture occurs on the 169.6^{th} day. The Mars capture phase is thus seen to last only 9.1 days while the earth escape phase is more than four times as long. This is due to the spacecraft being lighter on arrival at Mars along with Mars having a much weaker gravity field. This gives the spacecraft a greater control over it's orbital parameters than during departure from the Earth. In case the arrival planet is much heavier, this situation may reverse. In the heliocentric plot, it is visible that the semi-major axis rises to a higher level than necessary in the interplanetary phase and then is lowered to an appropriate value. This suggests that there is still scope for improving the fuel fraction. This can be done by increasing the flight duration or the thrust levels. This plot is representative of the maneuver's efficiency and indicates wastage of energy if any. In this case, significant wastage of energy occurs in order to satisfy the flight duration value. The flat portion of the plot is the coasting region where the thruster is inactive. This region was automatically produced by the optimization technique and no user input was necessary. This is possible due to the fuel optimal formulation.

6.3.3 Effect of thrust level variation on fuel optimal Earth-Mars trajectories

Genta and Maffione (2016) performs a transfer with a variable specific impulse, variable thrust level spacecraft with both NEP and inverse square SEP models. The formulation utilized had the specific impulse as a control with the thrust level set by the power availability and thruster efficiency which were modeled to be constant in the NEP case. This formulation does not allow for coasting. For comparison, a single operating point of the spacecraft was chosen from optimal plot given in the paper. This corresponds to a specific impulse of 4000s and an initial acceleration of $2.11 mm/s^2$ based on the instantaneous power to mass ratio of the spacecraft considered in the paper. In order to obtain conservative figures, the lower acceleration values of $2.00 mm/s^2$ and $1.5 mm/s^2$ were chosen with an NEP spacecraft initial mass of 1000kg. This fixes the two chosen thrust levels at 2N and 1.5N respectively. The optimal trajectory design procedure was followed for the two chosen initial acceleration levels and the results are shown in table 6.2. The flight durations are not fixed at exactly 180 days. Instead, a small tolerance of ± 2.5 days is provided. This is done to make it easier for DE to converge to a feasible solution.

Table 6.2 Earth-Mars transfers between 500km parking orbits with varying thrust levels.

Spacecraft considered	Fuel fraction	Flight duration (days)
Genta and Maffione (2016) NEP	0.53700	180.00
$1.50N$ thrust, 4000s I_{sp}	0.52656	182.40
$2.00N$ thrust, 4000s I_{sp}	0.48234	178.70
$2.11N$ thrust, 4000s I_{sp}	0.47470	179.10

From the table, it is seen that using a fixed operating point thruster in the fuel optimal framework with bang-bang control structures is superior to an energy optimal formulation which allows for smooth variation in the specific impulse. The disadvantage in the fuel optimal formulation is that the TPBVP is numerically much more sensitive and difficult to solve. This has been addressed in the current project by the application of differential evolution. This makes the use of techniques like homotopy unnecessary. If exact computed $2.11N$ thrust is used without using the conservative figure of $2.0N$, it is possible to get even better savings in fuel fraction for a 180 day Earth-Mars transfer. The maximum fuel fraction savings possible with the fixed operating point-NEP spacecraft in the fuel optimal framework is 6.23%. There is no penalty on the flight duration with this approach when compared to the variable specific impulse energy optimal trajectory in the reference paper. Genta and Maffione (2016) recognize that it would be beneficial to switch off the thruster in the spacecraft they have considered during the high specific impulse, low thrust phases. The formulation pursued by them does not allow for such switches. The current work solves that issue but with the drawback of allowing the I_{sp} only to be an external spacecraft parameter and not a control variable.

It is possible to derive a fuel optimal control law with all the acceleration components and specific impulse set as control variables with appropriate constraints on the thrust level and specific impulse connected by the power availability. This will result in a bang-bang control structure with the specific impulse either at the maximum or minimum values with the thruster either at the maximum possible level or at zero. Further details are available in appendix C

References

Anderson, R. L. and Lo, M. W. (2009). Role of Invariant Manifolds in Low-Thrust Trajectory Design. *Journal of Guidance, Control, and Dynamics*, 32(6):1921–1930.

Arthur. E, B. and Ho, Y.-C. (1975). *Applied optimal control: Optimization, estimation, and control (revised edition)*. Taylor & Francis.

Betts, J. T. (1998). Survey of Numerical Methods for Trajectory Optimization. *Journal of Guidance, Control, and Dynamics*, 21(2):193–207.

Betts, J. T. (2000). Very low-thrust trajectory optimization using a direct SQP method. *Journal of Computational and Applied Mathematics*, 120(1-2):27–40.

Betts, J. T. and Erb, S. O. (2003). Optimal low thrust trajectories to the moon. *SIAM Journal on Applied Dynamical Systems*, 2(2):144–170.

Casalino, L. and Simeoni, F. (2012). Indirect Optimization of Asteroid Deflection Missions with Electric Propulsion. *Journal of Guidance, Control, and Dynamics*, 35(2):423–433.

Chiravalle, V. P. (2008). Nuclear electric ion propulsion for three deep space missions. *Acta Astronautica*, 62(6-7):374–390.

Circi, C. (2004). Mars and Mercury Missions Using Solar Sails and Solar Electric Propulsion. *Journal of Guidance, Control, and Dynamics*, 27(3):496–498.

Conway, B. A. (2014). *Spacecraft trajectory optimization*, volume 29 of *Cambridge Aerospace Series*. Cambridge University.

Edelbaum, T. N. (1961). Propulsion Requirements for Controllable Satellites. *ARS Journal*, 31(8):1079–1089.

Falck, R. and Dankanich, J. (2012). Optimization of low-thrust spiral trajectories by collocation. In *AIAA/AAS Astrodynamics Specialist Conference*, page 4423.

Falck, R. D., Sjauw, W. K., and Smith, D. A. (2014). Comparison of low-thrust control laws for applications in planetocentric space. In *50th AIAA/ASME/SAE/ASEE Joint Propulsion Conference*, page 3714.

Feagin, T. (2007). A tenth-order Runge-Kutta method with error estimate. In *Proceedings of the IAENG Conference on Scientific Computing*.

Genta, G. and Maffione, P. (2016). Optimal low-thrust trajectories for nuclear and solar electric propulsion. *Acta Astronautica*, 118:251–261.

Gopinath, N. (2003). Optimal low thrust orbit transfer from gto to geosynchronous orbit and stationkeeping using electric propulsion system. In *54th International Astronautical Congress of the International Astronautical Federation, the International Academy of Astronautics, and the International Institute of Space Law*, pages A–7.

Hoskins, W. A., Cassady, R. J., Morgan, O., Myers, R. M., Wilson, F., King, D. Q., and DeGrys, K. (2013). 30 years of electric propulsion flight experience at Aerojet Rocketdyne. In *33rd International Electric Propulsion Conference*, pages 1–12.

Kim, M. (2005). Continuous low-thrust trajectory optimization: Techniques and Applications, PhD dissertation.

Kirk, D. E. (2012). *Optimal control theory: an introduction*. Courier Corporation.

Kluever, C. A. and Pierson, B. L. (1997). Optimal earth-moon trajectories using nuclear electric propulsion. *Journal of Guidance, Control, and Dynamics*, 20(2):239–245.

Kugelberg, J., Bodin, P., Persson, S., and Rathsman, P. (2004). Accommodating electric propulsion on SMART-1. *Acta Astronautica*, 55(2):121–130.

Lev Semenovich, P. (1987). *Mathematical Theory of Optimal Processes*, volume 4 of *Classics of Soviet Mathematics*. CRC Press.

Mingotti, G., Topputo, F., and Bernelli-Zazzera, F. (2009). Low-energy, low-thrust transfers to the moon. *Celestial Mechanics and Dynamical Astronomy*, 105(1-3):61.

Nah, R. S., Vadali, S. R., and Braden, E. (2001). Fuel-Optimal, Low-Thrust, Three-Dimensional Earth-Mars Trajectories. *Journal of Guidance, Control, and Dynamics*, 24(6):1100–1107.

Patel, P., Scheeres, D., and Gallimore, A. (2006). Maximizing Payload Mass Fractions of Spacecraft for Interplanetary Electric Propulsion Missions. *Journal of Spacecraft and Rockets*, 43(4):822–827.

Pérez-Palau, D. and Epenoy, R. (2018). Fuel optimization for low-thrust Earth–Moon transfer via indirect optimal control. *Celestial Mechanics and Dynamical Astronomy*, 130(2).

Price, K., Storn, R. M., and Lampinen, J. A. (2005). *Differential Evolution: A Practical Approach to Global Optimization*. Natural Computing Series. Springer.

Quarta, A. A., Izzo, D., and Vasile, M. (2013). Time-optimal trajectories to circumsolar space using solar electric propulsion. *Advances in Space Research*, 51(3):411–422.

Racca, G. D. (2001). Capability of solar electric propulsion for planetary missions. *Planetary and Space Science*, 49(14-15):1437–1444.

Ramanan, R. and Lal, M. (2005). Analysis of optimal strategies for soft landing on the moon from lunar parking orbits. *Journal of earth system science*, 114(6):807–813.

Rauwolf, G. A. and Coverstone-Carroll, V. L. (1996). Near-optimal low-thrust orbit transfers generated by a genetic algorithm. *Journal of Spacecraft and Rockets*, 33(6):859–862.

Rayman, M. D., Chadbourne, P. A., Culwell, J. S., and Williams, S. N. (1999). Mission design for deep space 1: a low-thrust technology validation mission. *Acta astronautica*, 45(4-9):381–388.

Rayman, M. D., Fraschetti, T. C., Raymond, C. A., and Russell, C. T. (2006). Dawn: A mission in development for exploration of main belt asteroids Vesta and Ceres. *Acta Astronautica*, 58(11):605–616.

Sankovic, J. M., Hamley, J. A., and Haag, T. W. (1994). Performance evaluation of the Russian SPT-100 thruster at NASA LeRC.

Sánchez-Sánchez, C. and Izzo, D. (2018). Real-Time Optimal Control via Deep Neural Networks: Study on Landing Problems. *Journal of Guidance, Control, and Dynamics*, pages 1–14.

Storn, R. and Price, K. (1997). Differential evolution–a simple and efficient heuristic for global optimization over continuous spaces. *Journal of global optimization*, 11(4):341–359.

Stuhlinger, E. (1964). *Ion propulsion for space flight*. Mc-Graw Hill, New York.

Williams, S. N. and Coverstone-Carroll, V. L. (1997). Benefits of Solar Electric Propulsion for the Next Generation of Planetary Exploration Missions. *Journal of the Astronautical Sciences*, 45(2):143–159.

Yam, C. H., McConaghy, T. T., Chen, K. J., and Longuski, J. (2004). Preliminary design of nuclear electric propulsion missions to the outer planets. In *AIAA/AAS Astrodynamics Specialist Conference and Exhibit*, page 5393.

Appendix A

Differential Evolution for Low Thrust Trajectory Optimization

A.1 Introduction to Differential Evolution

Storn and Price (1997) in their seminal paper introduce a new heuristic search based global optimization method which they term as differential evolution. It was demonstrated to outperform several existing algorithms including adaptive simulated annealing. It is considered to be a subset of the broad genetic algorithm class of methods. Due to it's real valued representation, it has inherent advantages when dealing with continuous optimization problems as will arrive from low thrust transfer problems. Gradient information is not required and also, this technique works well for problems with high dimensionality.

A.2 Basic DE Algorithm

Let f be a function from $\mathbb{R}^n$ to $\mathbb{R}^1$. No conditions are imposed on the smoothness of this function. Elements of the domain of this function are termed as population members and elements of the range are denoted as cost value corresponding to the population member. This function is called the cost function which we want to minimize based on several additional inequality and equality constraints on the agents. The constrained optimization problem can be converted into an unconstrained problem through the use of techniques like penalty functions. Thus the same minimization algorithm developed for unconstrained problems can be utilized. It is also possible to make use of the concept of pareto-optimality while dealing with multi-objective problems.

The algorithm is as follows,

- For every population member **x**,
  - Pick 3 mutually distinct random population members **a**, **b** and **c** which are also distinct from **x**.
  - Pick a random integer from 1 to the n where n is the dimensionality of the problem being solved.
  - For each i from 1 to n, compute a new potential population member **y** as follows.
    - Pick a uniformly distributed r_i from 0 to 1.
    - If $r_i < CR$ or $i = R$, then set $y_i = a_i + F(b_i - c_i)$
    - Else set $y_i = x_i$.
  - If $f(\mathbf{y}) < f(\mathbf{x})$, replace **x** with **y**.
- Iterate over all the population members to complete 1 generation.
- Iterate till the required number of generations or until the cost function of the best agent goes below a set value.
- Return the population member with the minimum cost as the best solution.

A.3 Parallelization of DE algorithm

In order to enable the determination of solutions to large sized problems, it becomes necessary to allow for the numerical methods to use extensive amounts of computer hardware. Most desktop computers as of today are equipped with at least a dual core CPU. This means that two tasks or threads can concurrently run on the same machine at any given point of time. Conventional programming techniques allow for the generation of only one thread that can run when an executable/binary file is made to run. Special language dependent programming constructs are available to perform parallel computing. The two main types of parallelization are based on the hardware architecture. They are namely,

- Shared memory architecture
- Distributed memory architecture

Most desktops and workstations are of the shared memory parallel architecture. It involves a multiple core processor or multiple processors all sharing the same memory space. This means that all the data is available in one location and different cores can perform the specified instructions concurrently on the data or on different partitions of the data.
On the other hand, high performance clusters and supercomputers are of the distributed memory parallel architecture. They involve multiple nodes which are networked together by fast interconnect topologies. Each node can posses multiple processors and memory units which is shared by the processors internal to the node. In these architectures, the data is distributed in different locations and each node can usually operate only on the data it possess. To access non-local data, significant time is required to send, process and receive data from other nodes. Nonetheless, this type of architecture is massively scalable and the fastest supercomputers in the world currently are based on this computing architecture.
For the present study, DE has been parallelized in the shared memory architecture.

A.3.1 Parallelizing DE in shared memory architecture

This can be achieved with very high efficiency by decomposing the population members into individual groups that computer cores can work on. Each core only iterates over the batch of population members assigned to it. There are locks in place to prevent conflicts between different cores trying to overwrite data which is being used by other cores. Since all the cores can access the entire population, there are no communication requirements to perform the mutation operation. This has been implemented in standard C++17 and the efficiency of parallelization has been noted in 2, 4 and 8 core machines.

Table A.1 DE performance in a dual core 2.6GHz machine.

25 dimensional Rastrigin function			1 thread	2 threads	4 threads	
Lower bounds	Upper bounds	Generations	Time(ms)	Time(ms)	Time(ms)	Max Speedup
-1	1	1000	857.626	546.38	379.27	2.26
-10	10	1750	1460.03	934.662	621.439	2.35
-100	100	1950	1613.14	1021.72	682.483	2.36
-1000	1000	2125	1764.25	1088.09	751.529	2.35
-10000	10000	2350	1954.39	1202.36	816.597	2.39
	Solution	(0,0, . . . ,0)				

Individual steps of DE do not involve any sort of sorting or other global reconfigurations of the data which tend to be inherently sequential. This leads to very high parallelization efficiency based on Amdahl's law. Super-linear speedup has been consistently observed in some of the machines due to efficient cache behavior. Typically, it is advisable to load about 2 to 5 threads per core available. This is to eliminate the possibility of a core finishing all the tasks assigned and idling. Increasing the number of threads beyond a certain limit will have diminishing returns and beyond that, there will be performance loss due to thread creation overhead and switching between the threads. Consistent speedup has been observed for all problems attempted. Table A.1 presents the results for the solution to a 25 dimensional Rastrigin function. This function has several local minima and the high dimensionality makes this a very difficult problem to handle. Nonetheless, DE has proven itself to reliably obtain the global optimum for every set of bounds on the search domain. Other such examples can be found in the book by Price et al. (2005).

A.3.2 Parallelizing DE in distributed memory architecture

Implementing DE in this architecture can be performed using multiple strategies, a few of which are as follows,

- Decomposition of population
- Decomposition of the search domain
- Distributing the evaluation of the cost function

Decomposition of the population will lead to severe communication requirements at every generation step. This will reduce the parallelization efficiency. Decomposing the search domain has advantages but in the field of trajectory optimization, all sub-domains may not need similar computational times for cost function evaluation. This can lead to severe load balancing and can lead to inefficiencies.

The third approach of distributing the evaluation of the cost function has merit when each cost function evaluation is computationally very expensive. The evolutionary algorithm is made to run on the head node while the cost function evaluations are offloaded to the alternative nodes as well as the head node. This has a fixed latency per generation and is scalable. Balancing the loads is much simpler with this mode of parallelization. It is possible to achieve this parallelization using frameworks like MPI (Message Passing Interface)

It is the opinion of the author that the effort spent in parallelizing DE in a distributed architecture will not pay off unless the cost function evaluations are a severe bottleneck for the optimization.

A.3.3 Parallelizing DE in a graphics processing unit

If the cost function evaluations involve solutions to extremely large systems of equations that arise from partial differential equations or extremely large systems of ordinary differential equations in the case of direct summation n-body simulations with large n, it may be beneficial to offload the cost function evaluation to a highly parallel single input multiple data (SIMD) processor like graphics processing units. These can be achieved through means of CUDA or OpenCL. Benchmarking double precision floating point arithmetic on a dual core Intel i7 4510U 2.6GHz processor vs a low end Nvidia GeForce 840M mobile graphics processor with 384 CUDA cores reveals that with appropriate tasks, a maximum speedup of 30 is possible with the graphics processing unit versus the CPU.

A.4 Parameter tuning for low thrust trajectory optimization

Figure A.1 shows the convergence pattern for a 200 day fuel optimal transfer from 1AU to 1.524AU orbits with an initial acceleration of $1mm/s^2$ and 2000s I_{sp}.

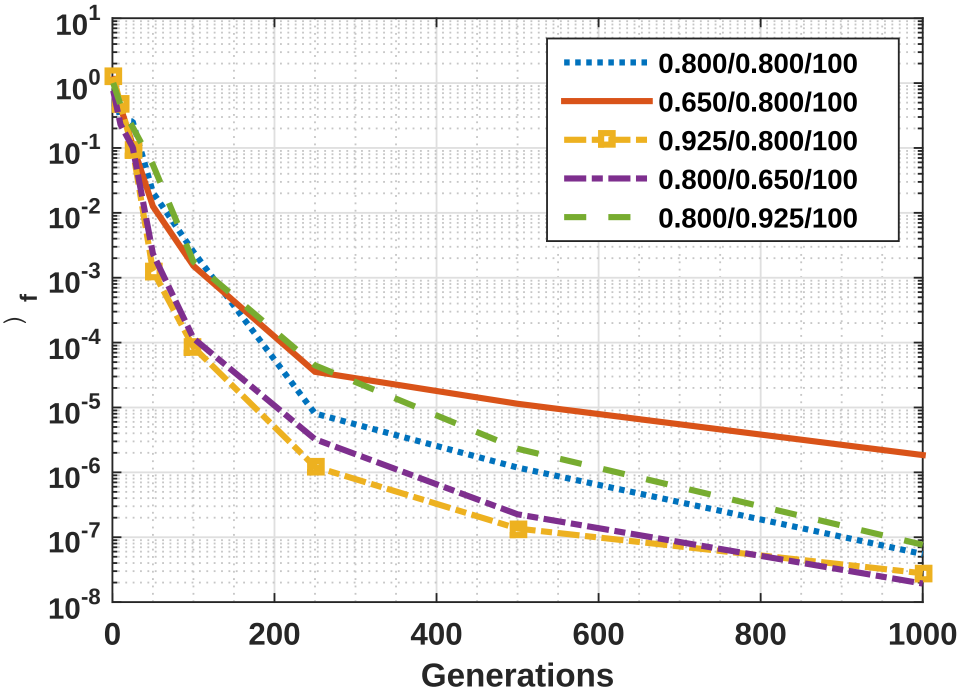

Fig. A.1 DE performance and convergence pattern.

It has been observed that CR/F ratios greater than unity lead to rapid convergence. Also, NP is set to at around 5 to 10 times the number of search variables. Beyond a certain number of generations, DE is found to saturate and not converge further, increasing NP alleviates this issue. Based on this plot, CR/F value chosen for all simulations is 0.9/0.8.

Appendix B

Optimal Lunar Landing

B.1 Introduction

In the absence of an atmosphere, landing a probe on the surface of a planet, moon or any other body can be achieved only through propulsive descent. These maneuvers involve significant periods of continuous thrusting where the thrust vector has to be steered significantly to achieve a soft landing.

There can be further constraints on the lander to be vertical to the ground by the end of the maneuver. These requirements have been addressed through optimal control theory to generate optimal trajectories for landing from orbit. DE has been used to solve the optimal control problem. A strategy has been arrived at to select the minimum thrust level required to perform the optimal phase of the descent. An effective and robust methodology to handle high thrust propulsive landing problems from orbit has been established in this study using differential evolution. Both time optimal and fuel optimal formulations can be used to obtain solutions. The state and costate dynamics along with the optimal control law remain unchanged even though this is a high thrust problem. For demonstration, propulsive landing on Jupiter's moon Callisto has been considered in this paper.

B.2 Results

B.2.1 Sample optimal landing trajectory

The problem considered here is landing a 1500kg initial mass spacecraft with a thrust of 2000N and I_{sp} of 315s. The current results are presented for the time optimal formulation. The initial orbit around Callisto is a 100x100km circular orbit. The terminal conditions are set as achieving an altitude 50m above the surface of Callisto with a downward velocity of only $0.75 m/s$. The horizontal component of velocity is set to be zero. This $50m$ altitude is considered as the target altitude as there needs to be a closed loop guidance procedure for the touch down phase as the surface topology may affect landing site location. This target altitude is also useful for sky-crane type of landing strategies which requires the lander to switch over from an optimal mode to a closed loop touchdown mode.

During descent as seen in figure B.1, the altitude of the spacecraft increases by a few meters initially. This increasing trend has been observed before in literature (Ramanan and Lal, 2005). This happens in the retrograde thrust phase where a significant fraction of the spacecraft's orbital velocity is negated. Due to the imposition of the optimal control law, a slight thrust angle exists off the tangential retrograde direction. This is the cause for the orbit raising. The next phase comprises of a rapid descent as the trajectory the spacecraft is elliptic with respect to Callisto. The final stage of the optimal trajectory involves a gradual drop in the altitude to the target value. This is essential for propulsive descent with a soft landing.

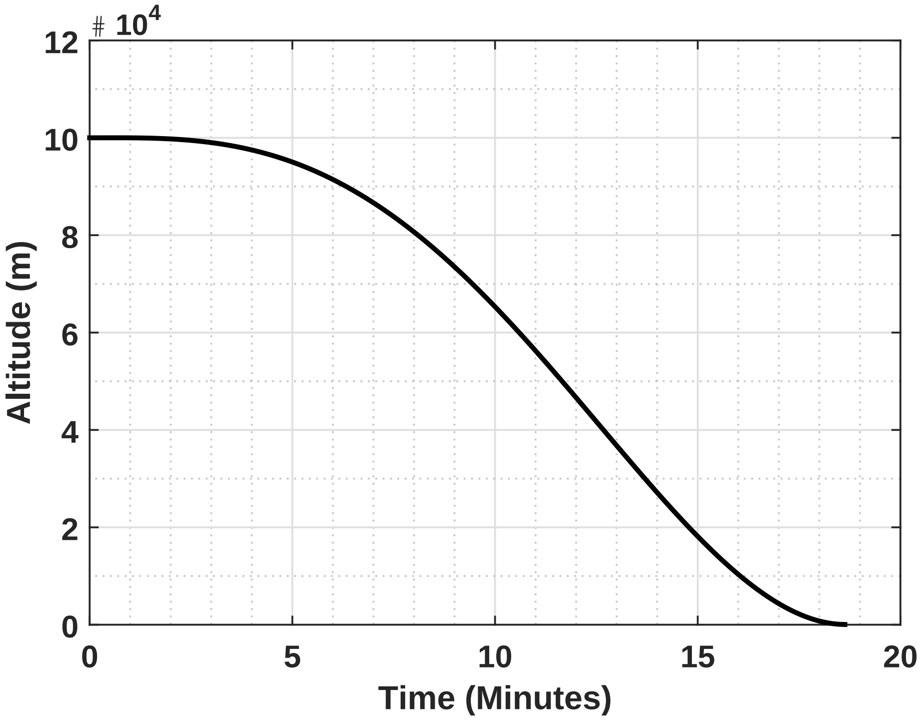

Fig. B.1 Altitude profile for time optimal descent.

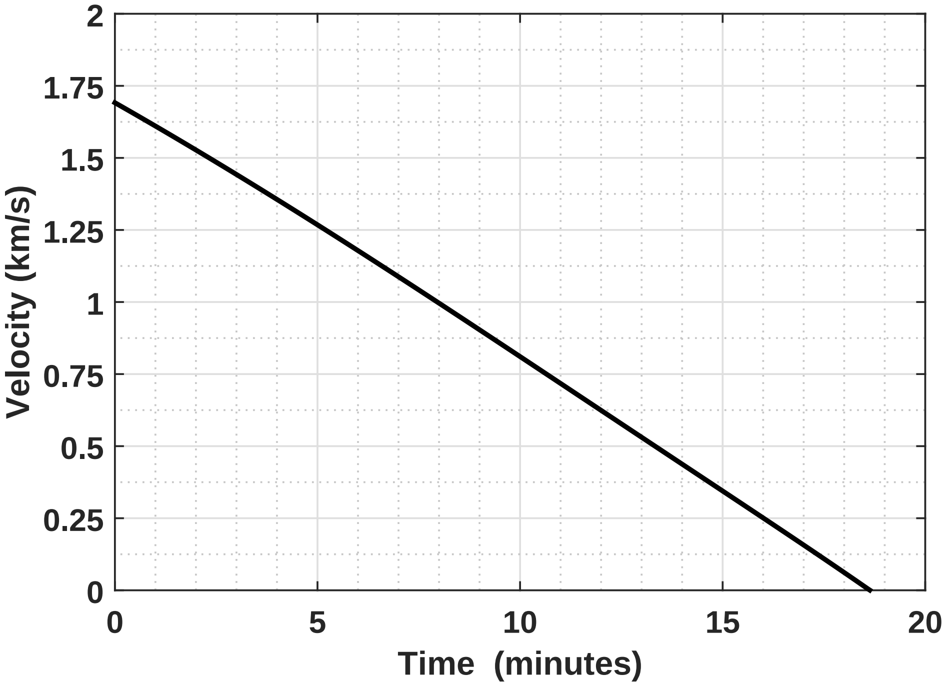

Fig. B.2 Velocity profile for time optimal descent.

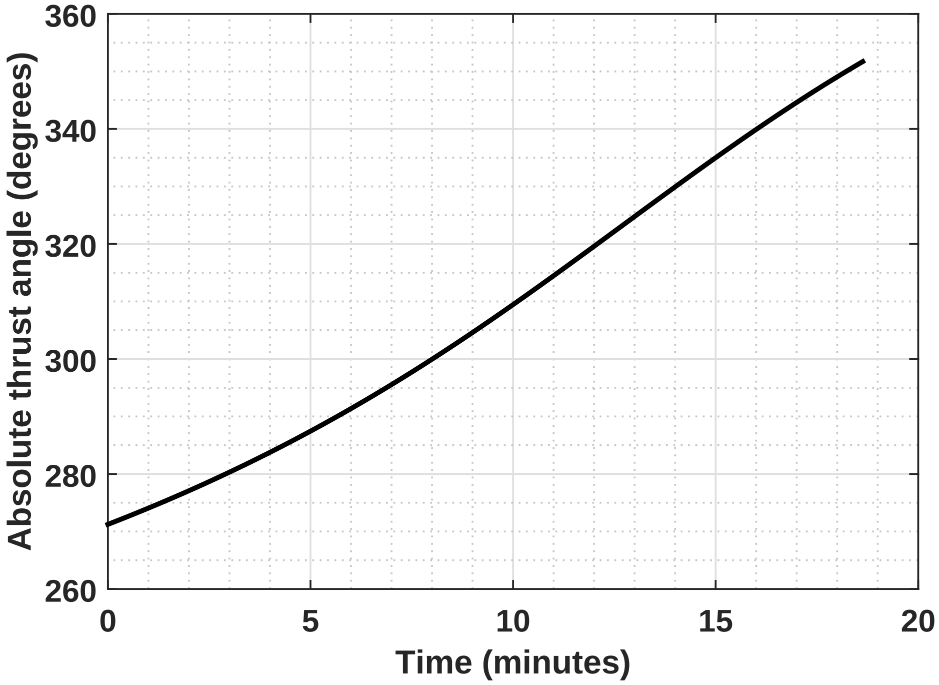

Fig. B.3 Thrust angle profile for time optimal descent.

In figure B.2, it is seen that the velocity of the spacecraft drops nearly linearly. The terminal deceleration at the end of the optimal phase is quite high as the thrusters are not throttled down. This leads to the requirement of imposing either acceleration limits in the optimal control formulation or by handling the terminal descent through a separate closed loop control. The latter strategy will be safer as it allows for the handling of landing obstacles in real time. In figure B.3, the thrust angle shows the steering requirement for the thruster. About 80^o worth of steering has to be performed by the attitude control thrusters. This is a small requirement and the steering rate is also quite low with a maximum of about 0.0863 degrees per second. This can be managed by even by small attitude control thrusters. It is concluded that the optimal control profile generated by a 3DOF code for landing does not impose any severe attitude control requirements.

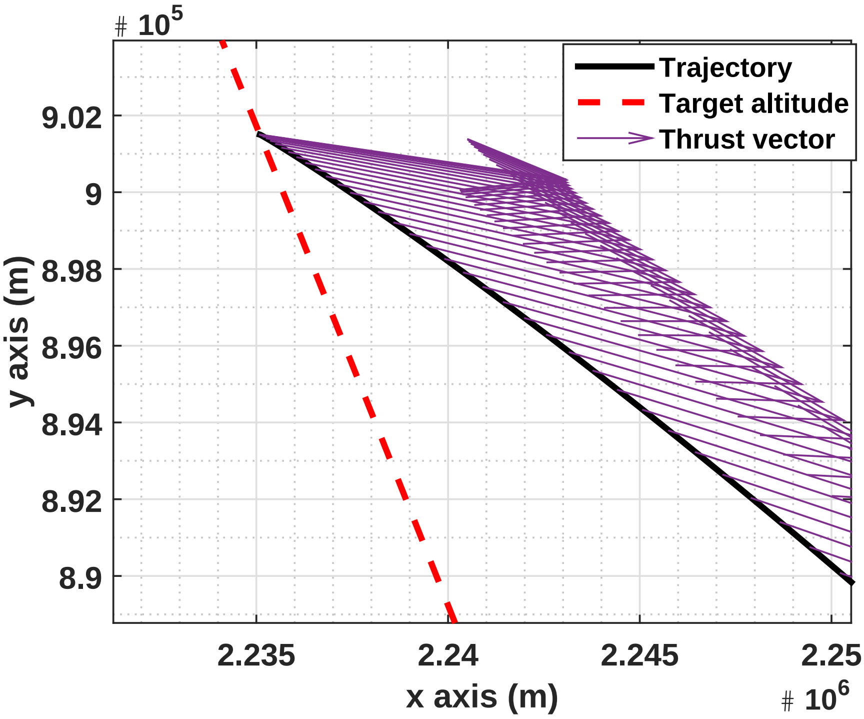

Fig. B.4 Final phase of optimal descent trajectory.

Fig. B.4 depicts the final trajectory phase of the lander as it approaches the target altitude 50m above the surface of Callisto. Due to the high acceleration, only at the final instant of time, is the target velocity achieved. Even though in the plot, it seems to appear that there is a significant horizontal component, it is actually reduced to zero only at the final time. This is yet another reason for the optimal phase to end at $50m$ above the surface. The high thrust levels involved in the optimal descent phase can lead to excessive control requirements if continued till touchdown. Once the optimal phase causes the lander to attain the fixed target altitude, the lander has to switch over to closed loop guidance and control for landing at much lower acceleration levels. Even though the subsequent strategy is sub-optimal, it leads to a much better controlled landing and lower impact loads. The final velocity is made vertical to the Callisto's surface with a value of $0.75 m/s$. Due to low velocity and high acceleration, this vertical velocity is achieved even though the approach of the lander prior to the terminal phase is significantly away from the vertical. This is made possible by the thrust steering law provided by the optimal control formulation.

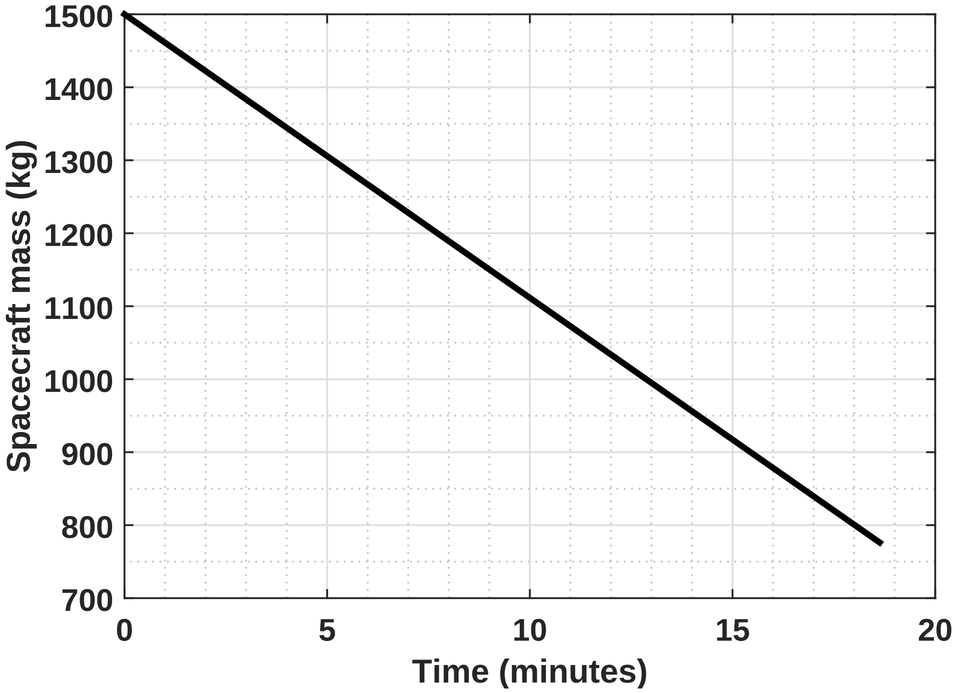

Fig. B.5 Spacecraft mass variation during descent.

Figure B.5 shows the variation of the spacecraft's mass during the descent. This is exactly linear as the thrust is constant without any throttle. Due to this, the thrust acceleration on the spacecraft varies from $1.333 m/s^2$ to $2.577 m/s^2$ with the magnitude linearly increasing with time. The maximum deceleration that the spacecraft experiences is still lesser than any launch loads and is thus safe.

B.2.2 Parametric studies: Time optimal results

Figures B.6 and B.7 present the results of a parametric study on the fuel fraction and peak altitude to initial altitude ratio as a function of the initial acceleration level.

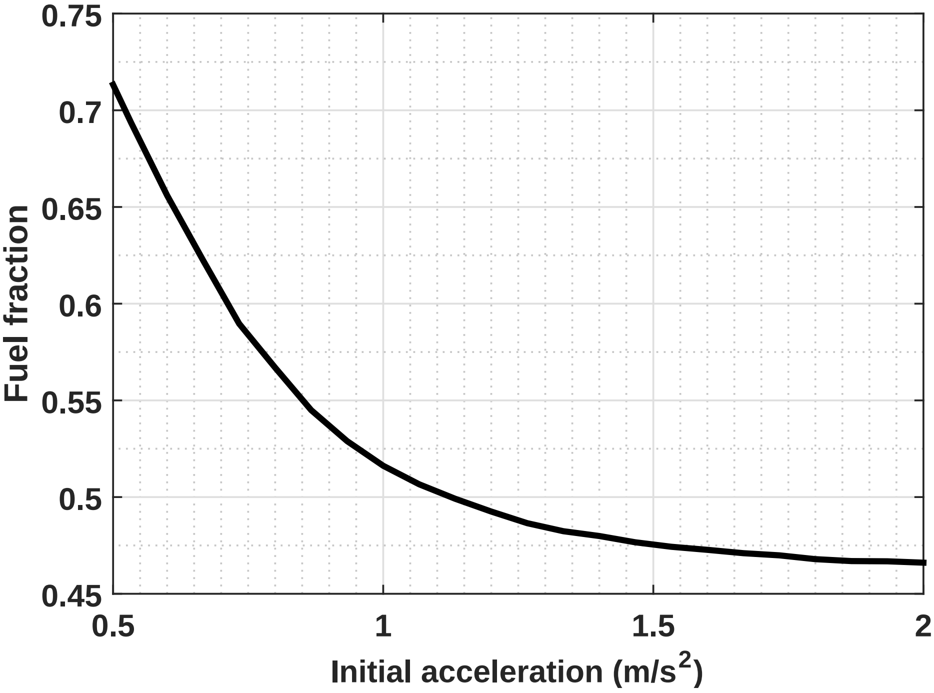

Fig. B.6 Influence of initial acceleration levels on fuel fraction.

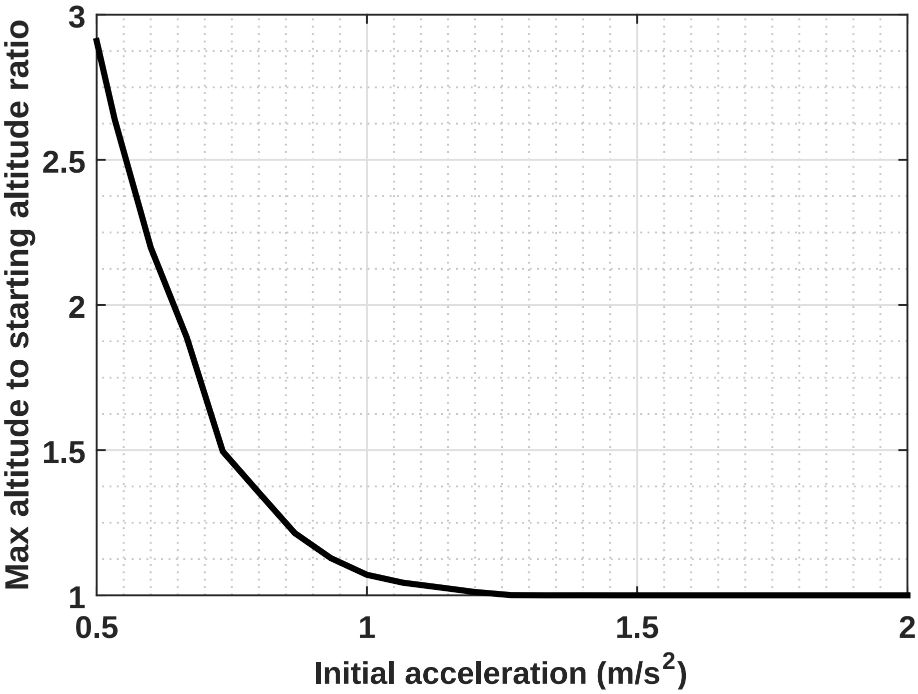

Fig. B.7 Influence of initial acceleration levels on the peak to initial altitude ratios.

The transfer geometry and thruster specific impulse are taken to be the same as in the previous problem. It is clear that for very low initial accelerations, the fuel fraction is considerably higher due to the peak altitude climbing above the initial level. This is done to bleed off some mass so that the spacecraft gets lighter in order for the propulsion system to be able to handle the spacecraft in the presence of the central body's gravity. The fuel fraction drops asymptotically to about 0.466 for this problem. Beyond a certain threshold thrust level, the trajectory only follows a downward path as the thrusters are now powerful enough to handle the entire spacecraft without having to bleed off extra mass. This study can be used to determine a suitable thruster configuration for a lander based on the fuel margins available and fix the minimum thrust level that would satisfy the weight constraints on the lander. These parametric studies have been done for the same initial and final orbits as the previous case.

B.2.3 Parametric studies: Influence of specific impulse

For this purpose, the same initial conditions are chosen but the final target altitude is set as 2km with the target velocity left free. The specific impulse is also varied by $\pm 5s$ from the nominal expected value. The propellant mass required by a 1500kg lander is depicted in figure B.8.

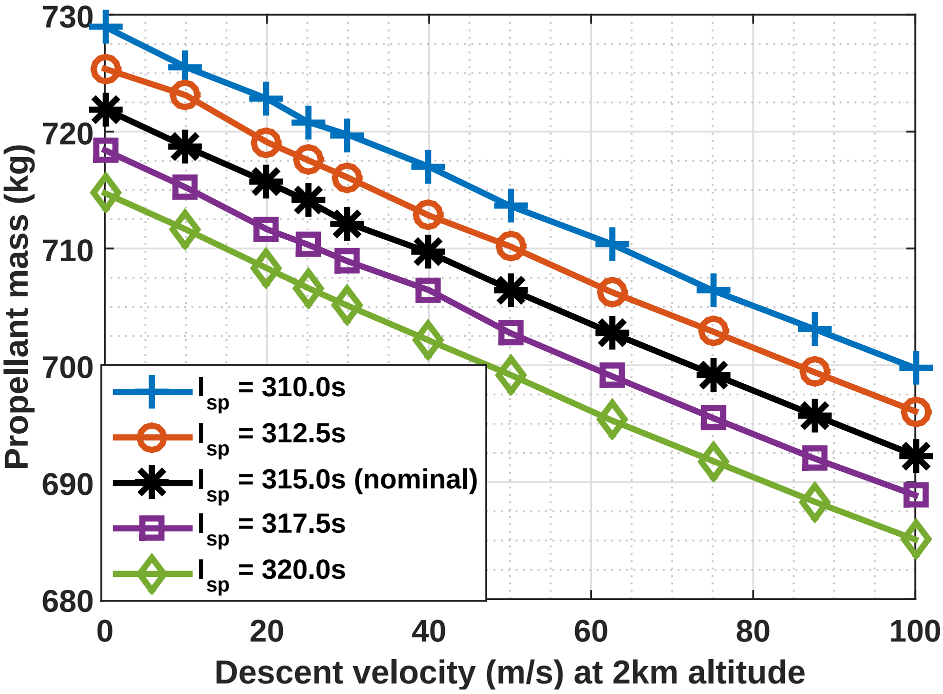

Fig. B.8 Propellant required vs final velocity of optimal phase.

This type of parametric study helps in determining reserve propellant volumes needed based on the control requirements and variations in the engine's specific impulse due to environmental and manufacturing effects.

B.2.4 Parametric studies: Fuel optimal results

Here the problem of landing an 874kg spacecraft with a 2200N thruster from a $100km \pm 15km$ orbit around Earth's moon is considered with a target altitude of $0m$ and a target velocity of $0m/s$.

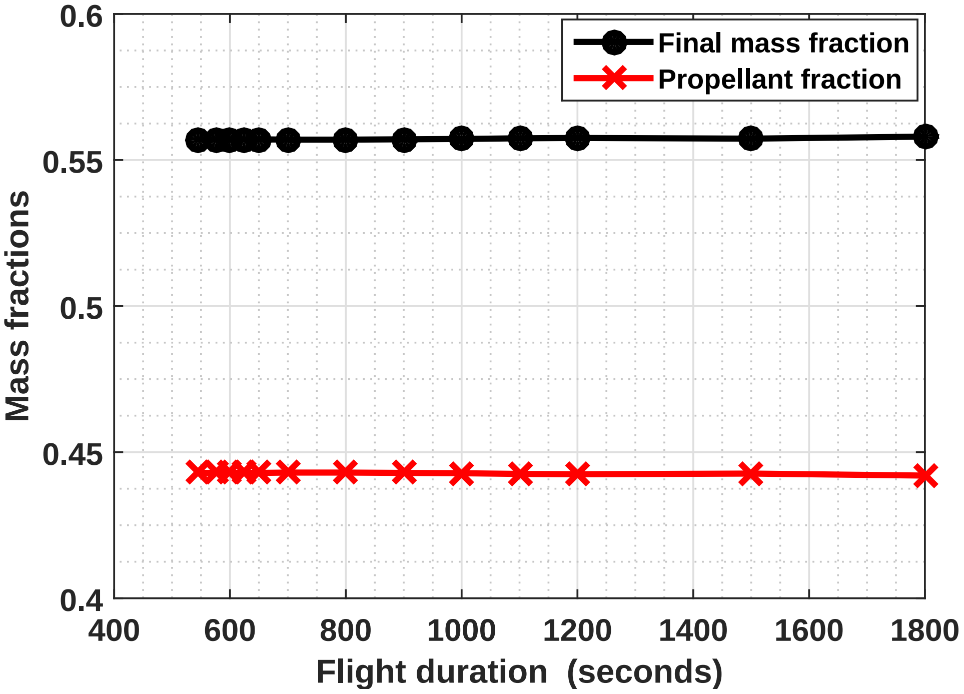

Fig. B.9 Influence of the flight duration on the fuel fraction and final delivered mass.

In figure B.9, it is seen that increasing flight duration causes a small drop in the fuel fraction with the final mass fraction delivered rising by a corresponding amount. This rise is only of the order of 0.8kg for over a 200% rise in propellant fraction. Flight durations less than the time optimal value are not feasible solutions. This implies that unlike in the case of interplanetary transfers, increasing flight duration for optimal propulsive landing does not lead to significant savings in propellant mass. The increase in flight duration is managed by the generation of coast phases by the optimal control formulation. These type of trajectories with higher flight duration can be useful if there are constraints on the communication requirements as well as on the navigation, guidance and control systems. The increased flight duration can serve to allow for corrections or system resets in case of emergencies.

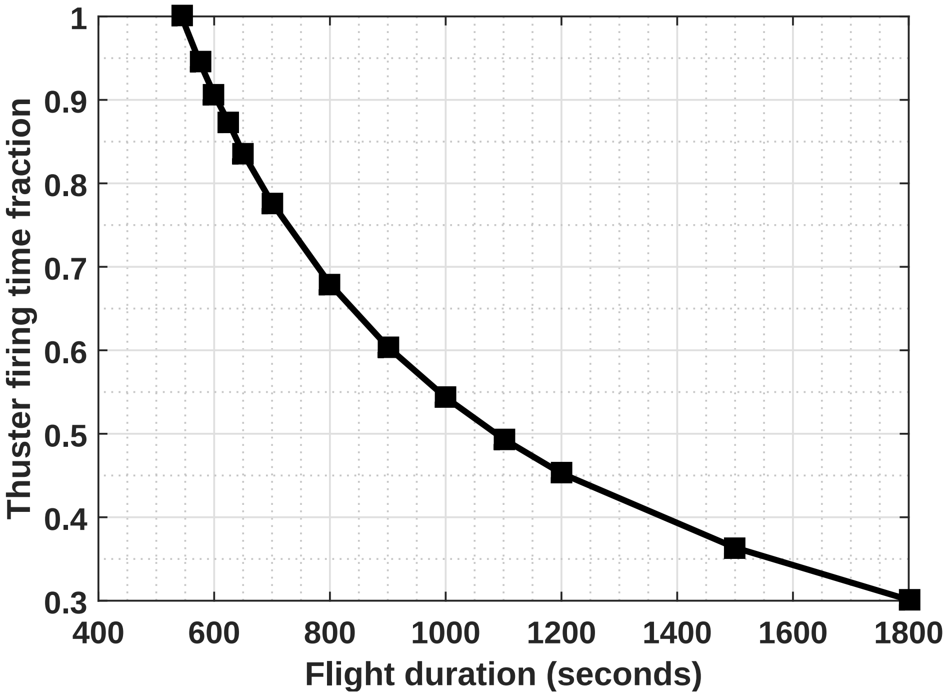

Fig. B.10 Fraction of time thruster is firing with varying flight duration.

Figure B.10 shows results for the fraction of time the thruster is firing versus the total flight duration. In the time optimal formulation, it is seen that the thruster is continuously firing throughout. For increased flight duration, the thruster firing time fraction rapidly drops due to the appearance of a coast phase in the control leading to a thrust-coast-thrust control structure. This fraction varies such that the total thruster firing time is nearly a constant as the propellant consumption varies only by about 0.21%.

B.3 Conclusions

DE has been successfully applied to solve the problem of optimal propulsive descent. The results for landing a probe on Callisto have been presented along with a parametric study on the influence of the initial acceleration levels. Differential evolution has been shown to work for time optimal propulsive descent trajectories for a wide range of inputs. It has been hypothesized that selecting the minimum acceleration level which prevents the trajectory from rising to a value higher than the initial level will lead to an appropriate compromise between thrust level required and fuel fraction needed to perform the landing. The validity of this can be either proved or disproved by conducting several more parametric studies on the influence of initial acceleration to the fuel fraction and altitude ratio. The author is of the opinion that the proposed design strategy is suitable for realistic optimal lunar lander trajectory design. Fuel optimal parametric results have been generated and it has been demonstrated that it is possible to have large increases in flight duration to satisfy other mission requirements without any compromise on the fuel fraction required.

Appendix C

Variable Thrust, Variable Specific Impulse Fuel Optimal Formulation

The specific impulse and acceleration vector components are taken to be the controls here. For a three dimensional transfer, this results in four control variables. The number of constraints on the feasible set of controls also increases as new constraints appear on the specific impulse. The constraints are as follows,

$$m\sqrt{a_x^2+a_y^2+a_z^2} \leq \frac{2P\eta}{g_0 I_{sp}} \tag{C.1}$$

$$m\sqrt{a_x^2+a_y^2+a_z^2} \geq 0 \tag{C.2}$$

$$I_{sp} \leq I_{sp_{max}} \tag{C.3}$$

$$I_{sp} \geq I_{sp_{min}} \tag{C.4}$$